Effects of Spin-Orbit Coupling on Quantum Transport

Jens Hjörleifur Bárðarson

Cover designed by Guneeta.

Effects of Spin-Orbit Coupling on Quantum Transport

PROEFSCHRIFT

ter verkrijging van de graad
van Doctor aan de Universiteit Leiden, op gezag van
de Rector Magnificus prof. mr. P.F. van der Heijden,
volgens besluit van het College voor Promoties
te verdedigen op woensdag 4 juni 2008
te klokke 15.00 uur

door

Jens Hjörleifur Bárðarson

geboren te Reykjavík in 1979

Promotiecommissie:

Promotor:	Prof. dr. C. W. J. Beenakker
Referent:	Prof. dr. ir. G. E. W. Bauer (Technische Universiteit Delft)
Overige leden:	Prof. dr. J. van den Brink
	Prof. dr. J. M. van Ruitenbeek
	Prof. dr. H. Schiessel
	Dr. J. Tworzydło (Universiteit van Warschau)
	Dr. ir. C. H. van der Wal (Rijksuniversiteit Groningen)

Casimir PhD Series, Delft-Leiden, 2008-01
ISBN: 978-90-8593-040-2

The research described in this thesis was supported by the European Community's Marie Curie Research Training Network under contract MRTN-CT-2003-504574, Fundamentals of Nanoelectronics for the first three years, and by the Leiden Institute of Physics for the fourth year.

Fyrir mömmu og pabba,
Guðmund, Kristjönu, Helga og Hlyn.
Takk fyrir allt.

Contents

1 Introduction **1**
- 1.1 Spin and Spin-Orbit Coupling . . . 3
  - 1.1.1 Spin and the Stern-Gerlach Experiment . . . 4
  - 1.1.2 Spin-Orbit Coupling from the Dirac Equation . . . 6
  - 1.1.3 Spin and Rotations . . . 8
  - 1.1.4 Spin-Orbit Coupling in Semiconductors . . . 13
- 1.2 Time Reversal and Kramers Degeneracy . . . 17
  - 1.2.1 Antiunitary Operators . . . 18
  - 1.2.2 Quaternions . . . 19
  - 1.2.3 Time Reversal . . . 21
  - 1.2.4 Consequences of Time Reversal for Hamiltonians . . . 24
  - 1.2.5 Consequences of Time Reversal for Scattering Matrices 26
- 1.3 Model Hamiltonians . . . 29
  - 1.3.1 The Rashba Hamiltonian . . . 30
  - 1.3.2 Graphene - the Single Valley Dirac Hamiltonian . . . 33
- 1.4 This Thesis . . . 34

2 Stroboscopic Model of Transport Through a Quantum Dot with Spin-Orbit Coupling **45**
- 2.1 Introduction . . . 45
- 2.2 Description of the Model . . . 46
  - 2.2.1 Closed System . . . 46
  - 2.2.2 Open System . . . 49
- 2.3 Relation to Random-Matrix Theory . . . 51
  - 2.3.1 $\beta = 1 \to 2$ Transition . . . 51
  - 2.3.2 $\beta = 1 \to 4$ Transition . . . 53
  - 2.3.3 $\beta = 4 \to 2$ Transition . . . 55
- 2.4 Numerical Results . . . 55

2.5 Conclusion 56

3 How Spin-Orbit Coupling can Cause Electronic Shot Noise 59
3.1 Introduction 59
3.2 The Effect of Spin-Orbit Coupling on the Ehrenfest Time . 60
3.3 Numerical Simulation in a Stadium Billiard 62
3.4 Conclusion 66

4 Degradation of Electron-Hole Entanglement by Spin-Orbit Coupling 67
4.1 Introduction 67
4.2 Calculation of the Electron-Hole State 69
4.2.1 Incoming and Outgoing States 69
4.2.2 Tunneling Regime 70
4.2.3 Spin State of the Electron-Hole Pair 71
4.3 Entanglement of the Electron-Hole Pair 72
4.3.1 Numerical Simulation 73
4.3.2 Isotropy Approximation 74
4.4 Conclusion 77
Appendix 4.A A Few Words on the Use of the Spin Kicked Rotator 78
Appendix 4.B Calculation of Spin Correlators 79

5 Mesoscopic Spin Hall Effect 83
5.1 Introduction 83
5.2 Scattering Approach 85
5.3 Random Matrix Theory 87
5.4 Numerical Simulation 89
5.5 Conclusion 90

6 One-Parameter Scaling at the Dirac Point in Graphene 91
6.1 Introduction 91
6.2 Transfer Matrix Approach 93
6.3 Numerical Results 96
6.4 Conclusion 99

References 101

Summary (in Dutch) 109

List of Publications 111

Curriculum Vitæ 113

Chapter 1

Introduction

In the center of Leiden there is a little park alongside a tranquil canal. On the other side of the canal, facing the park, is a magnificent old building that radiates history. The first hint towards its nature is the towering name *Kamerlingh Onnes* that marks the buildings front face[1]. This is, of course, the old physics building of the University of Leiden. Many great minds have graced this place with their presence and one of them, Paul Ehrenfest[2], has a particularly strong influence on this thesis. This influence, as we will discuss shortly, is both direct and indirect through three of his students: Hendrik Anthony Kramers, George Uhlenbeck, and Samuel Goudsmit (Fig. 1.1).

A few words about the contents of this thesis are, before revealing the connection to Ehrenfest, in order. The word *effects* in the title, hints at a certain diversity in the topics covered. In fact, in later chapters we will be concerned with a number of seemingly unrelated topics including quantum

[1]Heike Kamerlingh Onnes received the Nobel Prize in Physics in 1913 "for his investigations on the properties of matter at low temperatures which led, inter alia, to the production of liquid helium". He discovered superconductivity with his student Holst [1].

[2]It is fitting that it is Ehrenfest that takes the central stage in this story, for he was a genuine scientist. Einstein supposedly said that "he was not merely the best teacher in our profession whom I have ever known; he was also passionately preoccupied with the development and destiny of men, especially his students. To understand others, to gain their friendship and trust, to aid anyone embroiled in outer or inner struggles, to encourage youthful talent – all this was his real element, almost more than his immersion in scientific problems".

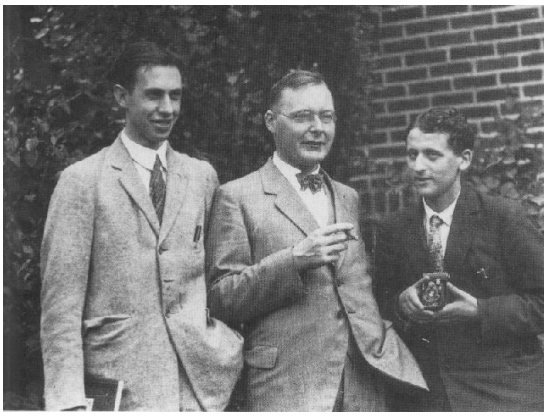

Figure 1.1. Left panel: The inventors of spin, George Uhlenbeck (left) and Samuel Goudsmit (right), with Hendrik Kramers who first noticed a twofold degeneracy in the solutions to the Schrödinger equation with spin: the Kramers degeneracy. All three were students of Paul Ehrenfest (right panel) in Leiden.

chaos, electronic shot noise, electron-hole entanglement, spin Hall effect, and (absence of) Anderson localization. While it certainly would be useful to have an extensive introduction to all these different topics there simply is not enough space to do them all justice (a brief introduction is given in Sec. 1.4). Instead, in this introduction, the focus is on what brings all these topics together in this thesis, namely *spin-orbit coupling*. In particular, we will concentrate on some fundamental aspects of quantum transport in the presence of spin-orbit coupling, the details of which are assumed known in the literature but are not always easily found in textbooks.

Before going into details, it is unavoidable in a thesis so involved with spin, to mention *spintronics*; if only as a means of motivation. Spintronics is a large field whose name indicates the wish to do electronics with spins. There are several technological reasons why one would want to do that, and initial successes are a testimony to their validity. Let us, however, not go down that road, but rather view the word spintronics as denoting the drive towards a fundamental understanding of quantum transport of spins. With this view it is difficult, for a physicist, not to get excited. The spin has from its discovery by Uhlenbeck and Goudsmit (under the guidance of

Ehrenfest[3]) tickled the imagination of physicists. Being purely quantum mechanical some of its properties are plain puzzling, but it is the simplicity of its description coupled with the richness of its physics that excites.

But let us not get too carried away, we were talking about spintronics. Initially, much of the interest was in systems that combined ferromagnets with metals or semiconductors. Later, interest grew in purely electronic systems, in which one talks to the spin degree of freedom through spin-orbit coupling. In this thesis we will be concerned with the latter type of systems.

To set the stage we will in this introduction start by giving a general introduction to spin and spin-orbit coupling in Sec. 1.1. Spin-orbit coupling conserves time reversal symmetry. The consequences of time reversal have thus to be taken into account. One particularly important consequence is a degeneracy named after the third of Ehrenfest students, the *Kramers degeneracy*. (We have now mentioned all the indirect influences of Ehrenfest, his direct influence will be encountered in chapter 3 on the effect of spin-orbit coupling on the Ehrenfest time[4].) In Sec. 1.2 we give a detailed account of time reversal symmetry and its consequences for the spectrum and symmetries of Hamiltonians and scattering matrices.

In Sec. 1.3 we solve two model Hamiltonians, the Rashba Hamiltonian and the single valley graphene Dirac Hamiltonian, whose solutions will be useful in later chapters. Finally, in Sec. 1.4 we give a brief introduction to each of the chapters of this thesis.

1.1 Spin and Spin-Orbit Coupling

It was after a detailed study of spectroscopic data that Uhlenbeck and Goudsmit came to suggest that the electron has spin, an intrinsic angular

[3]Ehrenfest's contribution, allowing his students to go ahead with a wild idea with the words "you are both young enough to be able to afford a stupidity", was crucial. About the same time, Ralph Kronig had similar ideas, but the response of his supervisor, Wolfgang Pauli, "it is indeed very clever but of course has nothing to do with reality", was in stark contrast to Ehrenfest's.

[4]Strictly speaking, the Ehrenfest time does not come directly from Ehrenfest himself. The Ehrenfest time τ_E is the time it takes a wavepacket to spread to a size on the order of the system size. For times smaller then τ_E the center of the wavepacket and its group velocity satisfy Ehrenfest's theorem, thus the name.

momentum that gives arise to a magnetic moment. Most physicists first acquaintance with spin, however, is through a recount of the Stern-Gerlach experiment [2]. Building on this familiarity, we will begin our discussion by using a combination of the results of the experiment and classical arguments to deduce the presence of the spin and a coupling of this spin to the orbital motion. The same results are then obtained more rigorously from the nonrelativistic limit of the Dirac equation. In turn, this leads us to an analysis of the rotation properties of spin and the accompanying Berry phase. We demonstrate the importance of this phase by considering its role in weak (anti) localization. To complete this section, we sketch how the spin-orbit coupling in semiconductors gives rise to the familiar Rashba and Dresselhaus terms.

1.1.1 Spin and the Stern-Gerlach Experiment

With their experiment, Stern and Gerlach, established the following empirical fact: The electron has an intrinsic magnetic moment $\boldsymbol{\mu}_s$ which takes on quantized values $\pm\mu_B$ along any axis ($\mu_B = e\hbar/2mc$ is the Bohr magneton). This suggests the introduction of a quantum number $\sigma = \pm$ such that the wavefunction of the electron can be represented by a two component spinor

$$\psi(\boldsymbol{r}) = \begin{pmatrix} \psi_+(\boldsymbol{r}) \\ \psi_-(\boldsymbol{r}) \end{pmatrix}. \tag{1.1}$$

Quite often the state of the electron factorizes, i.e. it can be written as a direct product $|\psi\rangle \otimes |\chi\rangle$ where $|\chi\rangle$ is a state vector (two component spinor) in the two dimensional Hilbert space of the spin. Any operator in this two dimensional space (i.e. any 2×2 matrix[5]) can be written as a linear combination of the 2×2 unit matrix $\mathbb{1}$ and the *Pauli matrices*

$$\sigma_1 = \begin{pmatrix} 0 & 1 \\ 1 & 0 \end{pmatrix}, \quad \sigma_2 = \begin{pmatrix} 0 & -i \\ i & 0 \end{pmatrix}, \quad \sigma_3 = \begin{pmatrix} 1 & 0 \\ 0 & -1 \end{pmatrix}. \tag{1.2}$$

In particular, any vector operator is necessarily proportional to $\boldsymbol{\sigma} = (\sigma_1, \sigma_2, \sigma_3)$.

What are the consequences of this empirical fact? Suppose our electron

[5] See also the section 1.2.2 on quaternions.

is moving with velocity $\boldsymbol{v}$ in an electric field $-e\boldsymbol{E} = -\boldsymbol{\nabla}V$. Classically the magnetic moment does not couple to the electric field. However, taking into account relativistic effects, the electron sees in its rest frame a magnetic field, which to order $(v/c)^2$ (with c the speed of light) is given by $\boldsymbol{B} = -\boldsymbol{v} \times \boldsymbol{E}/c$ [3]. The interaction of the magnetic moment $\boldsymbol{\mu}_s$ with this magnetic field leads to a potential energy term

$$V_{\mu_s} = -\boldsymbol{\mu}_s \cdot \boldsymbol{B} = \boldsymbol{\mu}_s \cdot \frac{\boldsymbol{v}}{c} \times \boldsymbol{E} = \frac{1}{ec}\boldsymbol{\mu}_s \cdot \boldsymbol{v} \times \boldsymbol{\nabla}V. \tag{1.3}$$

In an atom, the potential giving rise to the electric field is central $V = V(r)$ and

$$V_{\mu_s} = \frac{1}{ecr}\frac{dV}{dr}\boldsymbol{\mu}_s \cdot \boldsymbol{v} \times \boldsymbol{r} = -\frac{1}{emcr}\boldsymbol{\mu}_s \cdot \boldsymbol{L}, \tag{1.4}$$

with $\boldsymbol{L} = \boldsymbol{r} \times \boldsymbol{p}$ the orbital angular momentum and m the electron mass. Including this term in the quantum description, the conservation of angular momentum seems to be broken (since the components of $\boldsymbol{L}$ do not commute). To rescue the conservation of angular momentum, the electron needs to have an intrinsic angular momentum $\boldsymbol{S}$. In analogy with orbital moments, we expect the magnetic moment $\boldsymbol{\mu}_s$ to be proportional to the angular momentum

$$\boldsymbol{\mu}_s = -\frac{g_s \mu_B}{\hbar}\boldsymbol{S}. \tag{1.5}$$

Since $\boldsymbol{S}$ is a vector operator in spin space it is necessarily a multiple of $\boldsymbol{\sigma}$. The interaction term V_{μ_s} is thus proportional to $\boldsymbol{\sigma} \cdot \boldsymbol{L}$. The only possible choice for $\boldsymbol{S}$ such that the full angular momentum $\boldsymbol{J} = \boldsymbol{L} + \boldsymbol{S}$ is conserved turns out to be [2]

$$\boldsymbol{S} = \frac{\hbar}{2}\boldsymbol{\sigma}. \tag{1.6}$$

The magnetic moment becomes $\boldsymbol{\mu}_s = -(g_s/2)\mu_B\boldsymbol{\sigma}$ and since the eigenvalues of the Pauli matrices are ± 1 we need to take the g factor $g_s = 2$ to explain the observed quantization of $\boldsymbol{\mu}$.

With a careful consideration of their experiment we have learned a lot from Stern and Gerlach. We have been able to deduce the existence of the spin and we have seen how the interaction of the magnetic moment with

the electric field can alternatively be seen as a spin-orbit coupling

$$V_{\mu_s} = \frac{\hbar}{2m^2c^2}\frac{1}{r}\frac{dV}{dr}\boldsymbol{\sigma}\cdot\boldsymbol{L}, \tag{1.7}$$

In a noncentral potential this spin-orbit coupling is

$$V_{\mu_s} = -\frac{\hbar}{2m^2c^2}\boldsymbol{\sigma}\cdot\boldsymbol{p}\times\nabla V. \tag{1.8}$$

This is still not the full story. In addition to the effect just described we need to take into account a term that has a purely kinematic origin. To be able to use the above results we need to be in the rest frame of the electron. Since the electron is accelerating the reference frame is constantly changing. This amounts to successive Lorentz boosts. However since Lorentz boosts do not form a subgroup in the group of Lorentz transformations (which includes boosts and rotations) two successive boosts are in general not equivalent to another boost but rather to a boost followed by a rotation. There is thus an additional precession, *Thomas precession*, that needs to be taken into account. This turns out to give a contribution of the same form as (1.8) but with opposite sign and half the amplitude [3]. The full spin-orbit coupling term is thus

$$V_{\text{so}} = -\frac{\hbar}{4m^2c^2}\boldsymbol{\sigma}\cdot\boldsymbol{p}\times\nabla V. \tag{1.9}$$

1.1.2 Spin-Orbit Coupling from the Dirac Equation

Last section painted a nice physical picture of the origin of spin-orbit coupling. The arguments, however, are a bit handwavy and alternate between being classical, quantum and relativistic. A more satisfactory, albeit less physically transparent, derivation can be obtained by taking the nonrelativistic limit of the Dirac equation. This procedure leads to the Pauli equation. In this section we sketch the derivation following the more general derivation given by Sakurai [4].

In the standard representation, and in Hamiltonian form, the Dirac

equation is $H|\psi\rangle = E|\psi\rangle$ with [4]

$$H = \begin{pmatrix} 0 & c\,\boldsymbol{p}\cdot\boldsymbol{\sigma} \\ c\,\boldsymbol{p}\cdot\boldsymbol{\sigma} & 0 \end{pmatrix} + \begin{pmatrix} mc^2 & 0 \\ 0 & -mc^2 \end{pmatrix}. \tag{1.10}$$

Writing $|\psi\rangle = (\psi_A, \psi_B)^T$ we have two coupled equations for ψ_A and ψ_B. Using the second equation to eliminated ψ_B we obtain

$$\boldsymbol{p}\cdot\boldsymbol{\sigma}\frac{c^2}{E+mc^2}\boldsymbol{p}\cdot\boldsymbol{\sigma}\psi_A = (E-mc^2)\psi_A. \tag{1.11}$$

In the presence of a potential V, we make the substitution $E \to E - V$. We are interested in the nonrelativistic limit, so we write $E = mc^2 + \epsilon$ with $\epsilon \ll mc^2$. Further assuming that $|V| \ll mc^2$ we can expand

$$\frac{c^2}{E - V + mc^2} = \frac{1}{2m}\left(1 - \frac{\epsilon - V}{2mc^2} + \cdots\right). \tag{1.12}$$

Since $mv^2/2 + V \sim \epsilon$, the second term is seen to be of order $(v/c)^2$. To zeroth order, using[6] $(\boldsymbol{p}\cdot\boldsymbol{\sigma})(\boldsymbol{p}\cdot\boldsymbol{\sigma}) = p^2$, we simply obtain the Schrödinger equation

$$\left(\frac{p^2}{2m} + V\right)\psi = \epsilon\psi. \tag{1.13}$$

The reason this derivation works is that to zeroth order in (v/c), $\psi_B = 0$. In fact, from (1.10) we have to first order in $(v/c)^2$

$$\psi_B = \frac{\boldsymbol{p}\cdot\boldsymbol{\sigma}}{2mc}\psi_A. \tag{1.14}$$

In other words, in this limit ψ_A is equivalent to the Schrödinger wavefunction ψ. When going to next order, more care must be taken. The probabilistic interpretation of Dirac theory requires the normalization

$$\int(\psi_A^\dagger\psi_A + \psi_B^\dagger\psi_B) = 1. \tag{1.15}$$

[6] As a special case of the more general formula $(\boldsymbol{\sigma}\cdot\boldsymbol{A})(\boldsymbol{\sigma}\cdot\boldsymbol{B}) = \boldsymbol{A}\cdot\boldsymbol{B} + i\boldsymbol{\sigma}\cdot(\boldsymbol{A}\times\boldsymbol{B})$.

To first order, using (1.14), this gives

$$\int \psi_A^\dagger \left(1 + \frac{p^2}{4m^2c^2}\right) \psi_A = 1. \tag{1.16}$$

Apparently, to have a normalized wave function, we should use $\psi = [1 + p^2/(8m^2c^2)]\psi_A$. Substituting this into the Dirac equation, and using the expansion (1.12), we obtain after some rearrangement [4] the Pauli equation

$$\left(\frac{p^2}{2m} + V - \frac{p^4}{8m^3c^2} - \frac{\hbar}{4m^2c^2}\boldsymbol{\sigma}\cdot\boldsymbol{p}\times\boldsymbol{\nabla}V + \frac{\hbar^2}{8m^2c^2}\boldsymbol{\nabla}^2V\right)\psi = \epsilon\psi. \tag{1.17}$$

All the terms in this equation have a ready made interpretation. The third term is simply a relativistic correction to the kinetic energy, and the last term gives a shift in energy. The fourth term is the spin-orbit coupling term (1.9) we derived heuristically in the last section. It is gratifying to obtain the same result from the Dirac equation.

1.1.3 Spin and Rotations

Not only does the spin-orbit coupling emerge naturally from the Dirac equation, the spin itself is buried within the equation. Recall that the Dirac equation can be obtained with little more then Lorentz invariance. To discuss how spin arises in the Dirac equation we need to briefly discuss the theory of rotations. Since we will learn important facts about the rotations of spins at the same time, it is a worthwhile endeavor.

Infinitesimal rotations in a three dimensional space, of an angle $\delta\varphi$ about an axis $\hat{\boldsymbol{n}}$, are given by

$$U_R = \mathbb{1} - \frac{i}{\hbar}\delta\varphi\,\hat{\boldsymbol{n}}\cdot\boldsymbol{J}, \tag{1.18}$$

with $\boldsymbol{J} = (J_x, J_y, J_z)$ three operators which are called the *generators of infinitesimal rotations*. From the properties of rotations one deduces that the components of $\boldsymbol{J}$ satisfy the commutation relations [2]

$$[J_i, J_j] = i\hbar\varepsilon_{ijk}J_k, \tag{1.19}$$

with ε_{ijk} the fully antisymmetric tensor, or Levi-Civita symbol[7]. These are just the commutation relations of an angular momentum. In particular, rotations of a spin half particles are given by (1.18) with $\boldsymbol{J} = \boldsymbol{S}$. Integrating (1.18) and using the relation (1.6) of $\boldsymbol{S}$ to $\boldsymbol{\sigma}$, finite rotations of spin are given by

$$U_s = \exp\left(-i\frac{\varphi}{2}\hat{\boldsymbol{n}}\cdot\boldsymbol{\sigma}\right) = \cos\frac{\varphi}{2} - i\hat{\boldsymbol{n}}\cdot\boldsymbol{\sigma}\sin\frac{\varphi}{2}. \tag{1.20}$$

To obtain the second equality, we used that[8] $(\hat{\boldsymbol{n}}\cdot\boldsymbol{\sigma})^2 = 1$. As a consequence, we notice that a rotation of 2π does not bring you back to the same state, but rather minus the state, i.e. $U_s(2\pi) = -1$.

On first acquaintance this minus sign is odd. The mathematical explanation, that SU(2) is a twofold covering of SO(3), is only illuminating once you know what it means. Physicists like to picture the spin as living on the Bloch sphere. This description, however, does not contain the Berry's phase since a rotation of 2π brings you back to the same point on the Bloch sphere. The reason, of course, is that in constructing the Bloch sphere, a global phase factor of a general spin state was ignored. For an isolated spin this global phase factor does not lead to any observable effect, but there are cases when it is important (see below).

One way to picture what is going on, is to introduce a "Möbius-Bloch sphere"[9]. To explain what that means, start by picturing the normal Möbius strip, embedded in three dimensional space. Imagine walking along the strip with a cap on your head carrying an arrow that points upwards. Now you walk along the strip and after walking half of the strip, you are back at the same point in the three dimensional embedding space. In this space, however, you are on the "other side" of the strip, your arrow pointing in the opposite direction[10] (minus sign). If you were to identify the point you are on now, with the point that you started from, you would have a circle and you find you have gone around the full circle. But if you do not identify the point you find that you need to walk another full circle

[7] $\varepsilon_{ijk} = 1(-1)$ for an (odd) even permutation of (123) and zero otherwise.

[8] A consequence of the relation in footnote 6 and $|\hat{\boldsymbol{n}}|^2 = 1$.

[9] We are not aware of a strict mathematical equivalence between SU(2) and a "Möbius-Bloch sphere". It is introduced here for ease of visualization.

[10] Other side within quotations marks, since the Möbius strip has only one side.

to come back to your original point of departure. Generalizing this to the sphere, you imagine any great circle on the sphere to be a Möbius strip, and the fact that rotation about 2π gives a minus sign can be visualized[11].

How does spin come about in the Dirac equation? As already mentioned the Dirac equation is constructed to be Lorentz invariant. In demanding this invariance, in particular one can consider infinitesimal rotations. One finds that for the Dirac equation to be invariant the Dirac spinors need to transform in a certain way. Equating this transformation with general statement (1.18) about angular momentum as generators of rotation, one can simply read of the angular momentum of the electron. In addition to the orbital angular momentum $\boldsymbol{L}$ one indeed finds an intrinsic angular momentum[12] given by $\boldsymbol{S} = \hbar/2\boldsymbol{\sigma}$ as we had concluded earlier from the Stern-Gerlach experiment.

We conclude this section with an example of the effect of the (Berry's) phase obtained from a rotation of the spin. The effect we consider is the weak (anti)localization [5], which is a quantum correction to the classical conductance of a system arising from quantum interference. To understand the effect, imagine injecting a particle into a scattering region and ask about the probability for it to return. Let us start with the spinless case. The probability amplitude of reflection back in the same mode can be written as a sum over classical paths γ starting and ending at the same point [6]

$$r = \sum_{\gamma} \mathcal{A}_{\gamma} \exp\left(\frac{i}{\hbar}\mathcal{S}_{\gamma}\right). \tag{1.21}$$

$\mathcal{S}_{\gamma}$ is the action along γ and $\mathcal{A}_{\gamma}$ is a classical weight. The reflection probability is

$$R = rr^{\dagger} = \sum_{\gamma,\gamma'} \mathcal{A}_{\gamma}\mathcal{A}^{*}_{\gamma'} e^{i/\hbar(\mathcal{S}_{\gamma}-\mathcal{S}_{\gamma'})}. \tag{1.22}$$

In the classical limit, $\hbar \to 0$, the exponential is quickly oscillating, and

[11] Incidentally, your shoulder has the same property. Imagine holding a cup filled with coffee in one hand. Now rotate it by an angle 2π without spilling it. You find that to obtain that goal you needed to twist your arm which is now inverted (it acquired a "minus sign"). With some skill you can rotate the cup another 2π in the same direction, to find yourself in your initial configuration.

[12] Or more exactly, an angular momentum that in the nonrelativistic limit reduces to the Pauli equation spin [4].

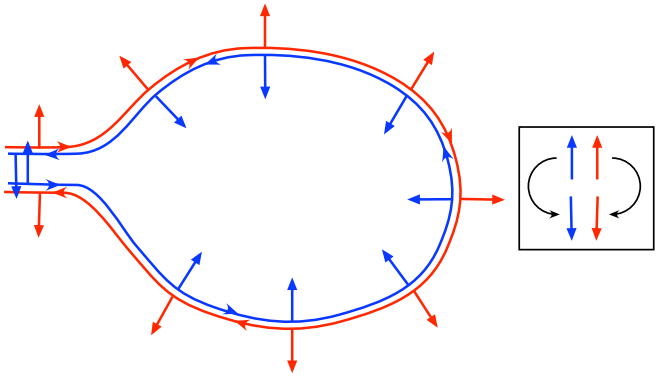

Figure 1.2. A schematic representation of a trajectory (red) and it time reverse (blue). The spin dynamics are assumed adiabatic such that the spin just adjusts itself to be always in an eigenstate. As the (time reversed) trajectory is followed the spin is seen to rotate about an angle of π $(-\pi)$. This rotation of the spin leads to an extra phase causing a destructive interference between the two paths.

only the paths with $S_\gamma = S_{\gamma'}$ contribute to the sum. In particular, the classical reflection probability is obtained by including only the terms with $\gamma' = \gamma$,

$$R_{\rm cl} = \sum_\gamma |\mathcal{A}_\gamma|^2. \tag{1.23}$$

In the presence of time reversal symmetry, the time reversed path $\tilde{\gamma}$ has the same action and weight factor as γ. Thus, in addition to the classical contribution, we have the extra term

$$R_{\rm wl} = \sum_{\gamma=\tilde{\gamma}} |\mathcal{A}_\gamma|^2 = R_{\rm cl}. \tag{1.24}$$

We thus see that the total reflection probability $R = R_{\rm cl} + R_{\rm wl} = 2R_{\rm cl}$ is enhanced compared to the classical reflection probability. This leads to a smaller conductance, and the correction term is referred to as *weak localization*. Essentially the path γ and its time reverse $\tilde{\gamma}$ interfere constructively to enhance the reflection probability.

When we have spin-orbit coupling there is more to the story. Most of the time the spin-orbit coupling is weak, so we can ignore the effect it has

on trajectories. The spin-orbit coupling does however rotate the spin of the electron as it moves around the classical path. One then finds that the only modification to the reflection amplitude r, is an introduction of a spin phase factor [7, 8] K_γ

$$r = \sum_\gamma K_\gamma \mathcal{A}_\gamma \exp\left(\frac{i}{\hbar}\mathcal{S}_\gamma\right). \tag{1.25}$$

The reflection probability becomes

$$R = rr^\dagger = \sum_{\gamma,\gamma'} \mathcal{M}_{\gamma,\gamma'} \mathcal{A}_\gamma \mathcal{A}^*_{\gamma'} e^{i/\hbar(\mathcal{S}_\gamma - \mathcal{S}_{\gamma'})}. \tag{1.26}$$

with $M_{\gamma,\gamma'} = K_\gamma K^*_{\gamma'}$ a *spin modulation factor*. K_γ is essentially[13] just $e^{i\alpha_\gamma}$ with α_γ the phase picked up by rotating the spin as we go along the path γ. Therefore, $\mathcal{M}_{\gamma,\gamma} = 1$ and the classical contribution to the reflection amplitude $R_{\rm cl}$ is the same as in the spinless case. If the spin-orbit coupling is strong enough the spin will simply adiabatically follow the path. The contribution of the time reversed pair of paths gets an extra minus sign $M_{\gamma,\tilde{\gamma}} = -1$. The reason is that following the path γ the spin is rotated by π, while for the path $\tilde{\gamma}$ it is rotated by $-\pi$ (see Fig. 1.2). Because of the complex conjugation in $M_{\gamma,\tilde{\gamma}} = K_\gamma K^*_{\tilde{\gamma}}$ these two phases add up to give a total rotation of 2π, leading to a Berry's phase of -1. The quantum correction

$$R_{\rm wal} = \sum_{\gamma=\tilde{\gamma}} \mathcal{M}_{\gamma,\tilde{\gamma}} |\mathcal{A}_\gamma|^2 = -R_{\rm cl}, \tag{1.27}$$

is referred to as *weak antilocalization*. The total reflection amplitude $R = R_{\rm cl} + R_{\rm wal} = 0$ vanishes, leading to a larger conductance.

Note that there is of course some reflection. What we considered here was only a part of the full scattering problem, namely we only looked at reflection back into the same mode.[14] This is why in the full problem (when

[13] We are simplifying things a bit here, K_γ is really matrix elements of a propagator of spin dynamics, and $\mathcal{M}$ is the trace over a product of propagators [7, 8]. The essential physics is still contained in our presentation.

[14] Actually, if the incident mode was $|n\rangle$ we looked at reflection into its time reverse

taking into account all modes), the classical contribution is proportional to the number of modes N, while the weak (anti)localization correction is of order one.

1.1.4 Spin-Orbit Coupling in Semiconductors

The Pauli equation (1.17) describes an electron moving in vacuum in the presence of a potential V. In a single particle picture of a solid, essentially the same equation can be used to obtain effective Hamiltonians describing the movement of electrons. Usually, we neglect the third and fifth term and write

$$\left(\frac{p^2}{2m} + V_0(\boldsymbol{r}) - \frac{\hbar}{4m^2c^2}\boldsymbol{\sigma}\cdot\boldsymbol{p}\times\boldsymbol{\nabla}V_0 + V(\boldsymbol{r})\right)\psi = E\psi. \tag{1.28}$$

Here V_0 is the periodic crystal potential, and V is an external applied potential (e.g. gate voltage). The main contribution to the spin-orbit coupling comes from the crystal potential, so we have neglected V in the third term.

We are interested in obtaining an effective Hamiltonian describing the motion of electrons in our semiconductor. There are essentially two approaches. One is the theory of invariants which is a purely group theoretical approach. The second, the Kane model, tries to obtain a solution with reasonable approximation to Eq. (1.28). It is the second approach we want to discuss here. A detailed account has been given of the method and the calculations in Refs. 9 and 10, to which we refer for details. Fortunately, we only need to introduce a few energy scales to get a flavor of the derivation and the meaning of its results.

In the absence of the spin-orbit term and external potentials a solution of Eq. (1.28) gives us the first approximation to the bandstructure of the solid. In the semiconductors we have in mind, the part of the bandstructure we are interested in will consist of a conduction band and a valence band separated by a band gap E_0 at a certain k value. Often (e.g. in GaAs) this is the Γ point $k = 0$. One can understand these bands as emerging from

$T|n\rangle$. In the spinless case, this is simply reversal of momentum, in the spin case the direction of the spin is also inverted (cf. Sec. 1.2.5).

the atomic levels of the constituent atoms of the solid. The conduction band is derived from s orbitals of the atom (basis states $|S\rangle$) and the valence band from p orbitals (basis states $|X\rangle, |Y\rangle, |Z\rangle$). The conduction band is therefore twofold (because of spin) and the valence band sixfold degenerate at the band edge (Γ point).

When we take into account the spin-orbit coupling, the bands become mixed and are now characterized by their total angular momentum quantum numbers (j and m_j) plus the orbital momentum index $l = 0$ ($l = 1$) characterizing the conduction (valence) bands. The conduction band now has $j = 1/2$ and $m_j = \pm 1/2$ while two of the valence bands ($j = 1/2, m_j = \pm 1/2$) split off from the other four ($j = 3/2, m_j = \pm 1/2, \pm 3/2$). In addition the $j = 3/2$ bands, while degenerate at the band edge, have a different curvature (i.e. effective mass) and are referred to as heavy hole (hh) and light hole (lh) band (cf. Fig. 1.3). The split off energy Δ_0 is simply given by an energy scale obtained from the spin-orbit coupling term

$$\Delta_0 = -\frac{3i\hbar}{4m^2c^2}\langle X|(\boldsymbol{\nabla} V_0 \times \boldsymbol{p}) \cdot \hat{\boldsymbol{y}}|Z\rangle. \tag{1.29}$$

The basic idea of the Kane model is that the band edge eigenstates (eigenstates with a fixed k) constitute a complete basis. To obtain the eigenstates away from the band edge we simply expand the wavefunction (in an envelope function approximation) in the band edge states. Bands that are far away in energy can be neglected. In the original Kane model, only the bands in Fig. 1.3 where taken into account, leading to an 8×8 band Hamiltonian

$$H = \begin{pmatrix} H_{cc} & H_{cv} \\ H_{vc} & H_{vv} \end{pmatrix}. \tag{1.30}$$

Here H_{cc} (H_{vv}) is the block of the conduction (valence) band eigenstates. The coupling H_{cv} between the conduction and valence band depends on the momentum operator matrix element

$$P_0 = \frac{\hbar}{m}\langle S|p_x|X\rangle. \tag{1.31}$$

Once one has the Hamiltonian (1.30), the final step is to find a unitary

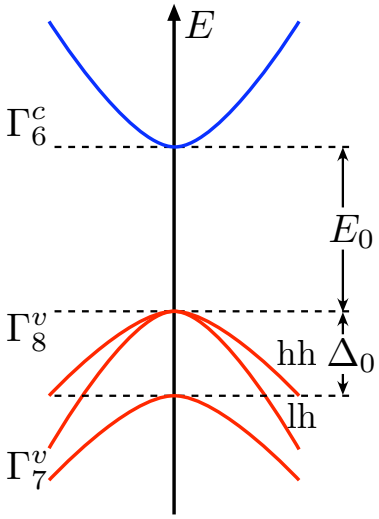

Figure 1.3. A schematic of the band structure of a zinc-blend structure, showing the twofold conduction band (Γ_6^c) and the six spin-orbit split valence bands (Γ_7^v and Γ_8^v). The conduction band and the topmost valence bands (heavy hole (hh) and light hole (lh)) are separated by the energy gap E_0. The spin-orbit split off valence band (Γ_7^v) is separated from the other valence bands by the energy Δ_0.

transformation U such that

$$UHU^\dagger = \begin{pmatrix} \tilde{H}_{cc} & 0 \\ 0 & \tilde{H}_{vv} \end{pmatrix}, \tag{1.32}$$

where $\tilde{H}_{cc}$ is now our effective Hamiltonian describing electrons in the conduction band.

Instead of going through the details, let us simply discuss the results of such a procedure, focusing on the spin-orbit coupling terms (the leading order terms will simply be the usual kinetic energy term with an effective mass). In a perturbation theory around $\boldsymbol{k} = 0$ we expect the lowest order terms that couple to the spin to be linear in $\boldsymbol{k}$. We can write

$$H_{\text{so}} = -\boldsymbol{B}(\boldsymbol{k}) \cdot \boldsymbol{\sigma}. \tag{1.33}$$

Time reversal symmetry requires $\boldsymbol{B}(-\boldsymbol{k}) = -\boldsymbol{B}(\boldsymbol{k})$. If in addition the

system has an inversion symmetry $\boldsymbol{B}(-\boldsymbol{k}) = \boldsymbol{B}(\boldsymbol{k})$ and the only possible solution is $\boldsymbol{B}(\boldsymbol{k}) = 0$. Thus for the term (1.33) to be nonzero the inversion symmetry needs to be broken[15].

In heterostructures the confinement potential and the band edge variations (different materials have different band gaps etc.) break the inversion symmetry. Taking this into account the procedure described above leads to the Rashba term

$$H_R = \alpha(k_x\sigma_y - k_y\sigma_x) \tag{1.34}$$

where

$$\alpha = \langle\alpha(z)\rangle, \tag{1.35a}$$

$$\alpha(z) = \frac{P_0^2}{3}\left[\frac{1}{(E_0+\Delta_0)^2} - \frac{1}{E_0^2}\right]\frac{dV}{dz}, \tag{1.35b}$$

with $\langle\ \rangle$ denoting an average over the z subband eigenstate that confines the electron to form a two dimensional electron gas.

A couple of important features of the Rashba spin-orbit coupling can be seen from the expression (1.35) for α. First is that it depends on the external (gate) potential V. We thus see that the size of α can be tuned by playing with the gate voltages. Second, we observe that the presence of Rashba spin-orbit coupling relies crucially on the size of the spin-orbit coupling in the semiconductor (as measured by Δ_0). If $\Delta_0 = 0$, $\alpha = 0$ regardless of the strength of the external potential. It is really by traveling near the nuclei that the electron picks up most of the spin-orbit coupling.

In zinc blend structure, such as GaAs, the inversion symmetry is also broken in the bulk leading to the Dresselhaus term

$$H_D = \beta(k_x\sigma_x - k_y\sigma_y). \tag{1.36}$$

To obtain this term one needs to take into account higher conduction bands so the expression for β is more complicated and contains additional parameters we have not defined, so we skip writing it down. In addition to

[15] Or time reversal symmetry which is trivially done by applying a magnetic field. We are interested in the all electronic setups (no magnetic fields) so we do not consider this possibility.

the linear Dresselhaus term (1.36) there is also a cubic (in k) Dresselhaus term which can be of importance [9].

1.2 Time Reversal and Kramers Degeneracy

In 1930 H. A. Kramers in his study of the Schrödinger equation of an electron with spin in the absence of a magnetic field, found a mapping T that given a solution $|\psi\rangle$ with energy E gives another solution $T|\psi\rangle$ with the same energy [11]. For systems with odd number of spin half electrons these solutions are orthogonal and therefore lead to a degeneracy in the spectrum, the *Kramers degeneracy*. A couple of years later Wigner pointed out that the mapping Kramers found is simply time reversal and that the degeneracy is a manifestation of the presence of time reversal symmetry [12].

Symmetries in quantum mechanics can be represented either by unitary and linear operators or antiunitary and antilinear operators, according to a theorem also due to Wigner [13]. We will see that time reversal is necessarily in the latter, somewhat less familiar category. There is a crucial difference between the two groups in the fact that while unitary symmetries lead to a conserved quantity (e.g. translation symmetry to conservation of momentum and rotation symmetry to conservation of angular momentum) antiunitary symmetries in general do not. The effect of antiunitary symmetries (time reversal) is thus more subtle, as reflected in the Kramers degeneracy, but just as important.

In addition to the Kramers degeneracy of energy eigenvalues, the presence of time reversal imposes a symmetry on Hamiltonians and scattering matrices. Furthermore, in scattering, transmission eigenvalues are twofold degenerate. The exact symmetries of the Hamiltonian are usually given in terms of quaternions (or Pauli sigma matrices) in which they take a simple form.

All the above mentioned properties are of importance in any quantum theory of transport. In the literature, these have become a common knowledge and are used as such. For a newcomer, it can take some time to dig up definitions and proofs of these important properties, in particular since topics such as antiunitary operators and quaternions are often not

included in textbooks. In the case of the Kramers degeneracy of transmission eigenvalues, the proofs that exist in the literature are somewhat convoluted and not given directly in terms of the scattering matrix. In this section we therefore represent definitions and proofs in a unified manner, and an alternative proof of the Kramers degeneracy of transmission eigenvalues.

We start by a review of the mathematical concepts of antiunitary operators and quaternions. Time reversal is then explained and its consequences for Hamiltonians and scattering matrices explored.

1.2.1 Antiunitary Operators

An operator T is said to be *antilinear*, if for any state vectors $|\varphi\rangle$, $|\psi\rangle$ and complex numbers α, β, it satisfies

$$T(\alpha\,|\varphi\rangle + \beta\,|\psi\rangle) = \alpha^* T\,|\varphi\rangle + \beta^* T\,|\psi\rangle\,. \tag{1.37}$$

The asterisk denotes complex conjugation. If in addition T has the property

$$|\langle\psi|\varphi\rangle| = |\langle T\psi|T\varphi\rangle|, \tag{1.38}$$

it is called *antiunitary* [13]. The relations (1.37) and (1.38) lead to the equality[16]

$$\langle T\psi|\,T\varphi\rangle = \langle\psi|\,\varphi\rangle^*, \tag{1.39}$$

which can equivalently be taken as the definition of antiunitarity [15].

The operator $\mathcal{C}$ of complex conjugation (with respect to the (orthogonal) basis $\{|n\rangle\}$) is an antiunitary operator that satisfies

$$\mathcal{C}\,|n\rangle = |n\rangle \quad \forall n, \quad \text{and} \quad \mathcal{C}^2 = 1. \tag{1.40}$$

[16] Note that the use of Dirac bra-ket notation, developed for *linear* vector spaces, is a risky business when dealing with antilinear operators. The safest approach is to let T first act on a ket, and only then use the dual correspondence to find the corresponding bra [14].

The action of $\mathcal{C}$ on a general state vector

$$|\psi\rangle = \sum_n c_n |n\rangle \tag{1.41}$$

is completely determined by these properties

$$\mathcal{C}|\psi\rangle = \sum_n c_n^* |n\rangle . \tag{1.42}$$

In particular, if

$$|\varphi\rangle = \sum_n d_n |n\rangle \tag{1.43}$$

we can confirm the antiunitary property (1.39)

$$\langle \mathcal{C}\psi|\mathcal{C}\varphi\rangle = \sum_n c_n d_n^* = \langle\psi|\varphi\rangle^*. \tag{1.44}$$

A product of an antiunitary and a unitary operator is again antiunitary, while the product of two antiunitary operators is unitary. Every antiunitary operator T can therefore be written as a product of a unitary operator U and the complex conjugation operator $\mathcal{C}$ (the form of U will depend on the basis with respect to which $\mathcal{C}$ is defined)

$$T = U\mathcal{C}. \tag{1.45}$$

In particular, the time reversal operator, our prime example of an antiunitary symmetry (and the reason for using here the symbol T to represent an antiunitary operator), will always be written in this form.

1.2.2 Quaternions

Sir W. R. Hamilton introduced quaternions as a generalization of complex numbers. Walking with his wife along the Royal Canal in Dublin, the defining equations of quaternions

$$\boldsymbol{i}^2 = \boldsymbol{j}^2 = \boldsymbol{k}^2 = \boldsymbol{ijk} = -1 \tag{1.46}$$

came to him in a burst of inspiration. In his excitement he carved them into stone at the Brougham Bridge [16]. The story does not elaborate on what his wife was doing meanwhile.

One of the consequences of the defining equation (1.46) is that the basic quaternions $\boldsymbol{i}, \boldsymbol{j}, \boldsymbol{k}$ do not commute. There are different representations of the algebraic structure of quaternions, the most common being in terms of the Pauli matrices (1.2) (see below).

Hamilton spent much of the rest of his life trying to realize the usefulness and beauty of complex numbers in his quaternions. There are strong reasons why that cannot work[17], and thus he was not very successful. So why do we want to use quaternions? For us, the main reason, perhaps, is bookkeeping. The Hamiltonian in a basis which is a direct product of a real space state vector and a two dimensional spin state vector, has a natural decomposition into blocks of 2×2 matrices, which can then be thought of as a single quaternion. Instead of taking the Hamiltonian to be a $2N \times 2N$ complex matrix, one can consider it to be an $N \times N$ matrix of quaternions. What does one gain by doing this? Mainly an economic way of expressing symmetry relations and performing calculations[18].

With this motivation in mind we are ready to dive into the mathematical definitions of quaternions. A quaternion is defined as a linear combination of the 2×2 unit matrix $\mathbb{1}$ and the Pauli spin matrices[19] (1.2) [18]

$$q = q_0 \mathbb{1} + i\boldsymbol{q} \cdot \boldsymbol{\sigma}, \tag{1.47}$$

with $\boldsymbol{q} = (q_1, q_2, q_3)$ a vector of complex numbers, and $\boldsymbol{\sigma} = (\sigma_1, \sigma_2, \sigma_3)$. The *quaternionic complex conjugate*[20] $\tilde{q}$ and *hermitian conjugate* $q^\dagger$ are

[17] For example, the concept of an analytical function has no counterpart.

[18] In random matrix theory calculations, for example, averages over the symplectic ensemble written in terms of quaternions can be translated into averages over the orthogonal ensemble [17].

[19] To make the connection to Hamiltons defining equation (1.46) we note the connection $\boldsymbol{i} = i\sigma_3$, $\boldsymbol{j} = i\sigma_2$ and $\boldsymbol{k} = i\sigma_1$.

[20] This notation is not standard. Most of the time people denote the quaternionic complex conjugate simply with an asterisk. Since the quaternionic complex conjugate differs from the normal complex conjugate, and we will mostly use the latter, we adopt a different notation to avoid confusion.

defined as

$$\tilde{q} = q_0^* + i\boldsymbol{q}^* \cdot \boldsymbol{\sigma} = \sigma_2 q^* \sigma_2, \tag{1.48a}$$

$$q^\dagger = q_0^* - i\boldsymbol{q}^* \boldsymbol{\sigma}. \tag{1.48b}$$

A quaternion is called real if $\tilde{q} = q$. We define the *dual* of a quaternion[21] with

$$q^R = q_0 - i\boldsymbol{q} \cdot \boldsymbol{\sigma} = \sigma_2 q^T \sigma_2. \tag{1.49}$$

For completeness, we mention that the trace of a quaternion is $\operatorname{tr} q = q_0$ (half the normal trace).

The quaternionic complex (hermitian) conjugate $\tilde{Q}$ ($Q^\dagger$) of a quaternionic matrix is the (transpose of the) matrix of the quaternionic complex (hermitian) conjugates

$$(\tilde{Q})_{ij} = \widetilde{(Q_{ij})}, \tag{1.50a}$$

$$(Q^\dagger)_{ij} = (Q_{ji})^\dagger. \tag{1.50b}$$

The dual of a quaternionic matrix $Q^R = (\tilde{Q})^\dagger$. A matrix which equals its dual, is called self-dual. For a hermitian matrix, self-dual and quaternionic real are equivalent. The trace of a quaternionic matrix is $\sum_j \operatorname{tr} Q_{jj}$.

1.2.3 Time Reversal

Having covered some mathematical ground, let us now turn our attention to time reversal symmetry (which we will sometimes refer to as $\mathcal{T}$-symmetry). In some sense, it is better to think of time reversal as being reversal of motion rather than actual reversal of time. The conventional time reversal of a spinless particle reverses its momentum but the position is unchanged.

Let us make this a little bit more abstract by considering Fig. 1.4. We imagine following a path in Hilbert space parameterized by time t. The evolution from state $|\psi(t)\rangle$ to $|\psi(t')\rangle$ is given by the time evolution operator $U(t', t) = \exp[-iH(t' - t)/\hbar]$. The arrows help us remember the

[21] Sometimes called *conjugate quaternion* [18].

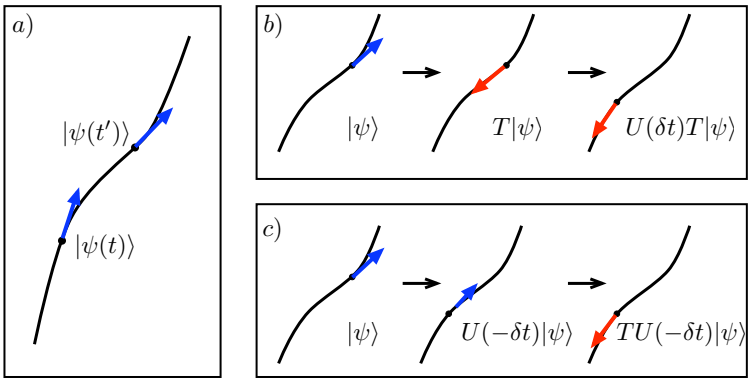

Figure 1.4. Time evolution represented as a flow along a "worldline" in Hilbert space (a). In time reversal symmetric systems, reversing the motion and evolving forward in time (b) is equivalent to evolving backwards in time and then reversing the motion (c). The b (c) panel pictorially represents the left (right) hand side of Eq. (1.51).

"direction" of motion[22]. Applying the time reversal operator T at a given time t_0, reverses the motion of the ket. Therefore if we have time reversal symmetry

$$U(t_0, t_0 + \delta t)T\,|\psi(t_0)\rangle = TU(t_0, t_0 - \delta t)\,|\psi(t_0)\rangle\,. \tag{1.51}$$

This equation reads in words: first reversing the motion and then evolving *forwards* in time, is equivalent to first evolving *backwards* in time and then reversing the motion (cf. Fig. 1.4).

For δt infinitesimal, $U(t_0, t_0 \pm \delta t) = 1 \mp iH\delta t/\hbar$, and since the time reversal relation (1.51) has to be valid for all kets $|\psi(t_0)\rangle$

$$(1 - iH\delta t/\hbar)T = T(1 + iH\delta t/\hbar). \tag{1.52}$$

If T were linear this would mean that $HT = -TH$, and thus for any energy eigenvalue E there would be an accompanying energy eigenvalue

[22]The arrows represent the Hamiltonian flow in Hilbert space, the Hamiltonian being the generator of time translation. It is perfectly fine, for intuition, to imagine the arrows being the direction of momentum.

$-E$. This is clearly a nonsensical result (take for example free electrons which have a strictly positive spectrum). Therefore we need to take T to be antilinear (and antiunitary) and find

$$[H, T] = 0. \tag{1.53}$$

In contrast to a unitary operator that commutes with the Hamiltonian, relation (1.53) does not lead to a conserved quantity. The reason is that because T is antilinear $TU(t, t') \neq U(t, t')T$ even though (1.53) is satisfied. Thus, an eigenstate of T does not necessarily remain an eigenstate of T under time evolution (contrast this with linear and unitary symmetries).

Spinless Systems

In a spinless system, the unitary operator U in $T = U\mathcal{C}$ for the conventional time reversal is simply equal to unity if $\mathcal{C}$ is taken to be with respect to the position basis $\{|x\rangle\}$. To see this consider the action of $\mathcal{C}\hat{x}$ on a general state vector $|\psi\rangle$

$$\mathcal{C}\hat{x}\,|\psi\rangle = \mathcal{C}\int dx\, x\, \psi(x)\,|x\rangle = \int dx\, x\, \psi^*(x)\,|x\rangle = \hat{x}\,\mathcal{C}\,|\psi\rangle\,. \tag{1.54}$$

Similarly for the momentum operator $\hat{p}$ we find

$$\mathcal{C}\hat{p}\,|\psi\rangle = \mathcal{C}\int dx\,(-i\hbar\partial_x\psi)\,|x\rangle = -\int dx\,(-i\hbar\partial_x\psi^*)\,|x\rangle = -\hat{p}\,\mathcal{C}\,|\psi\rangle\,. \tag{1.55}$$

These relations are valid for all $|\psi\rangle$ so the operators have to satisfy

$$\mathcal{C}\hat{x}\,\mathcal{C}^{-1} = \hat{x}, \tag{1.56a}$$
$$\mathcal{C}\hat{p}\,\mathcal{C}^{-1} = -\hat{p}. \tag{1.56b}$$

This is indeed what we want from our time reversal operator, and thus $T = \mathcal{C}$. Note that since $\mathcal{C}^2 = 1$ the time reversal operator squares to one in the spinless case.

Spin $\frac{1}{2}$ System

With the position operator even under time reversal and the momentum operator odd, the orbital angular momentum $\boldsymbol{L} = \boldsymbol{x} \times \boldsymbol{p}$ is clearly odd. Any angular momentum, in particular the spin, should therefore also be odd[23]. Extending the complex conjugation to be with respect to the tensor product $|x\rangle \otimes |\pm\rangle$ of position basis and the eigenstates $|\pm\rangle$ of σ_3, it becomes clear that $\mathcal{C}$ is not sufficient to represent time reversal. We need to find a unitary operator U such that $T\boldsymbol{\sigma}T^{-1} = U\boldsymbol{\sigma}^*U^\dagger = -\boldsymbol{\sigma}$. In components

$$U\sigma_1 U^\dagger = -\sigma_1, \tag{1.57}$$

$$U\sigma_2 U^\dagger = \sigma_2, \tag{1.58}$$

$$U\sigma_3 U^\dagger = -\sigma_3. \tag{1.59}$$

σ_2 does the job, but we are free to choose an accompanying phase. In anticipation of later discussion we will choose the phase such that

$$T = -i\sigma_2\mathcal{C}. \tag{1.60}$$

In this case $T^2 = -1$ while in the spinless case $T^2 = 1$. This generalizes: Systems with integral spin (even number of spin half particles) have a time reversal that squares to 1, while for half integral spin systems (odd number of spin half particles) it squares to -1 [13].

1.2.4 Consequences of Time Reversal for Hamiltonians

From now on we will exclusively consider the consequences of time reversal in spin half systems, or more generally in system were $T^2 = -1$.

Assume that $|E_n\rangle$ is an eigenstate of H with eigenvalue E_n and that H is time reversal symmetric. H and T then commute [cf. Eq. (1.53)], and $T|E_n\rangle$ is also an eigenstate with eigenvalue E_n. Furthermore, using the relation (1.39) and $T^2 = -1$, these two states are seen to be orthogonal

$$\langle E_n|TE_n\rangle = \langle TE_n|T^2E_n\rangle^* = -\langle E_n|TE_n\rangle \tag{1.61}$$

[23] This argument can be made more rigorous by considering the transformation of the total angular momentum $J = L + S$ [14].

i.e. $\langle E_n|TE_n\rangle = 0$. Every eigenvalue of the Hamiltonian is thus necessarily twofold degenerate. This is the Kramers degeneracy (of energy eigenvalues) [11, 12].

The arguments used in (1.61) did not rely on $|E_n\rangle$ being an eigenstate of H, and it thus true that any state $|n\rangle$ is orthogonal to its time reverse $T|n\rangle = |Tn\rangle$. We can thus generally[24] adopt an orthogonal basis set $\{|n\rangle, |Tn\rangle\}$ [15]. What is the form of the time reversal operator in this basis? A general state $|\psi\rangle$ can be written

$$|\psi\rangle = \sum_m (\psi_{m,+}|m\rangle + \psi_{m,-}|Tm\rangle). \tag{1.62}$$

Acting on this state with T (using antilinearity and $T^2 = -1$)

$$T|\psi\rangle = \sum_m (\psi^*_{m,+}|Tm\rangle - \psi^*_{m,-}|m\rangle). \tag{1.63}$$

We notice that T does not couple states with different m. We can thus look at a 2×2 submatrix (quaternion) of T, spanned by the states $|m\rangle$ and $|Tm\rangle$. As usual, writing $T = U\mathcal{C}$ the complex conjugation operator takes care of the complex conjugation. Inspection of Eq. (1.63) then leads us to take

$$U_{nm} = \begin{pmatrix} \langle n|U|m\rangle & \langle n|U|Tm\rangle \\ \langle Tn|U|m\rangle & \langle Tn|U|Tm\rangle \end{pmatrix} = \delta_{nm} \begin{pmatrix} 0 & -1 \\ 1 & 0 \end{pmatrix} = -i\sigma_2\delta_{nm}. \tag{1.64}$$

In the quaternionic notation $U = -i\sigma_2$ (tensor product with the unit matrix is implied) and $T = -i\sigma_2\mathcal{C}$. This agrees with the result (1.60) for the conventional time reversal but is more general.

Writing H in the same basis, time reversal invariance requires the Hamiltonian to be quaternionic real

$$H = THT^{-1} = -i\sigma_2\mathcal{C}H\mathcal{C}i\sigma_2 = \sigma_2 H^*\sigma_2 = \tilde{H}. \tag{1.65}$$

[24] It is relatively straightforward to see that this can always be done. Start with $|1\rangle$ and $|T1\rangle$. Choose $|2\rangle$ orthogonal to $|1\rangle$ and $|T1\rangle$ (for example using the Gram-Schmidt process). Then antiunitarity of T guarantees that $|T2\rangle$ is orthogonal to all the other basis vectors chosen. Continue this process until you have a full basis.

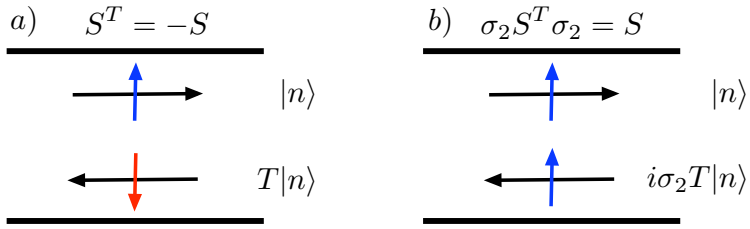

Figure 1.5. A schematic picture of the scattering states used as a basis for the scattering matrix. On the left the outgoing state is the time reverse of the incoming state, while on the left the spin is flipped such that the spin state of the incoming and outgoing states is the same.

Since H is hermitian, this implies that the Hamiltonian is also self-dual $H^R = H$.

1.2.5 Consequences of Time Reversal for Scattering Matrices

The presence of time reversal has implications also for the symmetry of the scattering matrix. The exact way this symmetry is reflected in the scattering matrix depends on the basis chosen. We will here discuss a couple of cases.

Symmetry of S

We consider a conventional two terminal scattering setup with $N_{L(R)}$ modes in the left (right) lead. We will label all incoming states on the left (right) with $|n\rangle$ ($|m\rangle$). The outgoing modes will then be $|Tn\rangle$ ($|Tm\rangle$). A general scattering state $|\varphi\rangle$ will then have the following form in the left lead

$$|\varphi\rangle = \sum_{n=1}^{N_L} (c_n^{\mathrm{in,L}} |n\rangle + c_n^{\mathrm{out,L}} |Tn\rangle), \tag{1.66}$$

and similar for the right lead (with $L \to R$ and $n \to m$). The scattering matrix connects the vectors of coefficients c^{in} to c^{out}

$$\begin{pmatrix} c^{\text{out,L}} \\ c^{\text{out,R}} \end{pmatrix} = S \begin{pmatrix} c^{\text{in,L}} \\ c^{\text{in,R}} \end{pmatrix} = \begin{pmatrix} r & t' \\ t & r' \end{pmatrix} \begin{pmatrix} c^{\text{in,L}} \\ c^{\text{in,R}} \end{pmatrix} \tag{1.67}$$

If we have time reversal symmetry then

$$T\,|\varphi\rangle = \sum_{n=1}^{N_L} [(c_n^{\text{in,L}})^*\,|Tn\rangle - (c_n^{\text{out,L}})^*\,|n\rangle), \tag{1.68}$$

is also a scattering state with the same energy. That means that

$$\begin{pmatrix} (c^{\text{in,L}})^* \\ (c^{\text{in,R}})^* \end{pmatrix} = S \begin{pmatrix} -(c^{\text{out,L}})^* \\ -(c^{\text{out,R}})^* \end{pmatrix}. \tag{1.69}$$

Multiplying from the left with $S^\dagger$, using unitarity of S and complex conjugating

$$\begin{pmatrix} c^{\text{out,L}} \\ c^{\text{out,R}} \end{pmatrix} = -S^T \begin{pmatrix} c^{\text{in,L}} \\ c^{\text{in,R}} \end{pmatrix}. \tag{1.70}$$

We conclude, by comparison with Eq. (1.67), that S is antisymmetric[25]

$$S = -S^T. \tag{1.71}$$

Note that this means that the diagonal elements are zero in agreement with the qualitative discussion of weak antilocalization in Sec. 1.1.3.

The representation (1.71) is most natural from the point of view of time reversal, and it is completely general. It is however rarely, if ever, seen in the literature. To understand why, consider the diagonal elements of the reflection matrix r (see Fig. 1.5). In our representation these elements

[25] In a typical calculation $|n\rangle$ could for example be a plane wave times a spinor. Often one would then want to use the same basis state to be an incoming state on the left and an outgoing state on the right. Thus the scattering state on the left would have the form (1.66) on the left, but on the right $|n\rangle$ and $|Tn\rangle$ would change role. With similar calculation as above, one finds that in this case $S = -\tau_z S^T \tau_z$, with $\tau_z = \begin{pmatrix} 1 & 0 \\ 0 & -1 \end{pmatrix}$ in the block structure of the scattering matrix.

describe processes where a spin up[26] particle is reflected as a spin down particle. In some cases there is only one band (like single-valley graphene) and the direction of the spin is completely tied to the momentum direction, and this is then the only meaningful representation. Quite often though, we have two degenerate bands (leads without spin-orbit coupling), and the most common representation is where a spin up particle is reflected as a spin up particle. We can easily take this into account in our scattering state, simply by flipping the spin of the outgoing mode (using $i\sigma_2$), which then becomes

$$|\varphi\rangle = \sum_{n=1}^{N_L} \sum_{\sigma=\pm} (c_{n,\sigma}^{\mathrm{in,L}} |n,\sigma\rangle + c_{n,\sigma}^{\mathrm{out,L}} i\sigma_2 T |n,\sigma\rangle), \tag{1.72}$$

with $|n,\sigma\rangle = |n\rangle \otimes |\sigma\rangle$ and σ_2 acts on $|\sigma\rangle$. Going through the same calculation that lead to Eq. (1.71), we obtain the well known result that the scattering matrix is self-dual

$$S = \sigma_2 S^T \sigma_2 = S^R. \tag{1.73}$$

Note that this representation is only possible when we have an even number of modes.

Kramers Degeneracy of Transmission Eigenvalues

The Kramers degeneracy of energy eigenvalues in time reversal symmetric systems is intuitively understandable: An electron moving to the left surely has the same energy as a particle moving to the right. The Kramers degeneracy of transmission eigenvalues (eigenvalues of the product $tt^\dagger$ of the matrix t of transmission amplitudes) is much less intuitively clear. In fact, time reversal takes an incoming mode into an outgoing mode, so why should there be any degeneracy. This lack of an intuitive picture plus the absence of a simple proof[27] for this fact has lead to a certain lack

[26] The quantization axis with respect to which *up* is defined depends on the problem at hand and can even depend on the quantum number n.

[27] To quote the authors of Ref. 19: "Note that the proof of the Kramers degeneracy of transmission eigenvalues is by far more complicated than that of the original Kramers theorem for the degeneracy of energy levels".

of appreciation for it, despite it being widely known. In this section we present a new alternative proof for this Kramers degeneracy, given solely in terms of the symmetries of the scattering matrix.

We have seen that in the presence of time reversal the scattering matrix is antisymmetric. In particular the reflection matrix r is antisymmetric $r^T = -r$. A linear algebra theorem [20, 21] states that for any antisymmetric matrix r there exist a unitary matrix W such that $r = W^T D W$, with

$$D = \Sigma_1 \oplus \Sigma_2 \oplus \cdots \oplus \Sigma_k \oplus 0 \oplus \cdots \oplus 0, \tag{1.74}$$

where $2k = \text{rank } r$, $\oplus$ denotes the direct sum and

$$\Sigma_j = \begin{pmatrix} 0 & \lambda_j \\ -\lambda_j & 0 \end{pmatrix}, \quad \lambda_j > 0, \quad j = 1, \cdots, k. \tag{1.75}$$

In other words, D is block diagonal with k 2×2 nonzero blocks Σ_j and $N_L - 2k$ 1×1 zero blocks 0. Clearly if there are odd number of modes (i.e. the dimension of r is odd) there is at least one zero term in the sum (1.74). Using this result, we find that

$$r^\dagger r = W^\dagger D^T D W. \tag{1.76}$$

But since

$$\Sigma_r^T \Sigma_r = \begin{pmatrix} \lambda_r^2 & 0 \\ 0 & \lambda_r^2 \end{pmatrix}, \tag{1.77}$$

we have managed to diagonalize $r^\dagger r$ and found that its eigenvalues come in pairs. Due to unitarity of S, $\mathbb{1} - r^\dagger r$ and $t^\dagger t$ have the same eigenvalues. The transmission eigenvalues are thus twofold degenerate (Kramers degeneracy), plus (if the number of modes is odd) one eigenvalue equal to unity (perfect transmission [22]).

1.3 Model Hamiltonians

In order to demonstrate the theory we have been discussing, we will in this section find the eigenstates and eigenenergies of two model Hamiltonians: The Rashba Hamiltonian of Sec. 1.1.4 and the single valley graphene Dirac

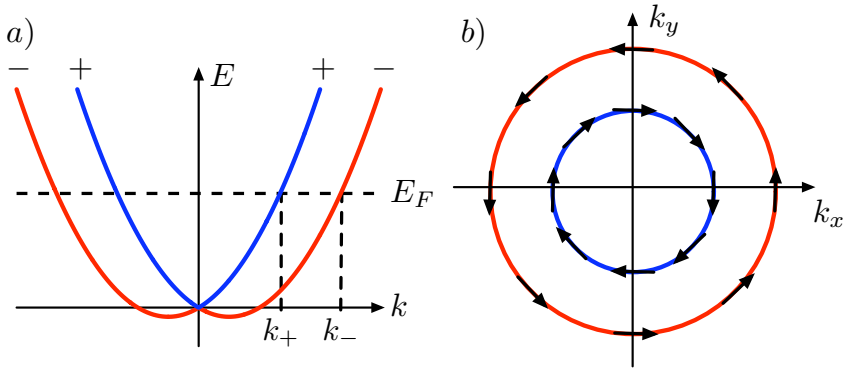

Figure 1.6. (a) The energy band structure of the Rashba Hamiltonian with the definition of the momenta $k_\pm$. (b) The Fermi surface consists of two concentric circles of radius $k_\pm$. The black arrows show the spin direction of the energy eigenstates.

Hamiltonian. In the latter the spin degree of freedom is not the real spin but rather the pseudospin corresponding to a sublattice index of the envelope wavefunction [23–25]. Similarly the time reversal is not the real time reversal but rather another antiunitary symmetry sometimes called effective time reversal.

1.3.1 The Rashba Hamiltonian

As a prototypical example of a simple electronic system with spin-orbit coupling, we consider in this section the Rashba Hamiltonian

$$H_R = \frac{p^2}{2m} + \frac{\alpha}{\hbar}(p_y\sigma_1 - p_x\sigma_2). \tag{1.78}$$

Since H_R commutes with the momentum operator $\boldsymbol{p}$ the eigenstates can be taken to be of the form $|\psi\rangle = |\boldsymbol{k}\rangle \otimes |\chi\rangle$ with $\langle \boldsymbol{x}|\boldsymbol{k}\rangle = \exp(i\boldsymbol{k}\cdot\boldsymbol{x})$. $|\chi\rangle$ is found by diagonalizing H_R for a fixed $\boldsymbol{k} = k(\cos\phi\,\hat{x} + \sin\phi\,\hat{x})$

$$H_R = \frac{\hbar^2 k^2}{2m}\begin{pmatrix} 1 & i\tilde{\alpha}e^{-i\phi} \\ -i\tilde{\alpha}e^{i\phi} & 1 \end{pmatrix}, \tag{1.79}$$

where $\tilde{\alpha} = 2m\alpha/(\hbar^2 k)$. The eigenvalues

$$\varepsilon_\pm = \frac{\hbar k^2}{2m} \pm \alpha k, \tag{1.80}$$

are independent of ϕ and show a zero (magnetic) field spin-splitting (see Fig. 1.6). The eigenstates $|\chi\rangle$ are found to be

$$|\chi_\pm(\phi)\rangle = \frac{1}{\sqrt{2}} \begin{pmatrix} e^{-i\phi/2} \\ \mp i e^{i\phi/2} \end{pmatrix}. \tag{1.81}$$

From these states we find that the direction of the spin,

$$\hat{n}_\pm = \langle \chi_\pm | \boldsymbol{\sigma} | \chi_\pm \rangle = (\pm \sin\phi, \mp \cos\phi, 0), \tag{1.82}$$

is orthogonal to the momentum $\hat{\mathbf{k}} \cdot \hat{n}_\pm = 0$. This can be summarized in the equation

$$\hat{n}_\pm = \pm \hat{\boldsymbol{k}} \times \hat{z}, \tag{1.83}$$

with $\hat{z}$ the unit vector in the z direction. We will sometimes refer to a spin with $\hat{n}_+$ ($\hat{n}_-$) as a plus (minus) spin. For a given energy the Fermi surface consists of two concentric circles with radii (Fig. 1.6)

$$k_\pm = \sqrt{k_{\rm so}^2 + k_F^2} \mp k_{\rm so}, \tag{1.84}$$

with $k_{\rm so} = \alpha m/\hbar$ and $k_F = \sqrt{2mE_F}/\hbar$ the Fermi wavevector. The spin rotates as we go along the circles such that there is no zero field spin polarization, consistent with time reversal symmetry.

A neat way of picturing this is to write the Rashba spin-orbit term as Zeeman splitting with a momentum dependent magnetic field

$$H_R = -\boldsymbol{B}(\boldsymbol{p}) \cdot \boldsymbol{\sigma}; \quad \boldsymbol{B}(p) = \alpha(-p_y, p_x, 0) = -\hbar\alpha\, \boldsymbol{k} \times \hat{z}. \tag{1.85}$$

The spin eigenstate $\left|\chi_{-(+)}\right\rangle$ is (anti)parallel to the field.

It is instructive to see explicitly that transforming a state with the time reversal operator $T = -i\sigma_2 \mathcal{C}$ gives us another eigenstate. In fact

$$T\,|\chi_\pm(\phi)\rangle = \pm\,|\chi_\pm(\phi+\pi)\rangle\,, \tag{1.86}$$

i.e. time reversal connects states on the same Fermi surface circle.

We gained some insight into the role of time reversal by looking at the eigenstates of the Hamiltonian. Being diagonal in that basis, the Hamiltonian is trivially quaternionic real. Let us get a bit more acquainted with the abstract theory of the last section by calculating the Hamiltonian in the states $|\phi, \pm\rangle$ where

$$\langle \boldsymbol{x}|\phi, +\rangle = \exp(i\boldsymbol{k}\cdot\boldsymbol{x}) \begin{pmatrix} \xi_\phi \\ 0 \end{pmatrix}, \tag{1.87a}$$

$$\langle \boldsymbol{x}|\phi, -\rangle = \exp(i\boldsymbol{k}\cdot\boldsymbol{x}) \begin{pmatrix} 0 \\ 1 \end{pmatrix}. \tag{1.87b}$$

The phase factor

$$\xi_\phi = \begin{cases} +1 & 0 \le \phi < \pi \\ -1 & \pi \le \phi < 2\pi \end{cases} \tag{1.88}$$

ensures that

$$T\,|\phi, \pm\rangle = |\phi + \pi, \mp\rangle\,. \tag{1.89}$$

A quaternion of the Hamiltonian in this basis ordered like in (1.64) (with $|n\rangle = |\phi, \pm\rangle$) thus becomes[28]

$$\begin{aligned} H_{\phi+,\phi'-} &= \begin{pmatrix} \langle \phi, +|H|\phi', -\rangle & \langle \phi, +|H|\phi' + \pi, +\rangle \\ \langle \phi + \pi, -|H|\phi', -\rangle & \langle \phi + \pi, -|H|\phi' + \pi, +\rangle \end{pmatrix} \\ &= \alpha k\,(\sin\phi \mathbb{1} + \cos\phi\, i\sigma_3)\delta_{\phi,\phi'}. \end{aligned} \tag{1.90}$$

The rest of the Hamiltonian quaternions are obtained similarly,

$$H_{\phi\pm,\phi'\pm} = \frac{\hbar^2 k^2}{2m}\delta_{\phi,\phi'}\mathbb{1}, \tag{1.91a}$$

$$H_{\phi-,\phi'+} = \alpha k\,(\sin\phi \mathbb{1} - \cos\phi\, i\sigma_3)\delta_{\phi,\phi'} = H^R_{\phi+,\phi'-}. \tag{1.91b}$$

The Hamiltonian is indeed quaternionic real and self-dual as expected.

[28] To avoid double counting in the basis $(\{|\phi, \pm\rangle\,, T\,|\phi, \pm\rangle\})$ we restrict $0 \le \phi, \phi' < \pi$.

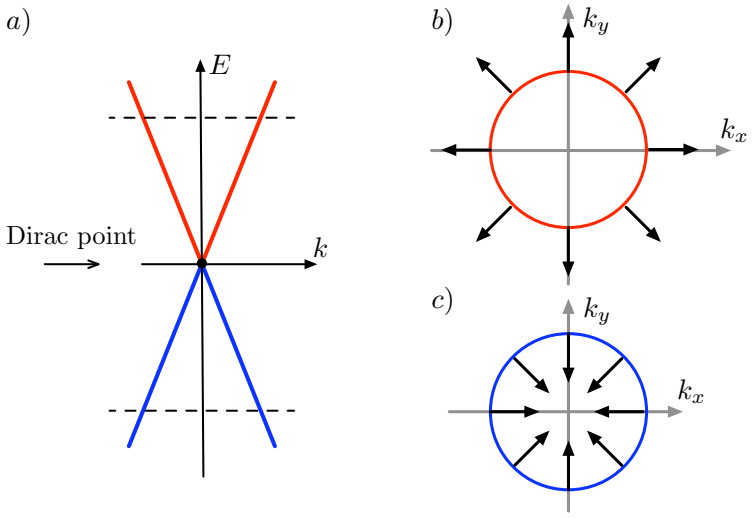

Figure 1.7. (a) The conical energy dispersion relation of a single valley graphene, with the two cones touching at the Dirac point. (b) In the conduction (valence) band the direction of the pseudospin is (anti)parallel to the momentum.

1.3.2 Graphene - the Single Valley Dirac Hamiltonian

In graphene, in the absence of intervalley scattering, the low energy excitations are described by the Dirac Hamiltonian

$$H = v\boldsymbol{p}\cdot\boldsymbol{\sigma} \tag{1.92}$$

with $v \approx c/300$ the velocity of the massless excitations. The energy eigenstates are $\langle \boldsymbol{x}|\varphi,\pm\rangle = \exp(i\boldsymbol{k}\cdot\boldsymbol{x})\,|\chi_\pm(\varphi)\rangle$ with $\boldsymbol{k} = k(\cos\varphi\,\hat{x} + \sin\varphi\,\hat{y})$ and

$$|\chi_\pm(\varphi)\rangle = \frac{e^{\mp i\pi/4}}{\sqrt{2}}\begin{pmatrix}\pm e^{-i\varphi/2}\\ e^{i\varphi/2}\end{pmatrix}. \tag{1.93}$$

With the phase factor $e^{\mp i\pi/4}$ these states satisfy $T\,|\varphi,\pm\rangle = |\varphi+\pi,\pm\rangle$, with $T = -i\sigma_2\mathcal{C}$. The spectrum

$$\varepsilon_\pm = \pm v\hbar k, \tag{1.94}$$

consists of two cones whose apexes meet in a single point called the Dirac point (see Fig. 1.7). The direction of the pseudospin

$$\hat{n}_\pm = \langle \chi_\pm | \boldsymbol{\sigma} | \chi_\pm \rangle = \pm(\cos\varphi, \sin\varphi, 0) = \pm\hat{k} \tag{1.95}$$

is always parallel to the group velocity $\boldsymbol{v}_{g\pm} = \pm v\hat{k}$. Calculating the matrix elements of the Hamiltonian in the basis (1.87) of eigenstates of σ_z in analogous way to the last section, one finds that the Hamiltonian matrix is quaternionic real and self-dual.

1.4 This Thesis

We end this introduction with a brief introduction to the remaining chapters.

Chapter 2: Stroboscopic Model of Transport Through a Quantum Dot with Spin-Orbit Coupling

In the physicist's toolbox, simple models that capture the essential physics and allow for an analytical solution are the best. These are rare. In their absence simple models that capture the essential physics and allow for an efficient numerical simulation are invaluable, be it for the sole purpose of comparing to (often approximate) analytical calculations, or even simulating experiments that can not be conducted in the lab with current technology. A numerical experiment, if you like.

The spin kicked rotator is just such a model; It generalizes the open spinless kicked rotator, which is used to model quantum transport through ballistic quantum dots, to include spin and spin-orbit coupling. The open kicked rotator, in turn, is a generalization of the kicked rotator, which models closed chaotic quantum dots, to model transport. The kicked rotator is a model of a pendulum (or a rotator) that rotates around a fixed point (in the absence of gravity) and is kicked periodically with an essentially random kicking strength. The time dependence is needed, for without it energy would be a constant of the motion and the model would be integrable.

In chapter 2 we introduce the open spin (symplectic) kicked rotator in the traditional way. That is, quantize the Hamiltonian and reduce its one period time evolution operator, the Floquet operator $\mathcal{F}$, to a discrete finite form by going to parameter values that give what is called a resonance. To be consistent with prior literature it is important to do it this way. For physical intuition, however, it is more fruitful to consider the Floquet operator

$$\mathcal{F} = \Pi U X U^{\dagger} \Pi \tag{1.96}$$

as the definition of the model. One then considers the matrix X to describe the free (spin-orbit coupled) motion inside the chaotic cavity. This free motion is interrupted by boundary scattering which is given in terms of the matrix Π. (The matrix X is diagonal in θ space, while Π is diagonal in p-space; U maps between the two spaces. θ and p are conjugate variables.) With this interpretation, the variable θ becomes the momentum-like variable, while p becomes a variable for the position on the boundary. To accommodate the notation it can be useful to think of θ as the angle describing the direction of the momentum.

How one then goes on to open up the model, i.e. attach leads, is described in the chapter. There it is explained how one needs to consider an alternative time reversal symmetry to the one usually used for the spinless kicked rotator. With the above interpretation in mind, the reasons for this are physically clear.

By simply looking at the model, it is by no means clear how to relate its parameters (kicking strengths and symmetry breaking parameters) to a real physical system. With some simple assumptions, we calculate analytically the conductance of the spin kicked rotator, and by varying parameters we can go from weak localization to weak antilocalization, to the absence of weak localization (which happens in the presence of magnetic field). By direct comparison with results from random-matrix theory, one reads off the connection between the model parameters and the physical parameters (magnetic field, spin-orbit coupling time etc.). This is a valuable result for any estimate of physical scales in the model.

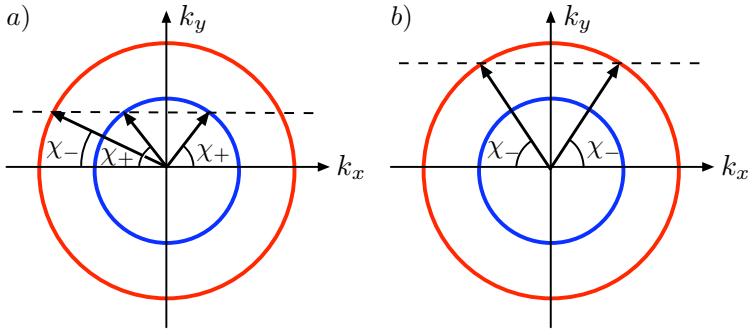

Figure 1.8. A + spin plane wave incident on a hard wall with an incident angle χ_+ (a) is always reflected as two plane waves with reflection angles $\chi_\pm$. A − spin plane wave (b) can, on the other hand, for large enough incident angles be reflected as a single plane wave .

Chapter 3: How Spin-Orbit Coupling Can Cause Electronic Shot Noise

In the absence of spin-orbit coupling, a plane wave incident on a hard wall is reflected as a single plane wave with an angle of reflection equal to the angle of incidence. In the presence of spin-orbit coupling this is no longer true; the plane wave can be reflected as two plane waves.

This can be understood pictorially as shown in Fig. 1.8, were we consider the case that the Fermi surface consists of two concentric circles (as in the Rashba case in Sec. 1.3.1). Assuming that the hard wall is parallel to the y-axis, the y component k_y of the momentum is conserved. If the incoming way belongs to the inner circle (+ spin plane wave) there are two possibilities for the outgoing wave. An incoming wave on the outer circle (− spin) also has two possible outgoing waves, unless the angle of incident χ_- is larger then the critical angle $\chi_c = \arcsin(k_+/k_-)$ with $k_+(k_-)$ the radius of the inner (outer) Fermi circle [cf. Eq. (1.84)]. When there are two outgoing waves, we talk of trajectory splitting [26].

Can this trajectory splitting be a source of (shot) noise in a ballistic quantum dot? That is the question considered in chapter 3. The answer is yes, but to observe it one needs to suppress any other sources of shot noise, in particular the shot noise that arises by the simple fact that the

electron is a wave. Imagine an electron trying to impinge on a lead. If the electron wavepacket is spread over a length scale large then the lead opening, it is going to be partially reflected, causing shot noise. To get rid of this source of noise one needs simply to make the lead very large, such that the spread of the wavepacket is negligible. In this chapter, this condition is given in terms of the Ehrenfest time τ_E, which essentially is the time it takes a wavepacket to spread to the size of the leads. If the dwell time τ_{dwell}, the time the electron spends inside the quantum dot, is smaller then the Ehrenfest time, quantum mechanical wave noise does not play any role.

We establish that in this limit there is a parameter regime were the trajectory splitting is the dominant source of shot noise. To check our theory, we have compared to a numerical simulation of classical particles in a stadium billiard. The trajectory splitting is calculated quantum mechanically, and added to the classical equations of motions to determine what happens as the classical particles are reflected of the boundaries of the billiard. The numerical results are found to be in agreement with our theory.

Chapter 4: Degradation of Electron-Hole Entanglement by Spin-Orbit Coupling

Take a tunnel junction connecting two metals and apply a voltage across it. Every now and then, and electron will tunnel from one side, leaving a hole behind on the other. The electron-hole pair move in opposite directions, creating a current that you can measure; the tunneling current. There is more to this simple process. Namely, the electron and the hole turn out to be entangled [27].

In chapter 4 we consider how the presence of spin-orbit coupling affects this electron-hole entanglement. In order to do so we begin by generalizing an earlier result to include many modes. The reason for this is that the degradation of the entanglement arises because of mode mixing by the spin-orbit coupling.

To quantify the entanglement we use the concurrence. The concurrence depends essentially on two parameters: the number of modes N in the leads connecting the tunnel barrier to the reservoirs, and the ratio $\tau_{\text{dwell}}/\tau_{\text{so}}$ of

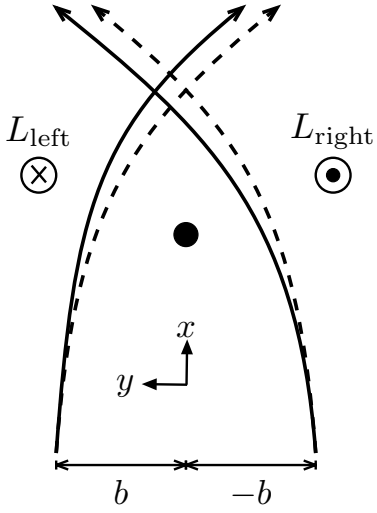

Figure 1.9. A schematic of a scattering of spin up (with respect to z axis) particles by a massive spinless particle (black dot in center). Dashed lines show the symmetric trajectories of electrons with impact parameters b and $-b$, realized when the spin-orbit coupling is neglected. Spin-orbit coupling makes the potential of the scatterer more (less) attractive for particles passing on the right (left), causing a left-right asymmetry in the scattering (solid trajectories).

the time the electron-hole pairs spends in the leads τ_{dwell} and the spin-orbit coupling time τ_{so}. The dependence of the concurrence on both these parameters can be understood intuitively. The more modes there are, the bigger the possibility of mode mixing and the smaller the concurrence. The longer time the modes have to mix, the smaller the concurrence, with τ_{so} setting the time scale on which it goes to zero.

We confirm these expectations numerically, and find in addition that for large number of modes the concurrence is independent of the number of modes. This allows us to make a simplifying assumption (about the form of the spin density matrix) in order to analytically calculate the dependence of the concurrence on the ratio $\tau_{\text{dwell}}/\tau_{\text{so}}$. We find good agreement between our analytical calculation and our numerics.

Chapter 5: Mesoscopic Spin Hall Effect

Let us consider scattering of a spin-half particle by a massive spinless particle [28]. According to our discussion in Sec. 1.1.1 [in particular Eq. (1.7)] the scattering potential the spin-half particle sees will be of the form

$$V_{\text{sc}} = V_0 + V_s(r)\boldsymbol{\sigma} \cdot \boldsymbol{L}. \tag{1.97}$$

Imagine sending in a beam of spin up (with respect to the z-axis) particles with a random impact parameter b. Neglecting the spin-orbit coupling, electrons with impact parameter b and $-b$ will scatter symmetrically (dashed lines in Fig. 1.9). When taking into account the spin-orbit coupling, the electrons passing on the right (left) of the scatterer have an angular momentum parallel (antiparallel) to the spin, and thus feel a stronger (weaker) potential. When averaging over all b we find that spin up electrons have a net tendency to scatter to the left [28]. Spin down electrons on the other hand have a net tendency to scatter to the right. An unpolarized incident beam in the x direction will thus, due to spin-orbit coupling, generate a pure spin current (i.e. not accompanied by a charge current) flowing in the y direction (polarized in the z direction). This, in essence, is the spin Hall effect [29, 30].

The above mechanism is *extrinsic*, coming e.g. from impurities. The *intrinsic* mechanisms for spin-orbit coupling, like the Rashba term, also give arise to a spin Hall effect. To understand this, we recall the representation (1.85) of the Rashba term as a momentum dependent magnetic field. In equilibrium the spin eigenstates are (anti)parallel to this magnetic field, but applying an electric field E_x accelerates the electrons, changing the momentum and in turn the Rashba magnetic field the spin sees. This leads to a precession of the spin out of plane, leading to a spin current $j_{s,y}$ (in the z direction) in analogy to the case discussed above. Referring to Fig. 1.6, the two states at each momentum give a contribution that cancel out. It is thus only the states in the annulus $k_+ < k < k_-$ that contribute, giving a spin Hall conductance [31]

$$\sigma_{sH} = -\frac{j_{s,y}}{E_x} = \frac{e}{8\pi}. \tag{1.98}$$

In the presence of disorder, however, this spin Hall conductance averages to zero [32]. Essentially, the diffusive scattering scrambles the momentum and the Rashba field such that the precession of the spin averages to zero.

In chapter 5 we consider the spin Hall effect in a mesoscopic four terminal chaotic cavity with spin-orbit coupling. The voltages on the terminals are adjusted such that a charge current flows between two longitudinal leads, while no charge current flows in the two transverse leads. In analogy to the two cases discussed above, the spin-orbit coupling gives arise to spin currents in the transverse leads, but the chaotic dynamics (like diffusion) scrambles the momentum such that on average this spin current is zero.

Even though the average spin current is zero, the variance does not need to be. In fact, one expects different cavities to contribute differently to the mean. By changing the chaotic dynamics (e.g. by changing the shape of the cavity) one thus expects spin current fluctuations, very much in analogy to conductance fluctuations. In this chapter we calculate this spin current fluctuations using random-matrix theory, and show that it is universal (in the same sense as universal conductance fluctuations are universal). In order to check our analytical predictions we compare with numerical simulations using the spin kicked rotator of chapter 2.

Chapter 6: One-Parameter Scaling at the Dirac Point in Graphene

Suppose you have a chunk of disordered material of volume L^d with d its dimension. Imagine doubling all the lengths such that the volume becomes $(2L)^d$, made up of 2^d pieces of the original size. Is there a relationship between the conductance of the larger chunk and the conductance of its constituent smaller chunks? According to the scaling theory of localization [33, 34] there is and in fact the rate of change of the dimensionless conductance $g = G/(e^2/h)$ can be written in terms of the beta function

$$\beta(g) = \frac{d \ln g}{d \ln L} \tag{1.99}$$

which depends only on the single parameter g.

In the Drude theory of metals the conductivity σ is a constant and the conductance $G = \sigma L^{d-2}$. For large conductance ($g \gg 1$) we expect the

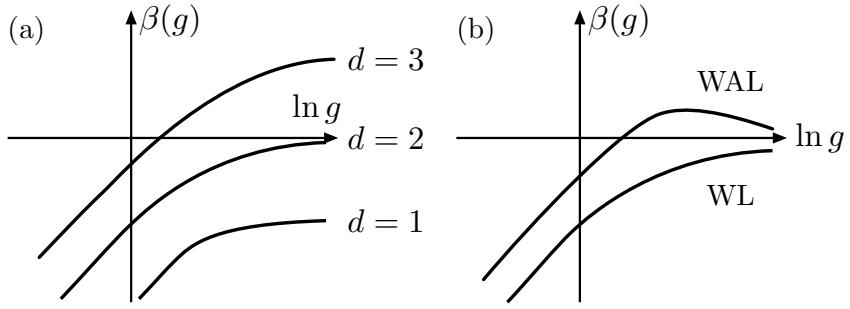

Figure 1.10. (a) A schematic of the beta function of the scaling theory of localization in different dimensions. (b) In two dimension how the beta function approaches zero becomes critical. This is determined by the weak (anti)localization (WL/WAL) correction to the conductivity. In the presence of spin-orbit coupling the beta function approaches zero from above.

Drude theory to be accurate, and thus in this limit

$$\lim_{g\to\infty} \beta(g) = d - 2. \tag{1.100}$$

On the other hand, if the disorder is large enough, the electron wavefunction localizes and the conductance is exponentially small $g \propto \exp(-L/\xi)$ with ξ the localization length. Thus

$$\lim_{g\to 0} \beta(g) = \ln g. \tag{1.101}$$

Assuming that these two limits are connected in a continuous and monotonous manner [33], we obtain the beta functions sketched in Fig. 1.10.

In the two dimensional case, the beta function goes to zero in the limit of large conductance. It therefore is important to know how this limit is approached. This one can do by a perturbation theory around the perfect metal assuming weak disorder. The result is the phenomena of weak (anti) localization discussed in Sec. 1.1.3, but in disordered systems it takes the form [35]

$$\sigma = \sigma_0 - \frac{2-\beta}{\beta}\frac{e^2}{h}\frac{2}{\pi}\ln L/\ell, \tag{1.102}$$

with ℓ the mean free path, and $\beta = 1(4)$ in the absence (presence) of spin-orbit coupling (see also Sec. 2.3). We thus observe that in the presence (absence) of spin-orbit coupling the beta function approaches zero from above (below) as $\beta(g) \sim +1/\pi g$ ($\beta(g) \sim -2/\pi g$).

In graphene, intervalley scattering leads to localization [36, 37]. This means that for system sizes L much larger then the intervalley scattering length $L_{\rm iv}$ graphene becomes an insulator. Intervalley scattering requires that the scattering potential has a Fourier component at a^{-1} with a the lattice spacing. In other words, scattering potential smooth on the scale of lattice spacing does not couple the two valleys of graphene. It turns out the intervalley scattering length in graphene is very large and thus it is of considerable interest to consider what happens in its absence. This is the topic of chapter 6.

Single valley graphene has the same symmetries as a metal with spin-orbit coupling. One might be tempted to conclude that the beta function of these two systems should thus be the same. However, there are several arguments that hint that something completely different is realized. Firstly, consider conductivity at the Dirac point. In the absence of disorder the density of states at the Dirac point is zero and conductance is through evanescent modes. Introduction of disorder will locally change the chemical potential and introduce propagating modes, or in other words disorder will induce a nonzero density of states. Disorder will thus initially increase conductivity. (Another way to think about the same thing is to consider the conductivity enhancement to be due to impurity assisted tunneling [38].) A consequence of this phenomena is that for conductances around the ballistic value the beta function is *positive*.

Secondly, in Refs. 39 and 40 it was shown that the low energy field theory of single valley graphene in the presence of smooth scalar disorder is given in terms of a non-linear sigma model with a topological term. For large conductances the topological term can be neglected and the field theory is the same as for the spin-orbit coupled metal. One thus expects the beta function to approach the limit $1/\pi g$ for $g \gg 1$. We thus have the situation that we have two limits in which the beta function is positive and no theory of how to interpolate between the two limits. One could use the arguments used above expecting the beta function to be monotonous

(which is not always the case, see Fig 1.10) and thus strictly positive. The authors of Ref. 39 gave arguments for a different nonmonotonic scenario in which there is a stable fixed point (as explained in chapter. 6).

In the absence of any analytical tool capable of deciding which beta function is realized, we have developed a numerical method to obtain some evidence for one scenario over the other. In chapter 6 we explain our method and present the results of the numerical simulations. From our results we conclude that the beta function of single valley graphene is strictly positive in contrast to Ref. 39.

Chapter 2

Stroboscopic Model of Transport Through a Quantum Dot with Spin-Orbit Coupling

2.1 Introduction

Electrical conduction in semiconductor heterostructures is affected by the spin degree of freedom through spin-orbit coupling. In quantum dots with chaotic scattering a statistical approach is appropriate. The spin-orbit Hamiltonian (of either Rashba or Dresselhaus form) has a special structure, that of a non-Abelian vector potential. By a gauge transformation Aleiner and Fal'ko identified all possible symmetry classes and described the crossovers between them by means of random-matrix theory (RMT) [41]. This RMT has been extended by Brouwer *et al.* to the case that the spin-orbit coupling is nonuniform and thus the gauge transformation cannot be made [42, 43]. Experiments are in good agreement with the predictions of the theory [44, 45]. Recently a semiclassical theory of quantum dots with spin-orbit coupling has been developed [7, 8]. Exact quantum mechanical calculations of such "Rashba billiards" have also been reported [46]. In this chapter we will focus on the regime of strong chaos,

where RMT and semiclassics agree.

We present a fully quantum mechanical computer simulation to test the theory. In the case of spinless chaotic quantum dots, the stroboscopic model known as the quantum kicked rotator has been proven to be quite successful [47–53]. This model exploits the fact that, although the phase space of the open quantum dot is four-dimensional, the dynamics can be described, on time scales greater than the time of flight across the dot, as a mapping between points on a two-dimensional Poincaré surface of section. The kicked rotator gives a map on a two-dimensional phase space that has the same phenomenology as open quantum dots.

In this chapter we extend the model of the open kicked rotator to include spin-orbit coupling in a perpendicular magnetic field. We begin by describing the known model for a closed chaotic quantum dot [54] with spin-orbit coupling in Sec. 2.2.1, before discussing the opening up of the model in Sec. 2.2.2. The relation of the model to RMT is given in Sec. 2.3. This relation will give us a mapping between the model parameters and the microscopic parameters of a chaotic quantum dot. Numerical results for the weak (anti)-localization peak and its dependence on magnetic field and spin-orbit coupling strength are presented in Sec. 2.4 and compared with the analytical predictions from Sec. 2.3.

2.2 Description of the Model

2.2.1 Closed System

The symplectic kicked rotator has been introduced by Scharf [54] and studied extensively in Refs. 55–57. We summarize this known model of the closed system before proceeding to the open system in the next subsection.

The symplectic kicked rotator describes an electron moving along a circle with moment of inertia I_0, kicked periodically at time intervals τ_0 with a kicking strength that is a function of position and spin. We choose

units such that $\tau_0 \equiv 1$ and $\hbar \equiv 1$. The Hamiltonian H is given by [54, 55]

$$H = \frac{1}{2}(p + p_0)^2 + V(\theta) \sum_{n=-\infty}^{\infty} \delta_s(t - n), \tag{2.1a}$$

$$V(\theta) = K \cos(\theta + \theta_0) + K_{\mathrm{so}}(\sigma_1 \sin 2\theta + \sigma_3 \sin \theta). \tag{2.1b}$$

We have introduced the symmetrized delta function $\delta_s(t) = [\delta(t + \epsilon) + \delta(t - \epsilon)]/2$, with ϵ an infinitesimal. The dimensionless angular momentum operator $p = -i\hbar_{\mathrm{eff}}\partial/\partial\theta$, with $\hbar_{\mathrm{eff}} = \hbar\tau_0/I_0$ the effective Planck constant, is canonically conjugate to the angle $\theta \in [0, 2\pi)$. The kicking potential $V(\theta)$ contains the Pauli spin matrices

$$\sigma_1 = \begin{pmatrix} 0 & 1 \\ 1 & 0 \end{pmatrix}, \quad \sigma_2 = \begin{pmatrix} 0 & -i \\ i & 0 \end{pmatrix}, \quad \sigma_3 = \begin{pmatrix} 1 & 0 \\ 0 & -1 \end{pmatrix}. \tag{2.2}$$

Potential scattering is parameterized by the kicking strength K and spin-orbit coupling by K_{so}. We choose smoothly varying functions of θ, corresponding to a smooth potential. Disorder can be added via a rapidly varying function of θ, cf. Ref. 58.

Spin rotation symmetry is broken if $K_{\mathrm{so}} \neq 0$. The generalized time-reversal symmetry [54]

$$\mathcal{T}: \ \theta \mapsto -\theta, \ \ p \mapsto p, \ \ \sigma_i \mapsto -\sigma_i, \ \ t \mapsto -t, \tag{2.3}$$

is preserved if $\theta_0 = 0$ and is broken if $\theta_0 \in (0, \pi)$. A nonzero p_0 ensures that the Hamiltonian has no other unitary or antiunitary symmetries [54].

Notice that the roles of p and θ are interchanged in $\mathcal{T}$ compared to the conventional time-reversal symmetry of the Rashba Hamiltonian and the spinless kicked rotator, which reads

$$\mathcal{T}': \ \theta \mapsto \theta, \ \ p \mapsto -p, \ \ \sigma_i \mapsto -\sigma_i, \ \ t \mapsto -t. \tag{2.4}$$

For this reason time-reversal symmetry in the symplectic kicked rotator is broken by a displacement of θ, rather than by a displacement of p as in the spinless kicked rotator [59].

The stroboscopic time evolution of a wave function is governed by the

Floquet operator

$$\mathcal{F} = \mathrm{T}\exp\left[-\frac{i}{\hbar_{\mathrm{eff}}}\int_{t_0}^{t_0+1} H(t)dt\right], \tag{2.5}$$

where T denotes time ordering of the exponential. In the range $[-1/2, 1/2)$ only $t_0 = 0$ and $t_0 = -1/2$ preserve $\mathcal{T}$-symmetry for $\theta_0 = 0$. We will find it convenient to choose $t_0 = -1/2$ for numerical calculations and $t_0 = 0$ for analytical work.

For $p_0 = 0$ the reduction of the Floquet operator to a discrete finite form is obtained for special values of $\hbar_{\mathrm{eff}}$, known as resonances [59]. For $\hbar_{\mathrm{eff}} = 4\pi/M$, with M an integer, the Floquet operator is represented by an $M \times M$ matrix of quaternions (cf. Sec. 1.2.2). For this value of $\hbar_{\mathrm{eff}}$ the momentum is restricted to $p \in [0, 4\pi)$, i.e. one can think of the Floquet operator as describing a map on a torus. For $t_0 = -1/2$ the matrix elements in the p-representation are given by

$$\mathcal{F}_{ll'} = (\Pi U X U^{\dagger}\Pi)_{ll'}, \quad l, l' = 0, 1, \ldots, M-1, \tag{2.6a}$$

$$\Pi_{ll'} = \delta_{ll'} e^{-i\pi l^2/M}\mathbb{1}, \tag{2.6b}$$

$$U_{ll'} = M^{-1/2} e^{-i2\pi ll'/M}\mathbb{1}, \tag{2.6c}$$

$$X_{ll'} = \delta_{ll'} e^{-i(M/4\pi)V(2\pi l/M)}. \tag{2.6d}$$

For $t_0 = 0$ one has instead

$$\mathcal{F} = U X^{1/2} U^{\dagger}\Pi^2 U X^{1/2} U^{\dagger}. \tag{2.7}$$

These maps (2.6) and (2.7) are equivalent to the Hamiltonian (2.1) with $p_0 = 0$. A nonzero p_0 may be introduced into the map by replacing Π with [59]

$$\Pi_{ll'} = \delta_{ll'} e^{-i\pi(l+l_0)^2/M}\mathbb{1}, \quad l_0 = \frac{p_0 M}{4\pi}. \tag{2.8}$$

This map is not rigorously equivalent to the Hamiltonian (2.1), but it has the same classical limit (for $K_{\mathrm{so}} = 0$) [51].

The generalized time-reversal symmetry (2.3) is expressed by the identity

$$\mathcal{F} = \mathcal{F}^R, \quad \text{if } \theta_0 = 0. \tag{2.9}$$

The superscript R denotes the dual of a quaternionic matrix (as in Sec. 1.2.2),

$$\mathcal{F}^R \equiv \sigma_2 \mathcal{F}^T \sigma_2.$$

Here T denotes the transpose in the basis of eigenstates of p (p-representation). To verify Eq. (2.9) note that $\sigma_2 \sigma_i^T \sigma_2 = -\sigma_i$ and that the transpose in p-representation takes θ to $-\theta$.

2.2.2 Open System

To describe electrical conduction we open up the kicked rotator, following the general scheme of Refs. 47–50. We model a pair of N-mode ballistic point contacts that couple the quantum dot to electron reservoirs, by imposing open boundary conditions in a subspace of Hilbert space represented by the indices $l_k^{(\mu)}$. The subscript $k = 1, 2, \ldots N$, with $N = N_1 + N_2$, labels the modes (both spin directions), and the superscript $\mu = 1, 2$ labels the point contacts. The $N \times M$ quaternionic projection matrix P is given by

$$P_{kk'} = \begin{cases} \mathbb{1} & \text{if } k' = l_k^{(\mu)}, \\ 0 & \text{otherwise.} \end{cases} \tag{2.10}$$

The matrices P and $\mathcal{F}$ together determine the scattering matrix

$$S(\varepsilon) = P(e^{-i\varepsilon} - \mathcal{F} Q^T Q)^{-1} \mathcal{F} P^T, \tag{2.11}$$

where $\varepsilon \in [0, 2\pi)$ is the quasi-energy and $Q^T Q = 1 - P^T P$. One readily verifies that S is unitary.

We need to ensure that the introduction of the point contacts does not break the $\mathcal{T}$-symmetry

$$S(\varepsilon) = S^R(\varepsilon), \quad \text{if } \theta_0 = 0, \tag{2.12}$$

or for non-zero θ_0 the more general duality relation

$$S(\theta_0) = S^R(-\theta_0). \tag{2.13}$$

This is assured by choosing the absorbing boundary conditions in a strip

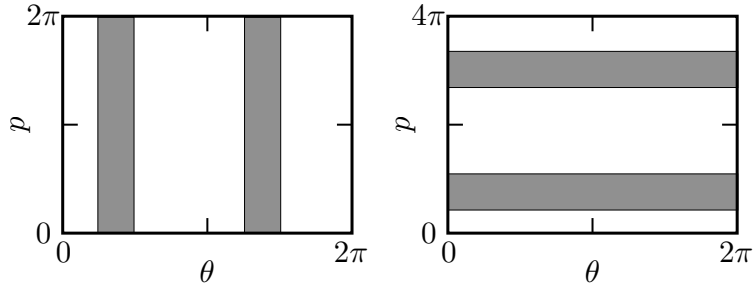

Figure 2.1. Location of the absorbing boundary conditions (grey rectangles) in the classical phase space of the open kicked rotator. To ensure that the openings do not break the time reversal symmetry they are oriented parallel to the p-axis in the spinless kicked rotator (left panel) and parallel to the θ-axis in the symplectic kicked rotator (right panel).

parallel to the θ-axis, rather than parallel to the p-axis as in the spinless kicked rotator (cf. Fig. 2.1). The difference is due to the exchange of the roles of p and θ in the time-reversal symmetry operation, compare Eqs. (2.3) and (2.4).

By grouping together the N_μ indices belonging to the same point contact, the $N \times N$ quaternionic matrix S can be decomposed into 4 sub-blocks containing the quaternionic transmission and reflection matrices,

$$S = \begin{pmatrix} r & t' \\ t & r' \end{pmatrix}. \tag{2.14}$$

The value of ε is arbitrary; we will take $\varepsilon = 0$ in the analytical calculations and average over ε in the numerics. The $\mathcal{T}$-symmetry (2.12) requires that $r = \sigma_2 r^T \sigma_2$, $r' = \sigma_2 r'^T \sigma_2$, and $t' = \sigma_2 t^T \sigma_2$.

The conductance G follows from the Landauer formula

$$G = \frac{e^2}{h} \mathrm{Tr}\ tt^\dagger, \tag{2.15}$$

where the trace Tr is over channel indices as well as spin indices. Unitarity of S ensures that $\mathrm{Tr}\ tt^\dagger = \mathrm{Tr}\ t't'^\dagger$. For $\theta_0 = 0$ the eigenvalues of $tt^\dagger$ are doubly degenerate due to the $\mathcal{T}$-symmetry (Kramers degeneracy, cf.

Sec. 1.2.5). It will prove useful to write the Landauer formula in the form [42, 43]

$$G = \frac{2e^2}{h}\frac{N_1 N_2}{N} - \frac{e^2}{h}\mathrm{Tr} S\Lambda S^\dagger \Lambda \equiv G_0 + \delta G, \tag{2.16}$$

with Λ a diagonal matrix having diagonal elements

$$\Lambda_{jj} = \begin{cases} N_2/N & j = 1, \ldots, N_1, \\ -N_1/N & j = N_1 + 1, \ldots, N. \end{cases} \tag{2.17}$$

The term $G_0 = (2e^2/h)N_1 N_2/N$ is the classical conductance and the term δG, of order e^2/h, is the quantum correction from the weak localization effect.

2.3 Relation to Random-Matrix Theory

Random-matrix theory (RMT) gives universal predictions for the quantum correction δG in Eq. (2.16). We calculate this quantity for the symplectic kicked rotator and compare with RMT. This will give us the relation between the parameters of the stroboscopic model and the microscopic parameters of the quantum dot.

The three universality classes of RMT are labeled by $\beta = 1, 2, 4$, with [60]

$$\delta G_{\mathrm{RMT}} = \frac{\beta - 2}{2\beta}\frac{e^2}{h}. \tag{2.18}$$

In the absence of $\mathcal{T}$-symmetry one has $\beta = 2$. In the presence of $\mathcal{T}$-symmetry one has $\beta = 1$ (4) in the presence (absence) of spin rotation symmetry. We will investigate the three symmetry breaking transitions $\beta = 1 \to 2$, $\beta = 1 \to 4$, and $\beta = 4 \to 2$ in separate subsections.

2.3.1 $\beta = 1 \to 2$ Transition

The $\beta = 1 \to 2$ transition takes place in the absence of spin-orbit coupling ($K_{\mathrm{so}} = 0$). This transition was studied in Ref. 51 for the case that the symmetry $\mathcal{T}'$ rather than $\mathcal{T}$ is broken. To fully characterize the model we

need to reconsider this transition for the case of $\mathcal{T}$-symmetry breaking.

For small θ_0, $\cos(\theta+\theta_0) \approx \cos\theta - \theta_0 \sin\theta$ and the Floquet matrix (2.7) takes the form

$$\mathcal{F}(K_{\rm so}=0,\theta_0\to 0) = e^{\theta_0 W}\mathcal{F}_0 e^{\theta_0 W}, \tag{2.19a}$$

$$W = UYU^\dagger, \quad Y_{ll'} = \delta_{ll'} i(KM/8\pi)\sin(2\pi l/M). \tag{2.19b}$$

Here $\mathcal{F}_0 = \mathcal{F}(K_{\rm so}=0,\theta_0=0)$ is unitary symmetric and W is real antisymmetric. The scattering matrix (2.11) (at $\varepsilon = 0$) becomes

$$S = T(1-\mathcal{F}_0 R)^{-1}\mathcal{F}_0 T', \tag{2.20a}$$

$$T = Pe^{\theta_0 W}, \tag{2.20b}$$

$$T' = e^{\theta_0 W}P^T, \tag{2.20c}$$

$$R = e^{\theta_0 W}Q^T Q e^{\theta_0 W}. \tag{2.20d}$$

Substitution of S into Eq. (2.16) gives the conductance G.

To make contact with RMT we assume that $\mathcal{F}_0$ is a random matrix from the circular orthogonal ensemble (COE), expand the expression for G in powers of $\mathcal{F}_0$ and average $\mathcal{F}_0$ over the COE. In the regime $1 \ll N \ll M$, we can perform the average over the unitary group with the help of the diagrammatic technique of Ref. 17. Since Tr $\Lambda = 0$ only the maximally crossed diagrams contribute to leading order in N. The result for the average quantum correction becomes

$$\langle \delta G\rangle = -\frac{2e^2}{h}\mathrm{tr}\; T^\dagger \Lambda T (T'\Lambda T'^\dagger)^T \frac{1}{M - \mathrm{tr}\; R^\dagger R^T}. \tag{2.21}$$

The factor of 2 comes from the spin degeneracy and the trace tr is over channel indices only. The two remaining traces are evaluated in the limit $N, M \to \infty$ at fixed N/M. We find

$$M^{-1}\mathrm{tr}\; T^\dagger \Lambda T (T'\Lambda T'^\dagger)^T = \frac{N_1 N_2}{N^2}\frac{N}{M}, \tag{2.22}$$

$$M^{-1}\mathrm{tr}\; R^\dagger R^T = 1 - N/M - \theta_0^2 (KM/4\pi)^2 (1-N/M). \tag{2.23}$$

Substitution into Eq. (2.21) gives the average quantum correction

$$\langle \delta G \rangle = -\frac{e^2}{h} \frac{2N_1 N_2}{N^2} \frac{1}{1 + (\theta_0/\theta_c)^2}, \tag{2.24a}$$

$$\theta_c = \frac{4\pi\sqrt{N}}{KM^{3/2}}. \tag{2.24b}$$

The RMT result has the same Lorentzian profile [61, 60]

$$\delta G_{\rm RMT} = -\frac{e^2}{h} \frac{2N_1 N_2}{N^2} \frac{1}{1 + (B/B_c)^2}, \tag{2.25a}$$

$$B_c = C \frac{h}{eL^2} \left(\frac{NL\Delta}{\hbar v_F} \right)^{1/2}, \tag{2.25b}$$

with C a numerical constant of order unity, $L = \sqrt{A}$ the size of the dot, A the area of the dot, $\Delta = 2\pi\hbar^2/mA$ the mean spacing of the Kramers degenerate levels, and v_F the Fermi velocity. Comparison of Eqs. (2.24) and (2.25) allows us to identify

$$\theta_0/\theta_c = B/B_c. \tag{2.26}$$

2.3.2 $\beta = 1 \to 4$ Transition

The $\beta = 1 \to 4$ transition is realized by turning on spin-orbit coupling ($K_{\rm so}$) in the absence of a magnetic field ($\theta_0 = 0$). In this transition the quaternionic structure of the Floquet matrix plays a role. The Floquet matrix (2.7) has the form

$$\mathcal{F}(K_{\rm so}, \theta_0 = 0) = e^{K_{\rm so} A} \mathcal{F}_0 e^{K_{\rm so} A}, \tag{2.27a}$$

$$A = U(\sigma_1 Y_1 + \sigma_3 Y_3) U^\dagger, \tag{2.27b}$$

$$(Y_1)_{ll'} = -\delta_{ll'} i (M/8\pi) \sin(4\pi l/M), \tag{2.27c}$$

$$(Y_3)_{ll'} = -\delta_{ll'} i (M/8\pi) \sin(2\pi l/M). \tag{2.27d}$$

The matrix A is real antisymmetric and thus $\tilde{A} = -A$, where the tilde denotes quaternion complex conjugation (cf. Sec. 1.2.2). The scattering

matrix takes the same form (2.20a), but now with

$$T = Pe^{K_{\rm so}A}, \tag{2.28a}$$
$$T' = e^{K_{\rm so}A}P^T, \tag{2.28b}$$
$$R = e^{K_{\rm so}A}Q^TQe^{K_{\rm so}A}. \tag{2.28c}$$

The average of $\mathcal{F}_0$ over the ensemble of unitary symmetric matrices only involves the channel indices and not the spin indices. To keep the quaternions in the correct order we adopt the tensor product notation of Brouwer *et al.* [42, 43]. The average of δG over $\mathcal{F}_0$ gives, to leading order in N,

$$\langle \delta G\rangle = \frac{e^2}{h}\sum_{\mu\nu}\left[\tau\frac{\text{tr } E\otimes\tilde{E}'}{M\mathbb{1}\otimes\mathbb{1}-\text{tr } R\otimes\tilde{R}}\tau\right]_{\mu\nu;\mu\nu}, \tag{2.29}$$

where $\tau = 1\otimes\sigma_2$, $E = T^\dagger\Lambda T$, and $E' = T'\Lambda T'^\dagger$. The tensor product has a backward multiplication in the second argument,

$$(a\otimes b)(c\otimes d) \equiv ac\otimes db, \tag{2.30}$$

and the indices μ and ν are the spin indices.

The two traces are calculated in the limit $K_{\rm so}\to 0$, $N, M\to\infty$ at fixed N/M, leading to

$$M^{-1}\text{tr } E\otimes\tilde{E}' = \frac{N_1N_2}{N^2}\frac{N}{M}\mathbb{1}\otimes\mathbb{1}, \tag{2.31a}$$
$$M^{-1}\text{tr } R\otimes\tilde{R} = (1-N/M)(1-4K_{\rm so}^2(M/8\pi)^2)\mathbb{1}\otimes\mathbb{1} + 2K_{\rm so}^2(M/8\pi)^2(1-N/M)(\sigma_1\otimes\sigma_1+\sigma_3\otimes\sigma_3). \tag{2.31b}$$

After substitution into Eq. (2.29) there remains a matrix structure that can be inverted, resulting in

$$\langle\delta G\rangle = \frac{e^2}{h}\frac{N_1N_2}{N^2}\left(1-\frac{2}{1+2a^2}-\frac{1}{1+4a^2}\right), \tag{2.32a}$$
$$a = K_{\rm so}/K_c, \quad K_c = \frac{4\pi\sqrt{2N}}{M^{3/2}}. \tag{2.32b}$$

The RMT result has the same functional form [42], with $a^2 = 2\pi\hbar/N\tau_{\rm so}\Delta$.

Here $\tau_{\rm so}$ is the spin-orbit coupling time. Thus we identify

$$K_{\rm so}/K_c = (2\pi\hbar/N\tau_{\rm so}\Delta)^{1/2}. \tag{2.33}$$

2.3.3 $\beta = 4 \longrightarrow 2$ Transition

In the presence of strong spin-orbit coupling ($K_{\rm so} \gg K_c$) the Floquet matrix takes for small θ_0 the same form as in Eq. (2.19a) for $K_{\rm so} = 0$, but now $\mathcal{F}_0 = \mathcal{F}(K_{\rm so} \gg K_c, \theta_0 = 0)$ is a unitary self-dual matrix rather than a unitary symmetric matrix. We can repeat exactly the same steps as we did for $K_{\rm so} = 0$ but with $\mathcal{F}_0$ a random matrix in the circular symplectic ensemble (CSE). We then average $\mathcal{F}_0$ over the CSE. This leads to

$$\langle \delta G \rangle = \frac{e^2}{h} \frac{N_1 N_2}{N^2} \frac{1}{1 + (\theta_0/\theta_c)^2}, \tag{2.34}$$

with θ_c as in Eq. (2.24b). The width of the Lorentzian is therefore the same in the $\beta = 1 \rightarrow 2$ and $\beta = 4 \rightarrow 2$ transitions, in agreement with RMT [60].

2.4 Numerical Results

The numerical technique we use is the same as has been used before for the spinless kicked rotator [50, 51]. A combination of an iterative procedure for matrix inversion and the fast-Fourier-transform algorithm allows for an efficient calculation of the scattering matrix from the Floquet matrix.

The average conductance $\langle G \rangle$ was calculated with the Landauer formula (2.15) by averaging over 60 different uniformly distributed quasi-energies and 40 randomly chosen lead positions. The quantum correction $\langle \delta G \rangle$ is obtained by subtracting the classical conductance G_0. The numerical data is shown in Figs. 2.2 and 2.3. The magnetic field parameter θ_0 is given in units of θ_c from Eq. (2.24b) and the spin-orbit coupling strength parameter $K_{\rm so}$ is given in units of K_c from Eq. (2.32b). The solid lines are the analytical predictions (2.24), (2.32), and (2.34) without any fitting parameter.

The small difference between the data and the predictions can be at-

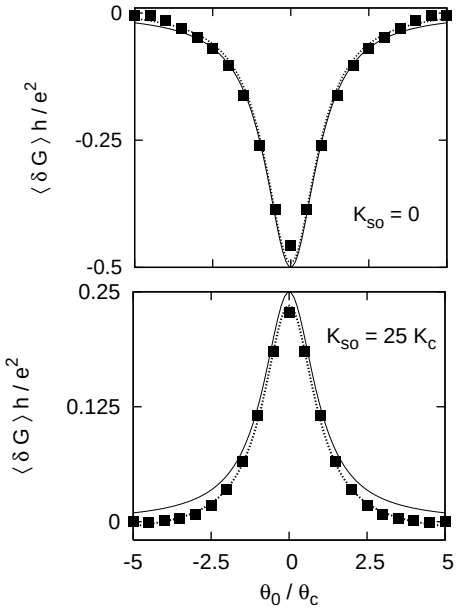

Figure 2.2. Average quantum correction $\langle \delta G \rangle$ to the conductance as a function of the $\mathcal{T}$-symmetry breaking parameter θ_0. The data points are for the symplectic kicked rotator characterized by $K = 41$, $M = 500$, $N_1 = N_2 = 10$, $l_0 = 0.2$. The solid lines are the analytical predictions (2.24) and (2.34) in the absence and presence of spin-orbit coupling. The dotted lines are the solid lines with a vertical offset, to account for a difference between the predicted and actual value of the classical conductance G_0.

tributed to an uncertainty in the value G_0 of the classical conductance. A small vertical offset (corresponding to a change in G_0 of about 0.1%) can correct for this (dotted lines in Fig. 2.2). The strongly non-Lorentzian lineshape seen by Rahav and Brouwer [52, 53] in the spinless kicked rotator is not observed here.

2.5 Conclusion

We have presented a numerically highly efficient model of transport through a chaotic ballistic quantum dot with spin-orbit coupling, extending the earlier work on the spinless kicked rotator. Through a simple assumption of

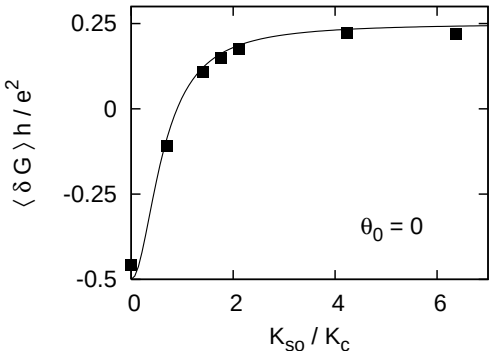

Figure 2.3. Average quantum correction $\langle \delta G \rangle$ to the conductance as a function of spin-orbit coupling strength K_{so} at zero magnetic field. Other parameters are the same as in Fig. 2.2. The solid line is the analytical prediction (2.32) for the crossover from weak localization to weak anti-localization.

a random Floquet matrix we have derived analytical predictions for the conductance of the model as a function of spin-orbit coupling strength and magnetic field. The functional form of the conductance coincides with random-matrix theory (RMT) and through this correspondence we obtain a mapping from microscopic parameters to model parameters. Numerical calculations are in good agreement with the analytical predictions.

In this chapter we have applied the model in a parameter regime where the transport properties of the system are analytically known through RMT, in order to test the validity of the model. In future work this model may provide a starting point for studies of transport properties in parameter regimes where RMT is known to break down. In certain cases, for example in the study of the effect of a finite Ehrenfest time on weak anti-localization, very large system sizes are required (cf. Refs. 52 and 53). An efficient dynamical model, as the one presented in this chapter, is then a valuable tool.

Chapter 3

How Spin-Orbit Coupling can Cause Electronic Shot Noise

3.1 Introduction

Electrical conduction is not much affected typically by the presence or absence of spin-orbit coupling. A familiar example [5, 42, 44, 7], the crossover from weak localization to weak anti-localization with increasing spin-orbit coupling strength, amounts to a relatively small correction to the classical conductance, of the order of the conductance quantum e^2/h. The relative smallness reflects the fact that the spin-orbit coupling energy $E_{\rm so}$ is much smaller than the Fermi energy E_F, basically because $E_{\rm so}$ is a relativistic correction (cf. Ch. 1).

In this chapter we identify an effect of spin-orbit coupling on the electrical current that has a quantum mechanical origin (like weak anti-localization), but which is an order-of-magnitude effect rather than a correction. The effect is the appearance of shot noise in a ballistic chaotic quantum dot with a large number N of modes in the point contacts.

3.2 The Effect of Spin-Orbit Coupling on the Ehrenfest Time

According to recent theory [62–65] and experiment [66], the shot noise without spin-orbit coupling is suppressed exponentially $\propto \exp(-\tau_E/\tau_{\rm dwell})$ when the Ehrenfest time $\tau_E \simeq \lambda_L^{-1} \ln N$ becomes greater than the mean dwell time $\tau_{\rm dwell}$ of an electron in the quantum dot. (The coefficient λ_L is the Lyapunov exponent of the classical chaotic dynamics.) The suppression occurs because electrons follow classical deterministic trajectories up to τ_E (in accord with Ehrenfest's theorem, hence the name "Ehrenfest time"). If $\tau_E > \tau_{\rm dwell}$ an electron wave packet entering the quantum dot is either fully transmitted or fully reflected, so no shot noise appears [67].

The electron spin of $\pm\frac{1}{2}\hbar$ remains quantum mechanical in the limit $N \to \infty$. In the presence of spin-orbit coupling the quantum mechanical uncertainty in the spin of the electron is transferred to the position, causing a breakdown of the deterministic classical dynamics and hence causing shot noise. The mechanism for the spin-orbit-coupling-induced shot noise is illustrated in Fig. 3.1 (cf. also Sec. 1.4). The key ingredient is the splitting of a trajectory upon reflection with a hard boundary [26].

Whether a boundary is "hard" or "soft" depends on the relative magnitude of the penetration depth ξ into the boundary and the spin-orbit precession length $l_{\rm so} = hv_F/E_{\rm so} \simeq \lambda_F E_F/E_{\rm so}$. A soft boundary has $\xi \gg l_{\rm so}$, so the spin evolves adiabatically during the reflection process [26, 68] and the electron remains in the same spin band, without splitting of the trajectory. In the opposite regime $\xi \ll l_{\rm so}$ of a hard boundary the spin is scattered into the two spin bands by the reflection process. The energy splitting $E_{\rm so}$ of the spin bands at the Fermi level amounts to a difference $\delta p_\perp \simeq E_{\rm so}/v_F$ of the component of the momentum perpendicular to the boundary, and hence to a splitting of the trajectories by an angle $\delta\phi_{\rm so} \simeq \delta p_\perp/p_F \simeq \lambda_F/l_{\rm so}$. (A precise calculation of the splitting, which depends on the angle of incidence, will be given later.)

Because of the chaotic dynamics, the angular opening $\delta\phi_{\rm so}(t) \simeq (\lambda_F/l_{\rm so}) \times e^{\lambda_L t}$ of a pair of split trajectories increases exponentially with time t — until they leave the dot through one of the two point contacts after a time T. The splitting will not prevent the trajectories to exit together through

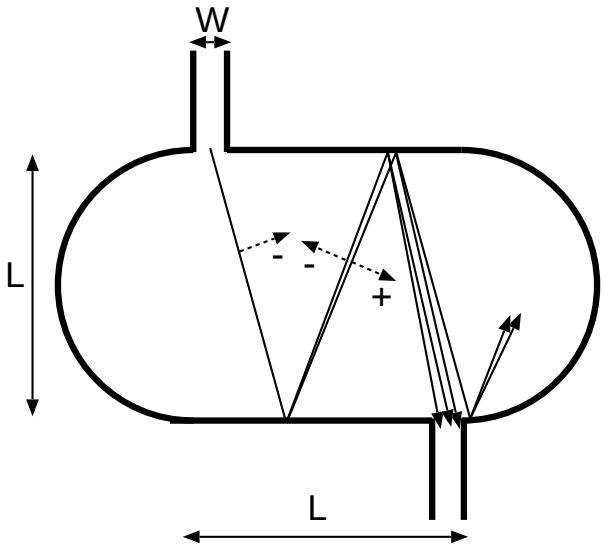

Figure 3.1. Splitting of trajectories by spin-orbit coupling in an electron billiard. (The dotted arrows indicate the spin bands, with ± spins.) The splitting produces shot noise if not all trajectories can exit through the same opening.

the same point contact if $\delta\phi_{\rm so}(T) < W/L$, with W the width of the point contact and L the diameter of the (two-dimensional) quantum dot. The time

$$T_{\rm so} = \lambda_L^{-1} \ln(W l_{\rm so}/L\lambda_F) \tag{3.1}$$

at which $\delta\phi_{\rm so}(T_{\rm so}) = W/L$ is an upper bound for deterministic noiseless dynamics due to spin-orbit coupling.

Dwell times shorter than $T_{\rm so}$ may yet contribute to the shot noise as a result of diffraction at the point contact, which introduces an angular spread $\delta\phi_{\rm pc} \simeq 1/N \simeq \lambda_F/W$ in the scattering states. The time

$$T_{\rm pc} = \lambda_L^{-1} \ln(WN/L) \tag{3.2}$$

at which this angular spread has expanded to W/L is an upper bound for deterministic noiseless dynamics due to diffraction at the point contact [63]. The smallest of the two times $T_{\rm so}$ and $T_{\rm pc}$ is the Ehrenfest time of

this problem,

$$\tau_E = \lambda_L^{-1} \ln\bigl[(W/L)\min(N, l_{\rm so}/\lambda_F)\bigr], \tag{3.3}$$

separating deterministic noiseless dynamics from stochastic noisy dynamics. (By definition, $\tau_E \equiv 0$ if the argument of the logarithm is < 1.) Since the distribution of dwell times $P(T) \propto \exp(-T/\tau_{\rm dwell})$ is exponential, a fraction $\int_{\tau_E}^{\infty} P(T)\,dt = \exp(-\tau_E/\tau_{\rm dwell})$ of the electrons entering the quantum dot contributes to the shot noise.

Following this line of argument we estimate the Fano factor F (ratio of noise power and mean current) as [62] $F = \frac{1}{4}\exp(-\tau_{\rm E}/\tau_{\rm dwell})$, hence

$$F = \frac{1}{4}\left(\frac{\lambda_F L}{l_{\rm so} W}\right)^{1/\lambda_L \tau_{\rm dwell}} \quad \text{if} \quad \frac{\lambda_F L}{W}, \xi < l_{\rm so} < W. \tag{3.4}$$

The upper bound on $l_{\rm so}$ indicates when diffraction at the point contact takes over as the dominant source of shot noise, while the two lower bounds indicate when full shot noise has been reached (Fano factor 1/4) and when the softness of the boundary (penetration depth ξ) prevents trajectory splitting by spin-orbit coupling.

Eq. (3.4) should be contrasted with the known result in the absence of spin-orbit coupling [62, 63]:

$$F = \frac{1}{4}\left(\frac{L}{NW}\right)^{1/\lambda_L \tau_{\rm dwell}} \quad \text{if} \quad \frac{\lambda_F L}{W} < W < l_{\rm so}. \tag{3.5}$$

Clearly, the role of the channel number N in determining the shot noise is taken over by the ratio $l_{\rm so}/\lambda_F$ once $l_{\rm so}$ becomes smaller than W.

3.3 Numerical Simulation in a Stadium Billiard

We support our central result (3.4) with computer simulations, based on the semiclassical theory of Refs. 69–71. In the limit $\lambda_F \to 0$ at fixed $l_{\rm so}, L, W$ a description of the electron dynamics in terms of classical trajectories is appropriate. For the spin-orbit coupling term we take the Rashba Hamiltonian,

$$H_{\rm Rashba} = (E_{\rm so}/2p_F)(p_y\sigma_1 - p_x\sigma_2), \tag{3.6}$$

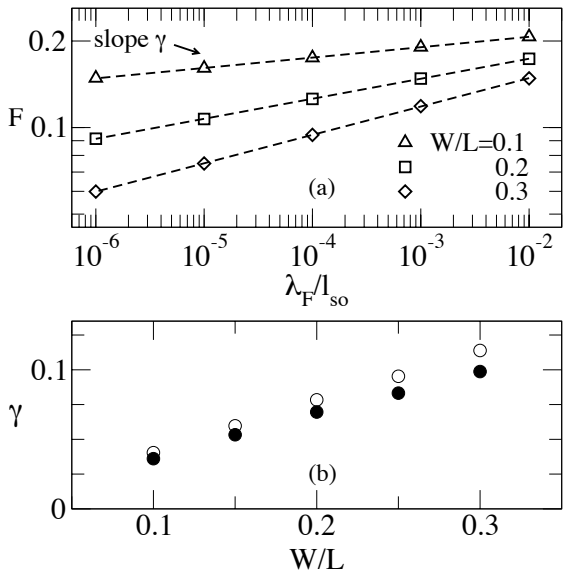

Figure 3.2. (a) Dependence of the Fano factor on the spin-orbit coupling strength for different widths of the opening in the billiard. The data points are calculated from Eq. (3.10). The linear fits in the log-log plot (dashed lines) confirm the predicted scaling $\log_{10} F \propto \log_{10}(\lambda_F/l_{\rm so})$. (b) Filled circles: slope $\gamma = d\log_{10} F/d\log_{10}(\lambda_F/l_{\rm so})$ extracted from Fig. 3.2a. The empty circles are the theoretical prediction $\gamma = 1/\lambda_L \tau_{\rm dwell}$.

with Pauli matrices σ_1 and σ_2. The two spin bands correspond to eigenstates of the spin component perpendicular to the direction of motion $\hat{p}$ in the $x-y$ plane (dotted arrows in Fig. 3.1). The spin direction $\hat{n}_\pm$ of a $\pm$ spin is defined by $\hat{n}_\pm \times \hat{p} = \pm\hat{z}$ (cf. Eq. (1.83)). The corresponding wave vectors are

$$k_\pm = \sqrt{k_F^2 + k_{\rm so}^2} \mp k_{\rm so}, \tag{3.7}$$

with $k_{\rm so} = E_{\rm so}/2v_F\hbar = \pi/l_{\rm so}$.

We consider the stadium-shaped billiard shown in Fig. 3.1 with hard-wall confinement ($\xi \to 0$). Since $\lambda_F \ll L$ we can neglect the curvature of the boundary when calculating the splitting of the trajectories by spin-orbit coupling [26]. The two reflection angles $\chi_\pm \in (0, \pi/2)$ of the split trajectory, measured relative to the inward pointing normal, are related by conservation of the momentum component parallel to the boundary,

$$k_+ \sin\chi_+ = k_- \sin\chi_-. \tag{3.8}$$

An incident trajectory of with a $-$ spin is not split near grazing incidence, if $\chi_- > \arcsin(k_+/k_-) \approx \pi/2 - 2\sqrt{k_{\rm so}/k_{\rm F}}$. Away from grazing incidence the probability $R_{\sigma\sigma'} = |r_{\sigma\sigma'}|^2$ for an electron incident with σ' spin at an angle $\chi_{\sigma'}$ to be reflected with with σ spin at an angle χ_σ is determined by the 2×2 unitary reflection matrix

$$r = \begin{pmatrix} r_{++} & r_{+-} \\ r_{-+} & r_{--} \end{pmatrix}, \tag{3.9a}$$

$$r_{++} = \frac{e^{i\chi_+} - e^{-i\chi_-}}{e^{-i\chi_+} + e^{-i\chi_-}}, \quad r_{--} = \frac{e^{i\chi_-} - e^{-i\chi_+}}{e^{-i\chi_+} + e^{-i\chi_-}}, \tag{3.9b}$$

$$r_{+-} = -\frac{2\sqrt{\cos\chi_+ \cos\chi_-}}{e^{-i\chi_+} + e^{-i\chi_-}} = r_{-+}. \tag{3.9c}$$

The reflection matrix refers to a basis of incident and reflected plane waves that carry unit flux perpendicular to the boundary, calculated using the proper spin-dependent velocity operator [72].

By following the classical trajectories in the stadium billiard, and splitting them upon reflection with probabilities $R_{\sigma\sigma'}$, we calculate the probability $f(x, y, \hat{p})$ that an electron at position x, y with direction $\hat{p}$ of its

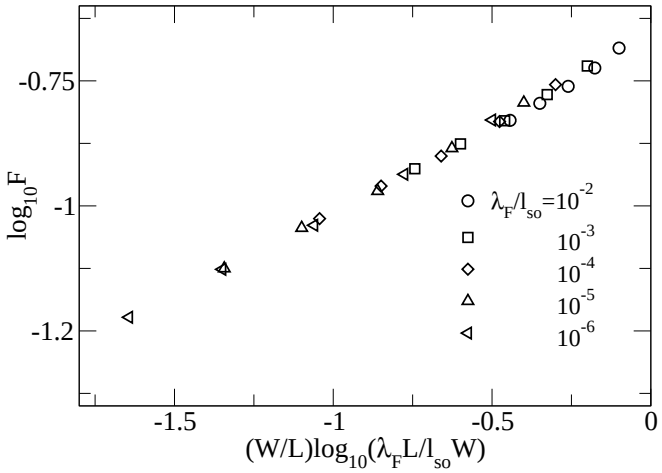

Figure 3.3. Dependence of the Fano factor on W/L for different fixed values of $\lambda_F/l_{\rm so}$. The data points follow closely the predicted scaling $\log_{10} F \propto (W/L)\log_{10}(\lambda_F L/l_{\rm so}W)$.

momentum originated from the upper left opening[1]. The Fano factor is then given by [69–71]

$$F = \frac{\int d\Omega\, f(1-f)}{2\int d\Omega\, f}, \tag{3.10}$$

where $d\Omega = dx\, dy\, d\hat{p}$.

The results of the simulations are presented in Figs. 3.2 and 3.3. We first varied $\lambda_F/l_{\rm so}$ at fixed W/L to test the scaling $F \propto (\lambda_F/l_{\rm so})^{1/\lambda_L \tau_{\rm dwell}}$ predicted by Eq. (3.4). We kept $\lambda_F/l_{\rm so} \ll 1$, to ensure that the classical Lyapunov exponent $\lambda_L = 0.86\, v_F/L$ [73] and mean dwell time $\tau_{\rm dwell} \propto L^2/v_F W$ (calculated numerically) are not affected significantly by the spin-orbit coupling. The log-log plot in Fig. 3.2a confirms the scaling $\log_{10} F \propto \log_{10}(\lambda_F/l_{\rm so})$. The slope γ, plotted in Fig. 3.2b as a function of W/L (filled circles), is close to the predicted theoretical value $\gamma = 1/\lambda_L \tau_{\rm dwell}$ (empty

[1]It is equivalent and computationally more efficient to use Birkhoff coordinates $s, p_\parallel$, with s the position along the boundary and $p_\parallel$ the component of the momentum parallel to the boundary. Then Eq. (3.10) holds with $d\Omega = ds\, dp_\parallel$.

circles) if the ratio W/L becomes sufficiently small. There is no adjustable parameter in this comparison of theory and simulation. We then tested the scaling $F \propto (L/W)^{1/\lambda_L \tau_{\rm dwell}}$ at fixed $\lambda_F/l_{\rm so}$. The data points in Fig. 3.3 all fall approximately on a straight line, confirming the predicted scaling law $\log_{10} F \propto (W/L) \log_{10}(\lambda_F L/l_{\rm so} W)$.

This completes our test of the scaling (3.4) in the regime $l_{\rm so} \ll W$. The scaling (3.5), in the opposite regime $l_{\rm so} \gg W$, was verified in Ref. 50 using the quantum kicked rotator. We have tried to observe the crossover from the scaling (3.4) to (3.5) in that model, but were not successful — presumably because we could not reach sufficiently large system size.

3.4 Conclusion

In conclusion, we have identified and analyzed a mechanism by which spin-orbit coupling in a ballistic system can produce electronic shot noise. The origin of the current fluctuations is a quantum mechanical effect, the splitting of trajectories, which persists in the limit of classical orbital dynamics. Since the strength of the Rashba spin-orbit coupling can be varied by a gate voltage in a two-dimensional electron gas [74], the most natural way to search for the effect would be to measure the shot noise as a function of the spin-orbit precession length $l_{\rm so}$. One would then see an increase in the Fano factor with decreasing $l_{\rm so}$, starting when $l_{\rm so}$ drops below the point contact width W. Since the splitting of trajectories requires $l_{\rm so}$ to be larger than the boundary penetration depth ξ, the noise would go down again when $l_{\rm so}$ drops below ξ (assuming $\xi \ll W$). This non-monotonic dependence of the noise on the spin-orbit coupling strength would be an unambiguous signature to search for in an experiment. In order to observe the effect an experimental system should be sufficiently clean to guarantee that the noise induced by quantum short-range disorder [71] is weak enough.

Chapter 4

Degradation of Electron-Hole Entanglement by Spin-Orbit Coupling

4.1 Introduction

Spin-orbit coupling is one of the sources of degradation of spin entanglement that has been extensively investigated for electron pairs confined to two quantum dots [75]. In that context the spin-orbit coupling induces dephasing by coupling the electron spins via the orbital motion to fluctuating electric fields in the environment (due to lattice vibrations or gate voltage fluctuations). The coupling of the spins to the environment is needed for entanglement degradation because the spin-orbit coupling by itself amounts to a local unitary transformation of the electron states in the two quantum dots, which cannot change the degree of entanglement.

The characteristic feature of these quantum dots is that they are single-channel conductors with a conductance G that is small compared to the conductance quantum e^2/h. This implies in particular that the width of the energy levels is much smaller than the mean level spacing. At low voltages and temperatures there is then only a single accessible orbital mode. This is the main reason that spin-orbit coupling by itself cannot degrade the spin entanglement.

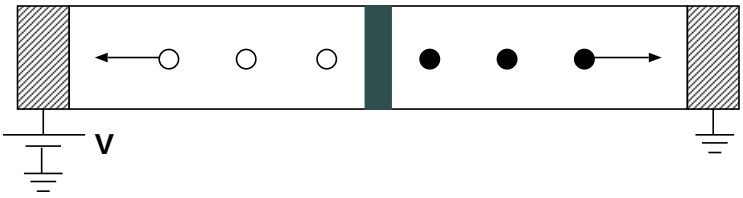

Figure 4.1. Multi-channel conductor containing a tunnel barrier. The applied voltage creates electron-hole pairs (solid and open circles) at opposite side of the barrier, whose spin state is maximally entangled. As the pair moves through the leads, the spin and orbital degrees of freedom become entangled by the spin-orbit coupling, degrading the spin entanglement upon tracing out the orbital degrees of freedom.

In a multi-channel conductor the situation is altogether different. Flying qubits in a multi-channel conductor can lose their entanglement as a result of spin-orbit coupling even in the absence of electric field fluctuations, because the large number of orbital degrees of freedom can play the role of an environment. This mechanism is the electronic analog of the loss of polarization entanglement by polarization-dependent scattering in quantum optics [76–78]. Fully-phase-coherent spin-orbit coupling can degrade the spin entanglement by reducing the pure spin state to a mixed spin density matrix — which typically has less entanglement than the pure state. Here we investigate this mechanism in the context of electron-hole entanglement in the Fermi sea [27]. Apart from the practical significance for the observability of the entanglement, this study provides a test for a theory of entanglement transfer based on the "isotropy approximation" that the spin state has no preferential quantization axis.

The system we consider, a multi-channel conductor containing a tunnel barrier, is schematically depicted in Fig. 4.1. The applied voltage V creates, at each tunnel event, a maximally entangled electron-hole pair [79]. Spin-orbit coupling in the leads entangles the spin and orbital degrees of freedom. The spin state (obtained by tracing out the orbital degrees of freedom) is degraded from a pure state to a mixed state. The degree of entanglement of the spin state decreases and can vanish for strong spin-orbit coupling. We consider two cases. In the first case the leads are diffusive

wires while in the second case we model the leads as two chaotic cavities. Although the first case is our primary interest, we include the second case in order to test our approximate analytical calculations against an exact numerical simulation of the spin kicked rotator (cf. chapter 2).

The outline of this chapter is as follows. In Sec. 4.2 we calculate the density matrix of the electron-hole pairs in the regime where the tunnel conductance G_{tunnel} is $\ll e^2/h$. This is the regime in which the electron-hole pairs form well separated current pulses, so that their entanglement can be measured easily [27]. (For $G_{\text{tunnel}} \gtrsim e^2/h$ different electron-hole pairs overlap in time, complicating the detection of the entanglement.) From the density matrix we seek, in Sec. 4.3, the degree of entanglement as measured by the concurrence [80]. For our analytical treatment we approximate the density matrix by the spin-isotropic Werner state [81]. The absence of a preferential basis in spin space is a natural assumption for a disordered or chaotic system, but it needs to be tested. For that purpose we use the spin kicked rotator, which as explained in Ch. 2 is a stroboscopic model of a chaotic cavity. We conclude in Sec. 4.4.

4.2 Calculation of the Electron-Hole State

4.2.1 Incoming and Outgoing States

Since the scattering of both orbital and spin degrees of freedom is elastic, we may consider separately each energy E in the range $(E_{\text{F}}, E_{\text{F}}+eV)$. For ease of notation we will omit the energy arguments in what follows. We assume zero temperature, so the incoming state is

$$|\Psi_{\text{in}}\rangle = \prod_{\nu=1}^{2N} a^{\dagger}_{L,\nu}\,|0\rangle\,. \tag{4.1}$$

The creation operators $a^{\dagger}_{L,\nu}$, $\nu = 1,\ldots,2N$ (acting on the true vacuum $|0\rangle$) occupy the ν-th channel incoming from the left. The index ν labels both the N orbital and two spin degrees of freedom. The $2N$ channels incoming from the right (creation operators $a^{\dagger}_{R,\nu}$) are unoccupied in the energy range $(E_{\text{F}}, E_{\text{F}}+eV)$. We collect the creation and annihilation operators

in vectors $\mathbf{a}_L = (a_{L,1}, a_{L,2}, \ldots, a_{L,2N})$, $\mathbf{a}_R = (a_{R,1}, a_{R,2}, \ldots, a_{R,2N})$.

The annihilation operators $b_{L,\nu}$ and $b_{R,\nu}$ of the outgoing channels are related to those of the incoming channels by the scattering matrix

$$\begin{pmatrix} \mathbf{b}_L \\ \mathbf{b}_R \end{pmatrix} = S \begin{pmatrix} \mathbf{a}_L \\ \mathbf{a}_R \end{pmatrix} = \begin{pmatrix} r & t' \\ t & r' \end{pmatrix} \begin{pmatrix} \mathbf{a}_L \\ \mathbf{a}_R \end{pmatrix}. \tag{4.2}$$

The $4N \times 4N$ unitary scattering matrix S is decomposed into $2N \times 2N$ transmission and reflection matrices t, t', r, and r'. Substitution into Eq. (4.1) gives the outgoing state

$$|\Psi_{\text{out}}\rangle = \prod_{\nu=1}^{2N} \left(\sum_{\nu'=1}^{2N} \left[b^\dagger_{L,\nu'} r_{\nu'\nu} + b^\dagger_{R,\nu'} t_{\nu'\nu} \right] \right) |0\rangle \,. \tag{4.3}$$

4.2.2 Tunneling Regime

We expand the outgoing state (4.3) in the small parameter $\epsilon = (h/e^2) G_{\text{tunnel}}$, neglecting terms of order ϵ and higher. Since t, t' are $\mathcal{O}(\epsilon^{1/2})$ while r, r' are $\mathcal{O}(\epsilon^0)$, we keep only terms linear in t and t'. The result is

$$|\Psi_{\text{out}}\rangle = |0_{\text{F}}\rangle + \sum_{\nu,\mu} (t r^\dagger)_{\nu\mu} b^\dagger_{R,\nu} b_{L,\mu} |0_{\text{F}}\rangle + \mathcal{O}(\epsilon), \tag{4.4}$$

where $|0_{\text{F}}\rangle$ is the unperturbed Fermi sea,

$$|0_{\text{F}}\rangle = \det(r) \prod_{\nu=1}^{2N} b^\dagger_{L,\nu} |0\rangle \,. \tag{4.5}$$

Since $r r^\dagger = \mathbb{1} - \mathcal{O}(\epsilon)$, we may assume that r is a unitary matrix to the order in ϵ considered. The determinant $\det(r)$ is therefore simply a phase. The state (4.4) is a superposition of the unperturbed Fermi sea and a single electron-hole excitation, consisting of an electron in channel ν at the right and a hole in channel μ at the left.

As a check, we verify that the multi-channel result (4.4) reduces for

$N = 1$ to the single-channel result

$$\left|\Psi_{\text{out}}^{N=1}\right\rangle = |0_{\text{F}}\rangle + \frac{1}{\det(r)} \sum_{\nu,\mu} (t\sigma_2 r^T \sigma_2)_{\nu\mu} b_{R,\nu}^\dagger b_{L,\mu} |0_{\text{F}}\rangle + \mathcal{O}(\epsilon)$$

of Ref. 79. We use the identity [82]

$$\sigma_2 r^T \sigma_2 = \det(r) r^\dagger, \tag{4.6}$$

which holds for any 2×2 unitary matrix r (with σ_2 a Pauli matrix). Hence $t\sigma_2 r^T \sigma_2 = \det(r) t r^\dagger + \mathcal{O}(\epsilon)$. Substitution into the single-channel result (4.6) indeed gives the multi-channel result (4.4) for $N = 1$.

4.2.3 Spin State of the Electron-Hole Pair

The spin state of the electron-hole pair is obtained from $|\Psi_{\text{out}}\rangle$ by projecting out the vacuum contribution and then tracing out the orbital degrees of freedom. This results in the 4×4 density matrix

$$\rho_{\alpha\beta,\gamma\delta} = \frac{1}{w} \sum_{n,m=1}^{N} (tr^\dagger)_{n\alpha,m\beta} (tr^\dagger)^*_{n\gamma,m\delta}, \tag{4.7}$$

with $w = \text{tr}(t^\dagger t r^\dagger r)$. Here n and m label the orbital degrees of freedom and α, β, γ, and δ label the spin degrees of freedom.

We assume that the tunnel resistance is much larger than the resistance of the conductors at the left and right of the tunnel barrier. The transmission eigenvalues T_n (eigenvalues of $tt^\dagger$) are then determined mainly by the tunnel barrier and will depend only weakly on the mode index n. We neglect this dependence entirely, so that $T_n = T$ for all n, the tunneling conductance being given by $G_{\text{tunnel}} = (2e^2/h)NT$.

To obtain a simpler form for the density matrix we use the polar decomposition of the scattering matrix

$$S = \begin{pmatrix} r & t' \\ t & r' \end{pmatrix} = \begin{pmatrix} u & 0 \\ 0 & v \end{pmatrix} \begin{pmatrix} \sqrt{1-\mathcal{T}} & \sqrt{\mathcal{T}} \\ \sqrt{\mathcal{T}} & -\sqrt{1-\mathcal{T}} \end{pmatrix} \begin{pmatrix} u' & 0 \\ 0 & v' \end{pmatrix}, \tag{4.8}$$

where u, u', v, and v' are unitary matrices and $\mathcal{T} = \text{diag}(T_1, T_2, \ldots, T_{2N})$.

For mode independent T_n's the matrix $\mathcal{T}$ equals T times the unit matrix. Hence

$$tr^\dagger = \sqrt{(1-T)T}\,U \tag{4.9}$$

is proportional to the $2N \times 2N$ unitary matrix $U = vu^\dagger$. Substitution into the expression (4.7) for the density matrix gives

$$\rho_{\alpha\beta,\gamma\delta} = \frac{1}{2N} \sum_{n,m=1}^{N} U_{n\alpha,m\beta} U^*_{n\gamma,m\delta}. \tag{4.10}$$

If there is no spin-orbit coupling, the matrix U is diagonal in the spin indices: $U_{n\alpha,m\beta} = \tilde{U}_{nm}\delta_{\alpha\beta}$ with $\tilde{U}$ an $N \times N$ unitary matrix. The density matrix then represents the maximally entangled Bell state $|\psi_{\rm Bell}\rangle$,

$$(\rho_{\rm Bell})_{\alpha\beta,\gamma\delta} = \frac{1}{2}\delta_{\alpha\beta}\delta_{\gamma\delta} = |\psi_{\rm Bell}\rangle \langle\psi_{\rm Bell}|\,, \tag{4.11}$$

$$|\psi_{\rm Bell}\rangle = \frac{1}{\sqrt{2}} \left(|\uparrow\rangle_e |\uparrow\rangle_h + |\downarrow\rangle_e |\downarrow\rangle_h\right), \tag{4.12}$$

with $|\sigma\rangle_{e,h}$ an electron (e) or hole (h) spin pointing up ($\sigma = \uparrow$) or down ($\sigma = \downarrow$). The state (4.11) is a pure state ($\rho^2_{\rm Bell} = \rho_{\rm Bell}$). Spin-orbit coupling will in general degrade ρ to a mixed state, with less entanglement.

4.3 Entanglement of the Electron-Hole Pair

We quantify the degree of entanglement of the mixed electron-hole state (4.7) by means of the concurrence C (which is in one-to-one correspondence with the entanglement of formation and varies from 0 for a nonentangled state to 1 for a maximally entangled state). Following Wootters [80] the concurrence is given by

$$C = \max\left\{0, \sqrt{\lambda_1} - \sqrt{\lambda_2} - \sqrt{\lambda_3} - \sqrt{\lambda_4}\right\}, \tag{4.13}$$

where the λ_i's are the eigenvalues, in decreasing order, of the matrix product $\rho(\sigma_2 \otimes \sigma_2)\rho^*(\sigma_2 \otimes \sigma_2)$.

In the next two subsections we calculate the concurrence numerically for a chaotic cavity using Eq. (4.7) and analytically with an isotropy ap-

proximation for the density matrix.

4.3.1 Numerical Simulation

We calculate the concurrence C numerically for the case that the scattering at the left and at the right of the tunnel barrier is chaotic. (The more experimentally relevant case of diffusive scattering will be considered in the next subsection.)

The total scattering matrix S of the system (shown in Fig. 4.2) is constructed from the scattering matrix of the tunnel barrier,

$$S_T = \begin{pmatrix} \sqrt{1-T}\mathbb{1}_N & \sqrt{T}\mathbb{1}_N \\ \sqrt{T}\mathbb{1}_N & -\sqrt{1-T}\mathbb{1}_N \end{pmatrix}, \tag{4.14}$$

and the scattering matrices S_1 and S_2 of the cavity on each side of the tunnel barrier. (We denote by $\mathbb{1}_N$ the $N \times N$ unit matrix.) We expand S in the small parameter T and keep terms up to order $\mathcal{O}(T^{1/2}) = \mathcal{O}(\epsilon^{1/2})$, consistent with the expansion of the outgoing state (4.4). This results in

$$r = r_1 + t_1' \frac{1}{1-r_1'} t_1 + \mathcal{O}(T), \tag{4.15a}$$

$$t = t_2 \frac{1}{1+r_2} \sqrt{T} \frac{1}{1-r_1'} t_1 + \mathcal{O}(T^{3/2}), \tag{4.15b}$$

and similar expressions for r' and t' which we do not need.

The scattering matrices S_1 and S_2 of the chaotic cavities are constructed from two spin kicked rotators. We briefly explain in Appendix 4.A how we use the results of chapter 2 to make a connection with the work in this chapter.

The resulting ensemble-averaged concurrence as a function of the ratio $\tau_{\rm dwell}/\tau_{\rm so}'$ of the mean dwell time $\tau_{\rm dwell}$ and spin-orbit coupling time $\tau_{\rm so}'$ is shown in Fig. 4.3. The dwell time $\tau_{\rm dwell}$ is the average time between a tunnel event and the escape of the particle into the left or right reservoir. The time $\tau_{\rm so}'$ is the exponential relaxation time of the spin-up and spin-down densities towards the equilibrium distribution[1]. (Both time scales

[1] In chapter 2 we calculate the spin relaxation time for spin amplitudes $\tau_{\rm so} = 2\tau_{\rm so}'$.

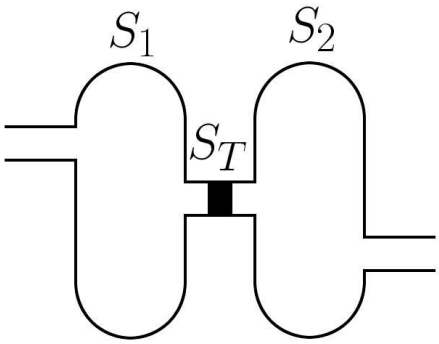

Figure 4.2. Two chaotic cavities with scattering matrices S_1 and S_2 connected by a tunnel barrier with scattering matrix S_T. The chaotic cavities are modeled by two spin kicked rotators.

are calculated in Appendixes 4.A and 4.B.) For a single channel, $N = 1$, the concurrence is unity independent of spin-orbit coupling strength since the trace over the orbital degrees of freedom leaves ρ unchanged. From Fig. 4.3 (bottom panel) we see that for small N the concurrence saturates at a nonzero value for large $\tau_{\rm dwell}/\tau'_{\rm so}$:

$$\lim_{\tau_{\rm dwell}/\tau'_{\rm so}\to\infty}\langle C\rangle = \begin{cases} 1, & N=1, \\ 0.15, & N=2, \\ 0.01, & N=3. \end{cases} \tag{4.16}$$

The limiting value for $N = 2$ is close to that obtained in Ref. 83 in a single chaotic cavity. For $N \gtrsim 5$ the ensemble-averaged concurrence is negligible for large $\tau_{\rm dwell}/\tau'_{\rm so}$. The dependence of $\langle C\rangle$ on $\tau_{\rm dwell}/\tau'_{\rm so}$ becomes N independent for $N \gtrsim 15$.

4.3.2 Isotropy Approximation

To obtain an analytical expression for the entanglement degradation we approximate the density matrix by the spin-isotropic Werner state [81]. The absence of a preferential basis in spin space means that the density

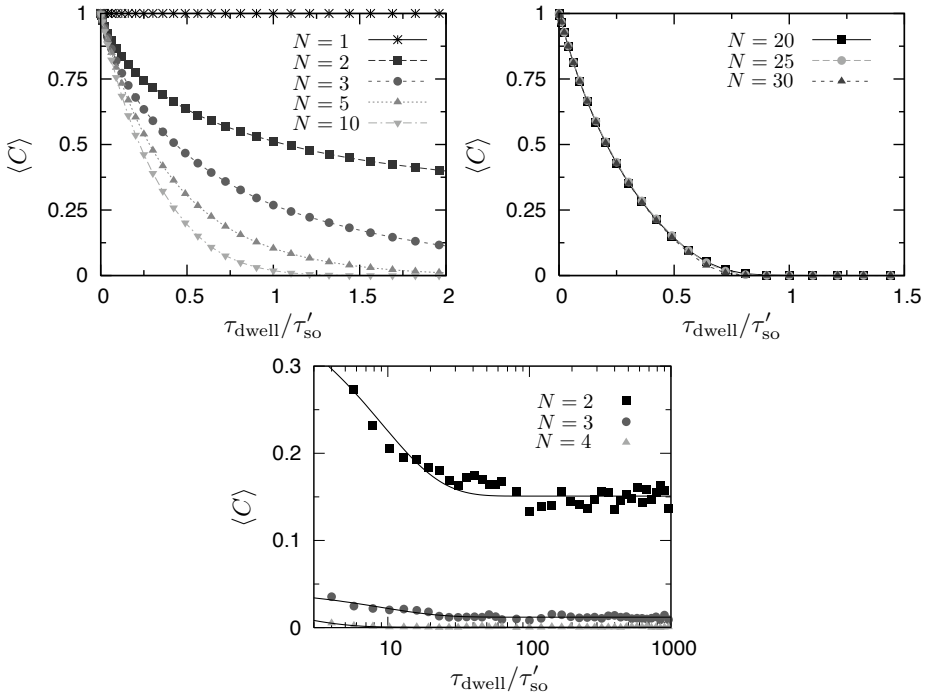

Figure 4.3. Ensemble averaged concurrence of the electron-hole pair scattered by two chaotic cavities, as a function of the spin-orbit coupling rate $1/\tau'_{\rm so}$ for different number of modes, N, in the leads. The data points are calculated from the spin kicked rotator; the lines are guides to the eye. The upper right panel shows that the results become N-independent for large N while the bottom panel shows that for small N the concurrence saturates at a finite value.

matrix ρ for an electron-hole pair is invariant under the transformation

$$(V \otimes V^*)\rho(V^\dagger \otimes V^T) = \rho \tag{4.17}$$

for all 2×2 unitary matrices V. This transformation rotates the spin basis of the electron (acted on by V) and the hole (acted on by V^*) by the same rotation angle. The isotropy relation (4.17) constrains the density matrix to be of the Werner form

$$\rho_{\rm W} = \frac{1}{4}(1-\xi)\mathbb{1}_4 + \xi\,|\psi_{\rm Bell}\rangle\langle\psi_{\rm Bell}|\,, \quad -\frac{1}{3} \le \xi \le 1, \tag{4.18}$$

with $|\psi_{\rm Bell}\rangle$ the Bell state defined in Eq. (4.12). The concurrence of the electron-hole Werner state is given by

$$C(\rho_{\rm W}) = \frac{3}{2}\max\left(0, \xi - \frac{1}{3}\right). \tag{4.19}$$

The parameter ξ characterizing the Werner state can be calculated from

$$\xi = \text{tr}\,[(\sigma_3 \otimes \sigma_3)\rho] = \rho_{11} - \rho_{22} - \rho_{33} + \rho_{44}. \tag{4.20}$$

Only diagonal elements of the density matrix appear in the expression (4.20) for ξ. These can be calculated semiclassically in the N-independent limit $N \gg 1$ (see Appendix 4.B), leading to the following expressions for the concurrence:

$$\langle C\rangle_{\rm diffusive} = \begin{cases} \frac{3}{2}[\sum_{n=0}^{\infty}\xi_n]^2 - \frac{1}{2}, & 1.5\,\tau_{\rm dwell} < \tau'_{\rm so}, \\ 0, & 0 < \tau'_{\rm so} < 1.5\,\tau_{\rm dwell}, \end{cases}$$

$$\xi_n = \frac{4\pi(-1)^n(2n+1)}{\pi^2(2n+1)^2 + 8\tau_{\rm dwell}/\tau'_{\rm so}}, \tag{4.21a}$$

$$\langle C\rangle_{\rm chaotic} = \begin{cases} \frac{3}{2}(1+\tau_{\rm dwell}/\tau'_{\rm so})^{-2} - \frac{1}{2}, & \frac{\tau_{\rm dwell}}{\sqrt{3}-1} < \tau'_{\rm so}, \\ 0, & 0 \le \tau'_{\rm so} \le \frac{\tau_{\rm dwell}}{\sqrt{3}-1}. \end{cases} \tag{4.21b}$$

In Fig. 4.4 we plot the analytical result (4.21) for the concurrence. The two cases of diffusive and chaotic scattering differ only slightly. The initial slopes are the same,

$$\begin{aligned} \langle C\rangle_{\rm diffusive} &= \langle C\rangle_{\rm chaotic} \\ &= 1 - 3\tau_{\rm dwell}/\tau'_{\rm so} + \mathcal{O}(\tau_{\rm dwell}/\tau'_{\rm so})^2. \end{aligned} \tag{4.22}$$

The critical spin-orbit coupling strengths, beyond which the concurrence vanishes, are different: $\tau_{so}^{\rm critical} = 1.5\,\tau_{\rm dwell}$ for diffusive scattering and $\tau_{so}^{\rm critical} = \tau_{\rm dwell}/(\sqrt{3}-1) = 1.37\,\tau_{\rm dwell}$ for chaotic scattering.

We also compare in Fig. 4.4 the analytical results in the chaotic case from this section with the numerical results from the previous section. The agreement is quite good for large N, where the semiclassical analytics is expected to hold.

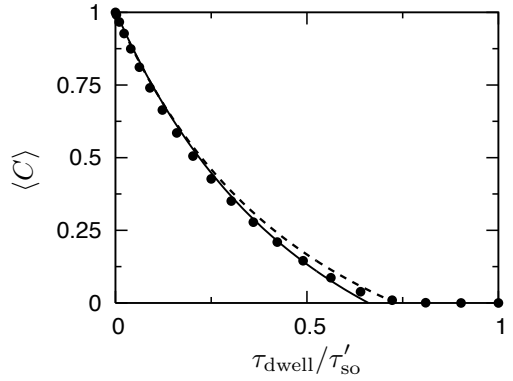

Figure 4.4. Ensemble averaged concurrence as a function of spin-orbit coupling rate $1/\tau'_{\rm so}$. The solid and dashed curves are the analytical results (4.21) in the case of diffusive wires and chaotic cavities, respectively, on each side of the tunnel barrier. These analytical curves use the isotropy approximation. The data points are from the numerical simulation in the chaotic case without the isotropy approximation (spin kicked rotator of Fig. 4.3, with $N = 30$).

4.4 Conclusion

Figure 4.4 summarizes our main findings: The effect of spin-orbit coupling on the degree of spin-entanglement of the electron-hole pairs produced at a tunnel barrier depends strongly on the ratio of the dwell time $\tau_{\rm dwell}$ and spin-orbit coupling time $\tau'_{\rm so}$. Even though $\tau_{\rm dwell}$ and $\tau'_{\rm so}$ each depend sensitively on the nature of the dynamics (diffusive or chaotic) the dependence of the concurrence on the ratio $\tau_{\rm dwell}/\tau'_{\rm so}$ is insensitive to the nature of the dynamics. The initial decay (4.22) is the same and the critical spin-orbit coupling strength (beyond which the entanglement vanishes) differs by less than 10%. This has the useful experimental implication that a single parameter suffices to quantify the amount of entanglement degradation by spin-orbit coupling.

We have tested our analytical theory using a computer simulation for the case of chaotic dynamics. (The close similarity to the diffusive results suggests that this test is representative.) Analytics and numerics are in good agreement, differing by less than 10% in the regime $N \gg 1$ of large conductance G where the semiclassical analytics applies. While the semi-

classical approximation is controlled by the small parameter $1/N$ (or, more generally, h/e^2G), the isotropy approximation has no small parameter that controls the error. Its use is justified by the reasonable expectation that an ensemble of disordered or chaotic systems should have no preferential quantization axis for the electron and hole spins. It is gratifying to see that the numerics supports this expectation.

The standard method of experimentally verifying the presence of entanglement is by demonstrating violation of Bell inequalities. In optics this is achieved by measuring coincidence rates of photons by photodetectors (i.e. by counting photons) in different polarization bases. In the solid state one cannot simply count electrons, but rather needs to formulate the Bell inequalities in terms of correlators of spin currents (= spin noise) [84–86]. This has so far not been accomplished experimentally. Thus, the isotropy approximation that has been used here as a way to simplify the calculation of the concurrence, also has an experimental implication [87]: By relying on spin isotropy the concurrence can be obtained directly from correlators of time averaged spin currents. Our demonstration of the accuracy of the isotropy approximation may motivate experimentalists to try this "poor man's method" of entanglement detection — since average spin currents have been measured [88] while spin noise has not.

Appendix 4.A A Few Words on the Use of the Spin Kicked Rotator

In this chapter we have compared numerical simulations with the spin kicked rotator to analytical calculations. In order to do so, we need to know the time scales $\tau'_{\rm so}$ and $\tau_{\rm dwell}$ in the spin kicked rotator. This was implicit in our comparison with random-matrix theory in section 2.3. In this appendix we give this relation a little more explicitly.

In chapter 2 we considered Eqs. (2.32) and (2.33) as giving the relation between the model parameters of the spin kicked rotator to the physical time scale $\tau_{\rm so} = 2\tau'_{\rm so}$. One can also take these equations to define $\tau_{\rm so}$ for the model. In the spin kicked rotator $\hbar = 1$ and $\Delta = 2\pi/M$. Inserting into Eq. (2.33) and using the expression for K_c from (2.32) we find the spin-orbit coupling time $\tau_{\rm so}$ (in units of the stroboscopic period) in the

model to be determined by the parameter $K_{\rm so}$ through

$$\tau_{\rm so} = 2\tau'_{\rm so} = \frac{32\pi^2}{K_{\rm so}^2 M^2}. \tag{4.23}$$

The mean dwell time $\tau_{\rm dwell}$ (in units of the stroboscopic period) is similarly given by

$$\tau_{\rm dwell} = \frac{M}{N} = \frac{2\pi}{N\Delta}, \tag{4.24}$$

where we have taken into account the fact that N of the $2N$ channels are closed by the tunnel barrier (cf. Fig. 4.2). Notice that the mean dwell time is a classical quantity, while N and Δ separately are quantum mechanical quantities.

We now use the spin kicked rotator to generate two sets scattering matrices (in our simulations we choose $K = 41$ (fully chaotic), $M = 640$, and $l_0 = 0.2$). From the reflection and transmission matrices (4.15) the density matrix (4.7) is obtained, from which the concurrence (4.13) follows. The concurrence is averaged over 20 different quasienergies ε, ε' and over 20 different lead positions P, P' in the two cavities (assumed to be independent scatterers). Results are shown in Fig. 4.3.

Appendix 4.B Calculation of Spin Correlators

The diagonal elements of the density matrix appearing in the expression (4.20) for the Werner parameter ξ represent spin correlators,

$$\rho_{11} = P_{\uparrow\uparrow},\ \rho_{22} = P_{\uparrow\downarrow},\ \rho_{33} = P_{\downarrow\uparrow},\ \rho_{44} = P_{\downarrow\downarrow}. \tag{4.25}$$

Here $P_{\sigma\sigma'}$ is the probability that the outgoing electron has spin σ and the outgoing hole has spin σ'. To calculate these correlators, it is convenient to first consider only those electrons that exit after a time t and those holes that exit after a time t'. The time-resolved correlator $P_{\sigma\sigma'}(t,t')$ gives the desired $P_{\sigma\sigma'}$ after integration over time,

$$P_{\sigma\sigma'} = \int_0^\infty dt \int_0^\infty dt' P_{\sigma\sigma'}(t,t') P_{\rm dwell}(t) P_{\rm dwell}(t'), \tag{4.26}$$

weighted by the dwell time distribution $P_{\rm dwell}$ (we assume that the dwell times at the left and right of the tunnel barrier are independent and identically distributed).

As initial condition we take

$$P_{\sigma\sigma'}(0,0) = \frac{1}{2}\delta_{\sigma\sigma'}, \tag{4.27}$$

corresponding to the spin state immediately after the tunnel event. Spin-orbit coupling randomizes the spin with a rate $1/\tau'_{\rm so}$, so that $P_{\sigma\sigma'}(t,t')$ decreases in time according to the rate equations

$$\frac{d}{dt}P_{\sigma\sigma'}(t,t') = \frac{1}{2\tau'_{\rm so}}\sum_{\sigma''}[P_{\sigma''\sigma'}(t,t') - P_{\sigma\sigma'}(t,t')], \tag{4.28a}$$

$$\frac{d}{dt'}P_{\sigma\sigma'}(t,t') = \frac{1}{2\tau'_{\rm so}}\sum_{\sigma''}[P_{\sigma\sigma''}(t,t') - P_{\sigma\sigma'}(t,t')]. \tag{4.28b}$$

The solution of the rate equations (4.28) with the initial condition (4.27) is

$$P_{\uparrow\uparrow}(t,t') = P_{\downarrow\downarrow}(t,t') = \frac{1}{4} + \frac{1}{4}e^{-(t+t')/\tau'_{\rm so}}, \tag{4.29a}$$

$$P_{\uparrow\downarrow}(t,t') = P_{\downarrow\uparrow}(t,t') = \frac{1}{4} - \frac{1}{4}e^{-(t+t')/\tau'_{\rm so}}. \tag{4.29b}$$

To complete the calculation we need the dwell time distribution. For a chaotic cavity this has the well known exponential form [89]

$$P_{\rm dwell,chaotic} = \frac{1}{\tau_{\rm dwell}}e^{-t/\tau_{\rm dwell}}, \tag{4.30}$$

with

$$\tau_{\rm dwell} = \frac{2\pi\hbar}{N\Delta} \tag{4.31}$$

inversely proportional to the mean level spacing Δ of Kramers degenerate levels in the cavity.

For the diffusive wire (diffusion constant D) we determine $P_{\rm dwell}$ by

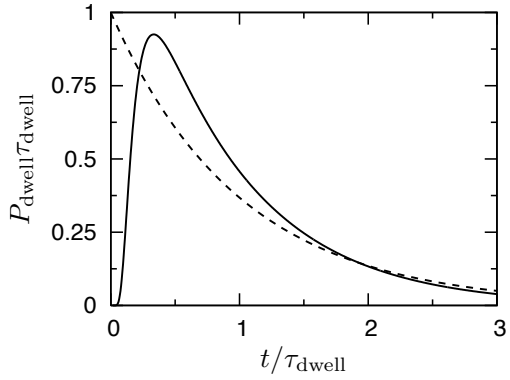

Figure 4.5. Dwell time distribution in a diffusive wire (solid line) and chaotic cavity (dashed line).

solving the one-dimensional diffusion equation

$$\left(\frac{\partial}{\partial t} - D\frac{\partial^2}{\partial x^2}\right) p(x,t) = 0, \quad 0 < x < L, \tag{4.32}$$

with initial and boundary conditions

$$\frac{\partial p}{\partial x}(0,t) = 0, \quad p(L,t) = 0, \quad p(x,0) = \delta(x). \tag{4.33}$$

Here $p(x,t)$ is the classical probability of finding a particle at point x at time t. The boundary conditions represent reflection by the high tunnel barrier at $x = 0$ and absorption by the reservoir at $x = L$.

The probability that the particle is still in the wire at time t is given by

$$N(t) = \int_0^L p(x,t)dx, \tag{4.34}$$

and therefore the dwell time distribution is

$$P_{\rm dwell} = -\frac{dN(t)}{dt}. \tag{4.35}$$

Solution of the diffusion equation by expansion in eigenstates gives the

result in the form

$$P_{\text{dwell, diffusive}} = \frac{\pi}{2\tau_{\text{dwell}}} \sum_{n=0}^{\infty} (-1)^n (2n+1) e^{-(2n+1)^2 \frac{\pi^2}{8} \frac{t}{\tau_{\text{dwell}}}}. \tag{4.36}$$

The mean dwell time is

$$\tau_{\text{dwell}} = \frac{L^2}{2D}. \tag{4.37}$$

The dwell time distributions for the chaotic and diffusive dynamics are compared in Fig. 4.5.

Collecting results we arrive at the expressions (4.21) for the concurrence given in the main text.

Chapter 5

Mesoscopic Spin Hall Effect

5.1 Introduction

The novel and rapidly expanding field of spintronics is interested in the creation, manipulation, and detection of polarized or pure spin currents [90]. The conventional methods of doing spintronics are to use magnetic fields and/or ferromagnets as parts of the creation-manipulation-detection cycle, and to use the Zeeman coupling and the ferromagnetic-exchange interactions to induce the spin dependency of transport. More recently, ways to generate spin accumulations and spin currents based on the coupling of spin and orbital degrees of freedom have been explored. Among these proposals, much attention has been focused on the spin Hall effect (SHE), where pure spin currents are generated by applied electric currents on spin-orbit (SO) coupled systems. Originally proposed by Dyakonov and Perel [29, 91], the idea was resurrected by Hirsch [30] and extended to crystal SO field (the intrinsic SHE) by Sinova *et al.* [31] and Murakami [92]. The current agreement is that the SHE vanishes for bulk, k-linear SO coupling for diffusive two-dimensional electrons [32, 93, 94]. This result is however specific to these systems [95], and the SHE does not vanish for impurity-generated SO coupling, two-dimensional hole systems with either Rashba or Dresselhaus SO coupling, and for finite-sized electronic systems [93, 95]. These predictions have been, to some extent, confirmed by experimental observations of edge spin accumulations in electron [96, 97] and hole [98] systems, and electrical detection of spin currents via ferro-

magnetic leads [99–101].

Most investigations of the SHE to date focused on disordered conductors with spin-orbit interaction, where the disorder-averaged spin Hall conductivity was calculated using either the Kubo formalism or a diffusion equation approach [30, 31, 94, 102, 32, 93, 103, 92, 95]. Few numerical works alternatively used the scattering approach to transport [104] to calculate the average spin Hall conductance of explicitly finite-sized samples connected to external electrodes. These investigations were however restricted to tight-binding Hamiltonians with no or weak disorder in simple geometries [105–107]. The data of Ref. 108 in particular suggest that diffusive samples with large enough SO coupling exhibit universal fluctuations of the spin Hall conductance $G_{\rm sH}$ with $\mathrm{rms}[G_{\rm sH}] \approx 0.18e/4\pi$. These numerical investigations call for an analytical theory of the SHE in mesoscopic systems, which we provide here.

We analytically investigate the DC spin Hall effect in mesoscopic cavities with SO coupling. We calculate both the ensemble-average and the fluctuations of the transverse spin current generated by a longitudinal charge current. Our approach is based on random matrix theory (RMT) [60], and is valid for ballistic chaotic and mesoscopic diffusive systems at low temperature, in the limit when the spin-orbit coupling time is much shorter than the mean dwell time of the electrons in the cavity, $\tau_{\rm so} \ll \tau_{\rm dwell}$. We show that while the transverse spin current is generically nonzero for a typical sample, its sign and amplitude fluctuate universally, from sample to sample or upon variation of the chemical potential with a vanishing average. We find that for a typical ballistic chaotic quantum dot, the transverse spin current corresponds to slightly less than one excess open channel for one of the two spin species. These analytical results are confirmed by numerical simulations for a stroboscopic model of a ballistic chaotic cavity.

In the ballistic regime, contributions to the SO coupling arise from the crystal field and confinement potentials. In analogy with diffusive systems, the SHE originating from the crystal field as well as the asymmetry of the confinement potential in the out of plane direction (i.e. the Rashba term) can be thought of as the intrinsic effect, while in plane confinement potentials generate extrinsic contributions to the SHE. Although the bal-

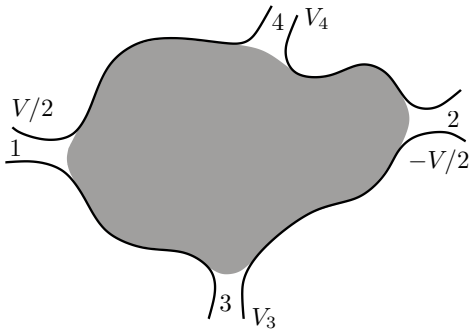

Figure 5.1. Ballistic quantum dot connected to four electrodes. The longitudinal bias V induces a charge current through terminals 1 and 2, while the voltages $V_{3,4}$ are adjusted such that no charge current flows through the transverse leads 3 and 4. Spin-orbit coupling is active only in the gray region.

ance between the two effects modifies nonuniversal properties such as the spin-orbit time, it does not affect the universal features described in this Letter.

5.2 Scattering Approach

We consider a ballistic chaotic quantum dot coupled to four external electrodes via ideal point contacts, each with N_i open channels ($i = 1, \ldots 4$). The geometry is sketched in Fig. 5.1. Spin-orbit coupling exists only inside the dot, and the electrochemical potentials in the electrodes are spin-independent. A bias voltage V is applied between the longitudinal electrodes labeled 1 and 2. The voltages V_3 and V_4 are set such that no net charge current flows through the transverse electrodes 3 and 4. We will focus on the magnitude of the spin current through electrodes 3 and 4, in the limit when the openings to the electrodes are small enough, and the spin-orbit coupling strong enough that $\tau_{\rm so} \ll \tau_{\rm dwell}$.

We write the spin-resolved current through the i-th electrode as [104]

$$I_i^\sigma = \frac{e^2}{h} \sum_{j,\sigma'} T_{ij}^{\sigma,\sigma'} (V_i - V_j). \tag{5.1}$$

The spin-dependent transmission coefficients are obtained by summing over electrode channels

$$T_{i,j}^{\sigma,\sigma'} = \sum_{m\in i}\sum_{n\in j}|t_{m,\sigma;n,\sigma'}|^2, \tag{5.2}$$

i.e. $t_{m,\sigma;n,\sigma'}$ is the transmission amplitude for an electron initially in a spin state σ' in channel n of electrode j to a spin state σ in channel m of electrode i. The transmission amplitudes t are the elements of the $2N_T \times 2N_T$ scattering matrix S, with $N_T = \sum_{i=1}^{4} N_i$.

We are interested in the transverse spin currents $I_i^{(z)} = I_i^{\uparrow} - I_i^{\downarrow}$, $i = 3, 4$, under the two constraints that (i) charge current vanishes in the transverse leads, $I_i^{\uparrow} + I_i^{\downarrow} = 0$, $i = 3, 4$ and (ii) the charge current is conserved, $I_1 = -I_2 = I$. From Eq. (5.1), transport through the system is then described by the following equation

$$\begin{pmatrix} 2J \\ J_3^{(z)} \\ J_4^{(z)} \end{pmatrix} = \mathcal{G} \begin{pmatrix} 1/2 \\ \tilde{V}_3 \\ \tilde{V}_4 \end{pmatrix}, \tag{5.3}$$

where

$$\mathcal{G} = \begin{pmatrix} 2N_1 - \mathcal{T}_{11}^{(0)} + 2N_2 - \mathcal{T}_{22}^{(0)} + \mathcal{T}_{12}^{(0)} + \mathcal{T}_{21}^{(0)} & \mathcal{T}_{23}^{(0)} - \mathcal{T}_{13}^{(0)} & \mathcal{T}_{24}^{(0)} - \mathcal{T}_{14}^{(0)} \\ \mathcal{T}_{32}^{(z)} - \mathcal{T}_{31}^{(z)} & -\mathcal{T}_{33}^{(z)} & -\mathcal{T}_{34}^{(z)} \\ \mathcal{T}_{42}^{(z)} - \mathcal{T}_{41}^{(z)} & -\mathcal{T}_{43}^{(z)} & -\mathcal{T}_{44}^{(z)} \end{pmatrix} \tag{5.4}$$

and the transverse voltages (in units of V) read

$$\tilde{V}_3 = \frac{1}{2}\frac{\mathcal{T}_{34}^{(0)}(\mathcal{T}_{42}^{(0)} - \mathcal{T}_{41}^{(0)}) + (2N_4 - \mathcal{T}_{44}^{(0)})(\mathcal{T}_{32}^{(0)} - \mathcal{T}_{31}^{(0)})}{\mathcal{T}_{34}^{(0)}\mathcal{T}_{43}^{(0)} - (2N_3 - \mathcal{T}_{33}^{(0)})(2N_4 - \mathcal{T}_{34}^{(0)})}, \tag{5.5a}$$

$$\tilde{V}_4 = \frac{1}{2}\frac{\mathcal{T}_{43}^{(0)}(\mathcal{T}_{32}^{(0)} - \mathcal{T}_{31}^{(0)}) + (2N_3 - \mathcal{T}_{33}^{(0)})(\mathcal{T}_{42}^{(0)} - \mathcal{T}_{41}^{(0)})}{\mathcal{T}_{34}^{(0)}\mathcal{T}_{43}^{(0)} - (2N_3 - \mathcal{T}_{33}^{(0)})(2N_4 - \mathcal{T}_{34}^{(0)})}, \tag{5.5b}$$

and we defined the dimensionless currents $I = e^2VJ/h$. We introduced

generalized transmission probabilities

$$\mathcal{T}_{ij}^{(\mu)} = \sum_{m\in i, n\in j} \mathrm{Tr}[(t_{mn})^\dagger \sigma^{(\mu)} t_{mn}], \quad \mu = 0, x, y, z, \tag{5.6}$$

where $\sigma^{(\mu)}$ are Pauli matrices ($\sigma^{(0)}$ is the identity matrix) and one traces over the spin degree of freedom.

5.3 Random Matrix Theory

We calculate the average and fluctuations of the transverse spin currents $J_i^{(\mu)}$, $\mu = x, y, z$ within the framework of RMT. Accordingly, we replace the scattering matrix S by a random unitary matrix, which, in our case of a system with time reversal symmetry (absence of magnetic field) and totally broken spin rotational symmetry (strong spin-orbit coupling), has to be taken from the circular symplectic ensemble[1] (CSE) [60, 41]. We rewrite the generalized transmission probabilities $\mathcal{T}_{ij}^{(\mu)}$ as a trace over S

$$\mathcal{T}_{ij}^{(\mu)} = \mathrm{Tr}\,[Q_i^{(\mu)} S Q_j^{(0)} S^\dagger], \tag{5.7}$$

$$[Q_i^{(\mu)}]_{m\alpha,n\beta} = \begin{cases} \delta_{mn}\, \sigma_{\alpha\beta}^{(\mu)}, & \sum_{j=1}^{i-1} N_j < m \le \sum_{j=1}^{i} N_j, \\ 0, & \text{otherwise.} \end{cases}$$

Here, m and n are channel indices, while α and β are spin indices. The trace is taken over both set of indices.

Averages, variances, and covariances of the generalized transmission probabilities (5.7) over the CSE can be calculated using the method of Ref. 17. For the average transmission probabilities, we find

$$\langle \mathcal{T}_{ij}^{(\mu)} \rangle = \frac{2\delta_{\mu 0}}{N_T - 1/2} \left(N_i N_j - \frac{1}{2} N_i \delta_{ij} \right), \tag{5.8}$$

[1] We assume that the SO coupling parameters are sufficiently nonuniform, so that SO cannot be removed from the Hamiltonian by a gauge transformation, see Ref. 41.

while variances and covariances are given by

$$\begin{aligned}
&\langle \delta\mathcal{T}_{ij}^{(\mu)} \delta\mathcal{T}_{kl}^{(\nu)} \rangle = \\
&\frac{4\delta_{\mu\nu}}{N_T(2N_T-1)^2(2N_T-3)} \Big\{ N_i N_j (N_T-1)(2N_T-1)(\delta_{ik}\delta_{jl} + \delta_{il}\delta_{jk}\delta_{\mu 0}) \\
&+ (N_i N_k \delta_{ij}\delta_{kl} - 2N_i N_k N_l \delta_{ij} - 2N_i N_j N_k \delta_{kl} + 4N_i N_j N_k N_l)\delta_{\mu 0} \\
&- N_i N_T (2N_T-1)\delta_{ijkl} + (2N_T-1)\Big[N_i N_l \delta_{ijk} + N_i N_k \delta_{ijl}\delta_{\mu 0} \\
&+ N_i N_j (\delta_{ikl} + \delta_{jkl}\delta_{\mu 0}) - N_i N_j N_l (\delta_{ik} + \delta_{jk}\delta_{\mu 0}) - N_i N_j N_k \delta_{\mu 0}(\delta_{il} + \delta_{jl}) \Big] \Big\},
\end{aligned} \tag{5.9}$$

where $\delta\mathcal{T}_{ij}^{(\mu)} = \mathcal{T}_{ij}^{(\mu)} - \langle \mathcal{T}_{ij}^{(\mu)} \rangle$.

Because the transverse potentials $\tilde{V}_{3,4}$ are spin-independent, they are not correlated with $\mathcal{T}_{ij}^{(\mu)}$. Additionally taking Eq. (5.8) into account, one concludes that the average transverse spin current vanishes ($i = 3, 4$),

$$\langle J_i^{(\mu)} \rangle = \frac{1}{2}\langle \mathcal{T}_{i2}^{(\mu)} - \mathcal{T}_{i1}^{(\mu)} \rangle - \sum_{j=3,4} \langle \mathcal{T}_{ij}^{(\mu)} \rangle \langle \tilde{V}_j \rangle = 0. \tag{5.10}$$

However, for a given sample at a fixed chemical potential $J_i^{(\mu)}$ will in general be finite. We thus calculate var $[J_i^{(\mu)}]$. We first note that $\langle \tilde{V}_{3,4} \rangle = (N_1 - N_2)/2(N_1 + N_2)$, and that var $[\tilde{V}_{3,4}]$ vanishes to leading order in the inverse number of channels. One thus has

$$\begin{aligned}
\text{var}\,[J_i^{(\mu)}] &= \frac{1}{4}\sum_{j=1,2} \text{var}[\mathcal{T}_{ij}^{(\mu)}] - \frac{1}{2}\,\text{covar}[\mathcal{T}_{i1}^{(\mu)}, \mathcal{T}_{i2}^{(\mu)}] \\
&+ \sum_{j=3,4} \Big\{ \text{var}[\mathcal{T}_{ij}^{(\mu)}] \langle \tilde{V}_j \rangle^2 + \text{covar}[\mathcal{T}_{i1}^{(\mu)} - \mathcal{T}_{i2}^{(\mu)}, \mathcal{T}_{ij}^{(\mu)}] \langle \tilde{V}_j \rangle \Big\} \\
&+ 2\,\text{covar}[\mathcal{T}_{i3}^{(\mu)}, \mathcal{T}_{i4}^{(\mu)}] \langle \tilde{V}_3 \rangle \langle \tilde{V}_4 \rangle.
\end{aligned} \tag{5.11}$$

From Eqs. (5.9) and (5.11) it follows that

$$\text{var}\,[J_i^{(\mu)}] = \frac{4N_i N_1 N_2 (N_T - 1)}{N_T(2N_T-1)(2N_T-3)(N_1+N_2)}. \tag{5.12}$$

Eqs. (5.10) and (5.12) are our main results. They show that, while the average transverse spin current vanishes, it exhibits universal sample-to-

sample fluctuations. The origin of this universality is the same as for charge transport [60], and relies on the fact expressed in Eq. (5.9) that to leading order, spin-dependent transmission correlators do not scale with the number of channels. The spin current carried by a single typical sample is given by $\mathrm{rms}[J_i^{(\mu)}] \times e^2V/h$, and is thus of order e^2V/h in the limit of large number of channels. In other words, for a given sample, one spin species has of order one more open transport channel than the other one. For a fully symmetric configuration, $N_i \equiv N$, the spin current fluctuates universally for large N, with $\mathrm{rms}[I_3^z] \simeq (e^2V/h)/\sqrt{32}$. This translates into universal fluctuations of the transverse spin conductance with $\mathrm{rms}[G_{\mathrm{sH}}] = (e/4\pi\sqrt{32}) \approx 0.18(e/4\pi)$ in agreement with Ref. 108.

5.4 Numerical Simulation

In the setup of Ref. 108 the universal regime is not very large and thus it is difficult to unambiguously identify it. Moreover, in the same setup all four sides of a square lattice are completely connected to the external leads (see inset to Fig. 1 in Ref. 108). Because of this geometry, there are paths connecting longitudinal to transverse leads that are much shorter than the elastic mean free path. It is well known that such paths contribute nonuniversally to the average conductance. We therefore present numerical simulations in chaotic cavities to further illustrate our analytical predictions (5.10) and (5.12).

We model the electronic dynamics inside a chaotic ballistic cavity by the spin kicked rotator of chapter 2. Averages were performed over 35 values of K in the range $41 < K < 48$, 25 values of ε uniformly distributed in $0 < \varepsilon < 2\pi$, and 10 different lead positions $l^{(k)}$. We set the strength of K_{so} such that $\tau_{\mathrm{so}} = \tau_{\mathrm{dwell}}/1250$, and fixed values of $M = 640$ and $l_0 = 0.2$.

Our numerical results are presented in Fig. 5.2. Two cases were considered, the longitudinally symmetric ($N_1 = N_2$) and asymmetric ($N_1 \neq N_2$) configurations. In both cases, the numerical data fully confirm our predictions that the average spin current vanishes and that the variance of the transverse spin current is universal, i.e. it does not depend on N for large enough value of N. In the asymmetric case $N_4 = 2N_3$, the variance of the spin current in lead 4 is twice as big as in lead 3, giving further

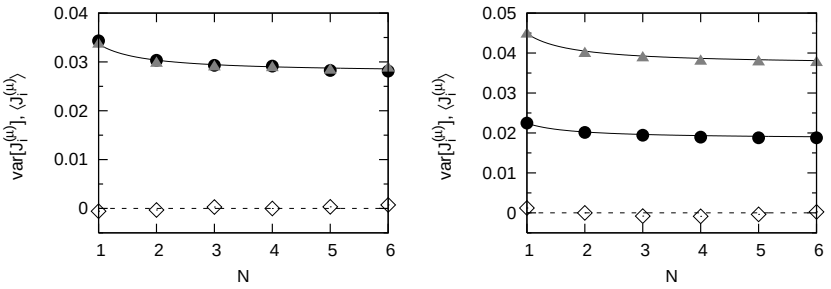

Figure 5.2. Average and variance of the transverse spin current vs. the number of modes. Left panel: longitudinally symmetric configuration with $N_1 = N_2 = 2N_3 = 2N_4 = 2N$; right panel: longitudinally asymmetric configuration with $N_2 = N_4 = 2N_1 = 2N_3 = 2N$. In both cases the total number of modes $N_T = 6N$. The solid (dashed) lines give the analytical prediction (5.10) [(5.12)] for the mean (variance) of the spin currents. Empty diamonds correspond to $\langle J_i^{(\mu)} \rangle$, circles to var $[J_3^{(\mu)}]$ and triangles to var $[J_4^{(\mu)}]$.

confirmation to Eq. (5.12).

5.5 Conclusion

We have calculated the average and mesoscopic fluctuations of the transverse spin current generated by a charge current through a chaotic quantum dot with SO coupling. We find that, from sample to sample, the spin current fluctuates universally around zero average. In particular, for a fully symmetric configuration $N_i \equiv N$, this translates into universal fluctuations of the spin conductance with rms$[G_{\rm sH}] = (e/4\pi\sqrt{32}) \approx 0.18(e/4\pi)$. This universal value is in agreement with the universality observed in the recent simulations in the diffusive regime [108].

Chapter 6

One-Parameter Scaling at the Dirac Point in Graphene

6.1 Introduction

Graphene provides a new regime for two-dimensional quantum transport [23–25], governed by the absence of backscattering of Dirac fermions [22]. A counterintuitive consequence is that adding disorder to a sheet of undoped graphene initially *increases* its conductivity [38, 109]. Intervalley scattering at stronger disorder strengths enables backscattering [110], eventually leading to localization and to a vanishing conductivity in the thermodynamic limit [36, 37]. Intervalley scattering becomes less and less important if the disorder is more and more smooth on the scale of the lattice constant a. The fundamental question of the new quantum transport regime is how the conductivity σ scales with increasing system size L if intervalley scattering is suppressed.

In usual disordered electronic systems, the hypothesis of *one-parameter scaling* plays a central role in our conceptual understanding of the metal-insulator transition [34, 111]. According to this hypothesis, the logarithmic derivative $d\ln\sigma/d\ln L = \beta(\sigma)$ is a function only of σ itself[1] — irrespective

[1] We define the β-function in terms of the ensemble averaged conductivity σ, measured in units of $4e^2/h$ (with the factor of four accounting for twofold spin and valley degeneracies). This is the appropriate definition for our system. For a more general definition of one-parameter scaling, one needs to scale a distribution function of con-

of the sample size or degree of disorder. A positive β-function means that the system scales towards a metal with increasing system size, while a negative β-function means that it scales towards an insulator. The metal-insulator transition is at $\beta = 0$, $\beta' > 0$. In a two-dimensional system with symplectic symmetry, such as graphene, one would expect a monotonically increasing β-function with a metal-insulator transition at [112] $\sigma_S \approx 1.4$ (see Fig. 6.1, green dashed curve).

Recent papers have argued that graphene might deviate in an interesting way from this simple expectation. Nomura and MacDonald [113] have emphasized that the very existence of a β-function in undoped graphene is not obvious, in view of the diverging Fermi wave length at the Dirac point. Assuming that one-parameter scaling does hold, Ostrovsky, Gornyi, and Mirlin [39] have proposed the scaling flow of Fig. 6.1 (black solid curve). Their β-function implies that σ approaches a universal, scale invariant value σ^* in the large-L limit, being the hypothetical quantum critical point of a certain field theory. This field theory differs from the symplectic sigma model by a topological term [39, 40]. The quantum critical point could not be derived from the weak-coupling theory of Ref. 39, but its existence was rather concluded from the analogy to the effect of a topological term in the field theory of the quantum Hall effect [111, 114]. The precise value of σ^* is therefore unknown, but it is well constrained [39]: From below by the ballistic limit[2] $\sigma_0 = 1/\pi$ [115, 116] and from above by the unstable fixed point $\sigma_S \approx 1.4$.

In this chapter we present a numerical test firstly, of the existence of one-parameter scaling, and secondly of the scaling prediction of Ref. 39 against an alternative scaling flow, a positive β without a fixed point (green dotted curve in Fig. 6.1). For such a test it is crucial to avoid the finite-a effects of intervalley scattering that might drive the system to an insulator before it can reach the predicted scale invariant regime. We accomplish this by starting from the Dirac equation, being the $a \to 0$ limit of the tight-binding model on a honeycomb lattice. We have developed an effi-

ductances [111].

[2] We call σ_0 the ballistic limit because it is reached in the absence of disorder, but we emphasize that it is a conductivity — not a conductance. This is a unique property (called "pseudodiffusive") of graphene at the Dirac point, that its conductance scales $\propto 1/L$ like in a diffusive system even in the absence of disorder.

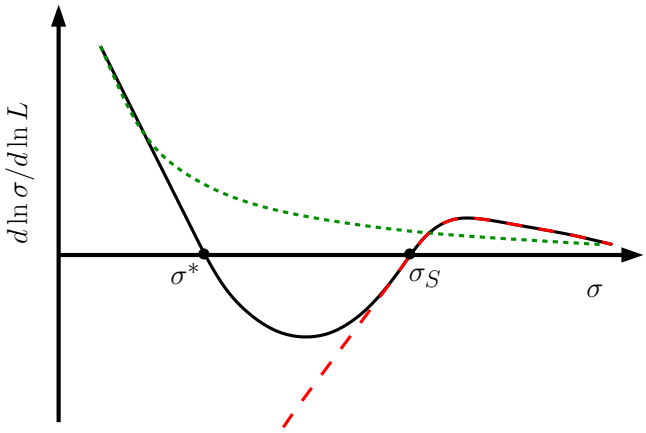

Figure 6.1. Two scenarios for the scaling of the conductivity σ with sample size L at the Dirac point in the absence of intervalley scattering. The black solid curve with two fixed points is proposed in Ref. 39, the green dotted curve without a fixed point is an alternative scaling supported by the numerical data presented in this chapter. For comparison, we include as a red dashed curve the scaling flow in the symplectic symmetry class, which has a metal-insulator transition at $\sigma_S \approx 1.4$ [112].

cient transfer operator method to solve this equation, which we describe in Sec. 6.2 before proceeding to the results in Sec. 6.3.

6.2 Transfer Matrix Approach

The single-valley Dirac Hamiltonian reads

$$H = v\mathbf{p}\cdot\boldsymbol{\sigma} + V(x) + U(x,y). \tag{6.1}$$

The vector of Pauli matrices $\boldsymbol{\sigma}$ acts on the sublattice index of the spinor Ψ, $\boldsymbol{p} = -i\hbar\partial/\partial\boldsymbol{r}$ is the momentum operator, and v is the velocity of the massless excitations. The disorder potential $U(\boldsymbol{r})$ varies randomly in the strip $0 < x < L$, $0 < y < W$ (with zero average, $\langle U\rangle = 0$). This disordered strip is connected to highly doped ballistic leads, according to the doping profile $V(x) = 0$ for $0 < x < L$, $V(x) \to -\infty$ for $x < 0$ and $x > L$. We set the Fermi energy at zero (the Dirac point), so that the disordered strip is

undoped. The disorder strength is quantified by the correlator

$$K_0 = \frac{1}{(\hbar v)^2} \int d\boldsymbol{r}' \, \langle U(\boldsymbol{r}) U(\boldsymbol{r}') \rangle. \tag{6.2}$$

Following Refs. 38 and 117, we work with a transfer operator representation of the Dirac equation $H\Psi = 0$ at zero energy. We discretize x at the N points $x_1, x_2, \ldots x_N$ and represent the impurity potential by $U(\boldsymbol{r}) = \sum_n U_n(y)\delta(x - x_n)$. Upon multiplication by $i\sigma_x$ the Dirac equation in the interval $0 < x < L$ takes the form

$$\hbar v \frac{\partial}{\partial x} \Psi_x(y) = \left[v p_y \sigma_z - i\sigma_x \sum_n U_n(y)\delta(x - x_n) \right] \Psi_x(y). \tag{6.3}$$

The transfer operator $\mathcal{M}$, defined by $\Psi_L = \mathcal{M}\Psi_0$, is given by the operator product

$$\mathcal{M} = \mathcal{P}_{L,x_N} \mathcal{K}_N \mathcal{P}_{x_N,x_{N-1}} \cdots \mathcal{K}_2 \mathcal{P}_{x_2,x_1} \mathcal{K}_1 \mathcal{P}_{x_1,0}, \tag{6.4}$$

$$\mathcal{P}_{x,x'} = \exp[(1/\hbar)(x - x')p_y \sigma_z], \tag{6.5}$$

$$\mathcal{K}_n = \exp[-(i/\hbar v) U_n \sigma_x]. \tag{6.6}$$

The operator $\mathcal{P}$ gives the decay of evanescent waves between two scattering events, described by the operators $\mathcal{K}_n$. For later use we note the current conservation relation

$$\mathcal{M}^{-1} = \sigma_x \mathcal{M}^\dagger \sigma_x. \tag{6.7}$$

We assume periodic boundary conditions in the y-direction, so that we can represent the operators in the basis

$$\psi_k^\pm = \frac{1}{\sqrt{W}} e^{iq_k y} |\pm\rangle, \quad q_k = \frac{2\pi k}{W}, \quad k = 0, \pm 1, \pm 2 \ldots. \tag{6.8}$$

The spinors $|+\rangle = 2^{-1/2}\binom{1}{1}$, $|-\rangle = 2^{-1/2}\binom{1}{-1}$ are eigenvectors of σ_x. In this basis, $(p_y)_{kk'} = \hbar q_k \delta_{kk'}$ is a diagonal operator, while $(U_n)_{kk'} = W^{-1} \int dy \, U_n(y) \times \exp[i(q_{k'} - q_k)y]$ is nondiagonal. We work with finite-dimensional transfer matrices by truncating the transverse momenta q_k at $|k| = M$.

The transmission and reflection matrices t, r are determined as in

Ref. 116, by matching the amplitudes of incoming, reflected, and transmitted modes in the heavily doped graphene leads to states in the undoped strip at $x = 0$ and $x = L$. This leads to the set of linear equations

$$\sum_k \left[\delta_{kk'}\psi_k^+(y) + r_{kk'}\psi_k^-(y)\right] = \Psi_0(y), \tag{6.9a}$$

$$\sum_k t_{kk'}\psi_k^+(y) = \Psi_L(y) = \mathcal{M}\Psi_0(y). \tag{6.9b}$$

Using the current conservation relation (6.7) we can solve Eq. (6.9) for the transmission matrix,

$$\begin{pmatrix} 1-r \\ 1+r \end{pmatrix} = \mathcal{M}^\dagger \begin{pmatrix} t \\ t \end{pmatrix} \Rightarrow t^{-1} = \langle +|\mathcal{M}^\dagger|+\rangle. \tag{6.10}$$

The transmission matrix determines the conductance $G = (4e^2/h)\,\mathrm{Tr}\,tt^\dagger$, and hence the dimensionless conductivity $\sigma = (h/4e^2)(L/W)G$. The average conductivity $\langle\sigma\rangle$ is obtained by sampling some $10^2 - 10^3$ realizations of the impurity potential.

Because the transfer matrix $\mathcal{P}$ has both exponentially small and exponentially large eigenvalues, the matrix multiplication (6.4) is numerically unstable. As in Ref. 118, we stabilize the product of transfer matrices by transforming it into a composition of unitary scattering matrices, involving only eigenvalues of unit absolute value.

We model the disorder potential $U(\boldsymbol{r}) = \sum_{n=1}^N \gamma_n \delta(x - x_n)\delta(y - y_n)$ by a collection of N isolated impurities distributed uniformly over a strip $0 < x < L$, $0 < y < W$. (An alternative model of a continuous Gaussian random potential is discussed at the end of the chapter.) The strengths γ_n of the scatterers are uniform in the interval $[-\gamma_0, \gamma_0]$. The number N sets the average separation $d = (WL/N)^{1/2}$ of the scatterers. The cut-off $|k| \le M$ imposed on the transverse momenta q_k limits the spatial resolution $\xi \equiv W/(2M+1)$ of plane waves $\propto e^{iq_k y \pm q_k x}$ at the Dirac point. The resulting finite correlation lengths of the scattering potential in the x- and y-directions scale with ξ, but they are not determined more precisely. The disorder strength (6.2) evaluates to $K_0 = \frac{1}{3}\gamma_0^2(\hbar v d)^{-2}$, independent of the correlation lengths. We scale towards an infinite system by increasing

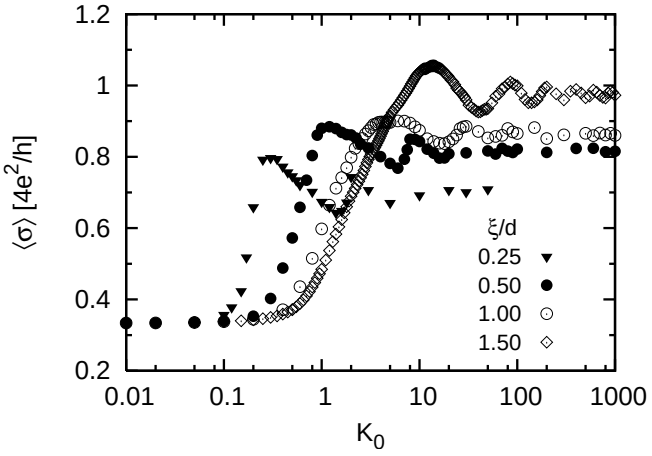

Figure 6.2. Disorder strength dependence of the average conductivity for a fixed system size ($W = 4\,L = 40\,d$) and four values of the scattering range.

$M \propto L$ at fixed disorder strength K_0, scattering range ξ/d, and aspect ratio W/L. This completes the description of our numerical method.

6.3 Numerical Results

We now turn to the results. In Fig. 6.2 we first show the dependence of the average conductivity on K_0 for a fixed system size. As in the tight-binding model of Ref. 109, disorder increases the conductivity above the ballistic value. This impurity assisted tunneling [38] saturates in an oscillatory fashion for $K_0 \gg 1$ (unitary limit [119, 120]). In the tight-binding model [109] the initial increase of σ was followed by a rapid decay of the conductivity for $K_0 \gtrsim 1$, presumably due to Anderson localization. The present model avoids localization by eliminating intervalley scattering from the outset.

The system size dependence of the average conductivity is shown in Fig. 6.3, for various combinations of disorder strength and scattering range. We take W/L sufficiently large that we have reached an aspect-ratio independent scaling flow and L/d large enough that the momentum cut-off $M > 25$. The top panel shows the data sets as a function of L/d. The in-

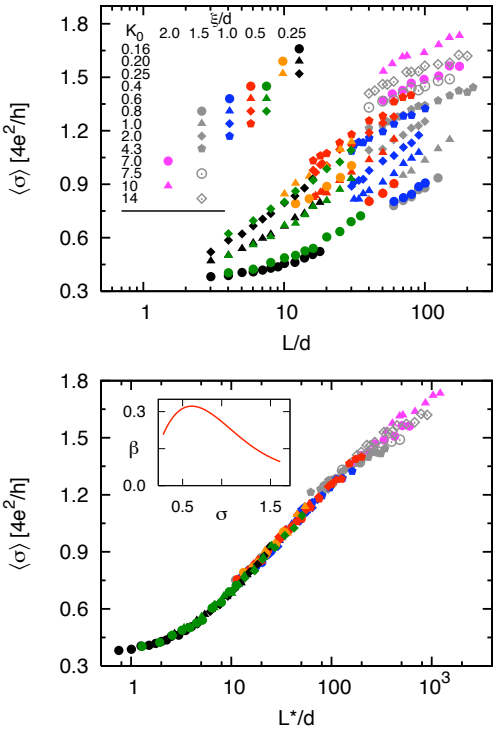

Figure 6.3. System size dependence of the average conductivity, for $W/L = 4$ (black and green solid symbols) and $W/L = 1.5$ (all other symbols) and various combinations of K_0 and ξ/d. The top panel shows the raw data. In the bottom panel the data sets have been given a horizontal offset, to demonstrate the existence of one-parameter scaling. The inset shows the resulting β-function.

crease of σ with L is approximately logarithmic, $\langle\sigma\rangle = \text{constant} + 0.25 \ln L$, much slower than the $\sqrt{L}$ increase obtained in Ref. 38 in the absence of mode mixing.

If one-parameter scaling holds, then it should be possible to rescale the length $L^* \equiv f(K_0, \xi/d)L$ such that the data sets collapse onto a single smooth curve when plotted as a function of L^*/d. (The function $f \equiv d/l^*$ determines the effective mean free path l^*, so that $L^*/d \equiv L/l^*$.) The bottom panel in Fig. 6.3 demonstrates that, indeed, this data collapse occurs. The resulting β-function is plotted in the inset. Starting from

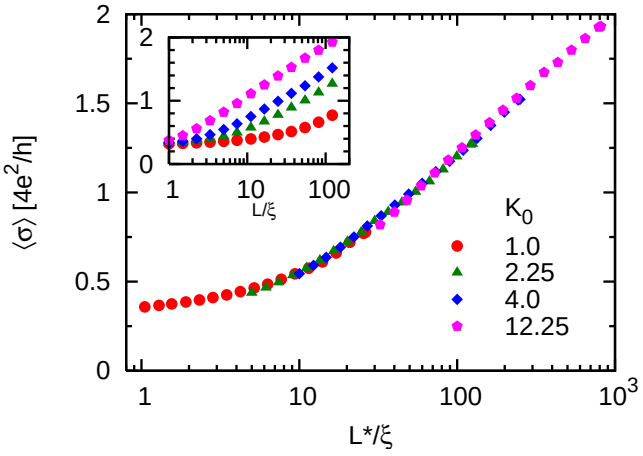

Figure 6.4. System size dependence of the average conductivity in the continuous potential model, for several values of K_0. The inset shows the raw data, while the data sets in the main plot have a horizontal offset to demonstrate one-parameter scaling when $L \gtrsim 5\,\xi$.

the ballistic limit (cf. footnote 2) at $\sigma_0 = 1/\pi$, the β-function first rises until $\sigma \approx 0.6$, and then decays to zero without becoming negative. For $\sigma > \sigma_S \approx 1.4$ the decay $\propto 1/\sigma$ is as expected for a diffusive system in the symplectic symmetry class. The positive β-function in the interval (σ_0, σ_S) precludes the flow towards a scale-invariant conductivity predicted in Ref. 39.

The model of isolated impurities considered so far is used in much of the theoretical literature, whereas experimentally a continuous random potential is more realistic [113]. We have therefore also performed numerical simulations for a random potential landscape with Gaussian correlations[3],

$$\langle U(\boldsymbol{r})U(\boldsymbol{r}')\rangle = K_0 \frac{(\hbar v)^2}{2\pi\xi^2} e^{-|\boldsymbol{r}-\boldsymbol{r}'|^2/2\xi^2}. \tag{6.11}$$

The discrete points $x_1, x_2 \ldots x_N$ in the operator product (6.4) are taken

[3]The Dirac equation with a delta-function correlated random potential has a divergent scattering rate, see, *e.g.,* Ref. 121. Hence the need to regularize the continuous potential model by means of a finite correlation length ξ.

equidistant with spacing $\delta x = L/N$, and

$$U_n(y) = \int_{x_n-\delta x/2}^{x_n+\delta x/2} dx\, U(x,y). \tag{6.12}$$

We take M, N, and W/L large enough that the resulting conductivity no longer depends on these parameters. We then scale towards larger system sizes by increasing L/ξ and W/ξ at fixed K_0. No saturation of σ with increasing K_0 is observed for the continuous random potential (as expected, since the unitary limit is specific for isolated scatterers [119, 120]). Fig. 6.4 shows the size dependence of the conductivity — both the raw data as a function of L (inset) as well as the rescaled data as a function of $L^* \equiv g(K_0)L$. Single-parameter scaling applies for $L \gtrsim 5\,\xi$, where $\langle\sigma\rangle = \text{constant} + 0.32 \ln L$. The prefactor of the logarithm is about 25% larger than in the model of isolated impurities (Fig. 6.3), which is within the numerical uncertainty.

6.4 Conclusion

In conclusion, we have demonstrated that the central hypothesis of the scaling theory of quantum transport, the existence of one-parameter scaling, holds in graphene. The scaling flow which we find (green dotted curve in Fig. 6.1) is qualitatively different both from what would be expected for conventional electronic systems (red dashed curve) and also from what has been predicted [120] for graphene (black solid curve). Our scaling flow has no fixed point, meaning that the conductivity of undoped graphene keeps increasing with increasing disorder in the absence of intervalley scattering. The fundamental question "what is the limiting conductivity σ_∞ of an infinitely large undoped carbon monolayer" has therefore three different answers: $\sigma_\infty = 1/\pi$ in the absence of any disorder [115, 116], $\sigma_\infty = \infty$ with disorder that does not mix the valleys (this chapter), and $\sigma_\infty = 0$ with intervalley scattering [36, 37].

After the work described in this chapter was finished similar conclusions have been reported by Nomura, Koshino, and Ryu [122].

References

[1] R. de Bruyn Ouboter, Sci. Am., March (1997).

[2] E. Merzbacher, *Quantum Mechanics* (John Wiley & Sons, 1998).

[3] J. D. Jackson, *Classical Electrodynamics* (John Wiley & Sons, 1999).

[4] J. J. Sakurai, *Advanced Quantum Mechanics* (Addison-Wesley, 1967).

[5] G. Bergmann, Phys. Rep. **107**, 1 (1984).

[6] H. U. Baranger, R. A. Jalabert, and A. D. Stone, Chaos **3**, 665 (1993).

[7] O. Zaitsev, D. Frustaglia, and K. Richter, Phys. Rev. Lett. **94** (2005).

[8] O. Zaitsev, D. Frustaglia, and K. Richter, Phys. Rev. B **72**, 155325 (2005).

[9] R. Winkler, *Spin-Orbit Coupling effects in Two-Dimensional Electron and Hole Systems* (Springer, 2003).

[10] J. Fabian, A. Matos-Abiague, C. Ertler, P. Stano, and I. Zutic, Act. Phys. Slov. **57**, 565 (2007).

[11] H. A. Kramers, Koninkl. Ned. Akad. Wetenschap. Proc. **33**, 959 (1930).

[12] E. P. Wigner, Göttingen Nachr. p. 546 (1932).

[13] E. P. Wigner, *Group Theory and its Applications to the Quantum Mechanics of Atomic Spectra* (Academic Press, 1959).

[14] J. J. Sakurai, *Modern Quantum Mechanics* (Addison-Wesley, 1994).

[15] F. Haake, *Quantum Signatures of Chaos*, Springer Series in Synergetics (Springer, 2001).

[16] R. Penrose, *The Road to Reality* (Jonathan Cape, 2004).

[17] P. W. Brouwer and C. W. J. Beenakker, J. Math. Phys. **37**, 4904 (1996).

[18] M. L. Mehta, *Random Matrices* (Elsevier, 2004), 3rd ed.

[19] O. V. Dimitrova and M. V. Feigel'man, JETP **102**, 652 (2006).

[20] D. C. Youla, Canad. J. Math. **13**, 694 (1961).

[21] J. Schliemann, J. I. Cirac, M. Kuś, M. Lewenstein, , and D. Loss, Phys. Rev. A **64**, 022303 (2001).

[22] T. Ando, T. Nakanishi, and R. Saito, J. Phys. Soc. Japan **67**, 2857 (1998).

[23] A. H. Castro Neto, F. Guinea, and N. M. R. Peres, Physics World (2006).

[24] A. K. Geim and K. S. Novoselov, Nature Mat. **6**, 183 (2007).

[25] M. I. Katsnelson and K. S. Novoselov, Solid State Comm. **143**, 3 (2007).

[26] O. Govorov, A. V. Kalameitsev, and J. P. Dulka, Phys. Rev. B **70**, 245310 (2004).

[27] C. W. J. Beenakker, in *Quantum Computer, Algorithms and Chaos* (IOS Press, 2006), vol. 162 of *International School of Physics Enrico Fermi*.

[28] M. L. Goldberger and K. M. Watson, *Collision Theory* (John Wiley & Sons, 1964).

[29] M. Dyakonov and V. Perel, Sov. Phys. JETP Lett. **13**, 467 (1971).

[30] J. E. Hirsch, Phys. Rev. Lett. **83**, 1834 (1999).

[31] J. Sinova, D. Culcer, Q. Niu, N. A. Sinitsyn, T. Jungwirth, and A. H. MacDonald, Phys. Rev. Lett. **92**, 126603 (2004).

[32] J. Inoue, G. E. W. Bauer, and L. W. Molenkamp, Phys. Rev. B **70**, 041303 (2004).

[33] E. Abrahams, P. Anderson, D. Licciardello, and T. Ramakrishnan, Phys. Rev. Lett. **42**, 673 (1979).

[34] P. A. Lee and T. V. Ramakrishnan, Rev. Mod. Phys. **57**, 287 (1985).

[35] S. Hikami, A. I. Larkin, and Y. Nagaoka, Prog. Theor. Phys. **63**, 707 (1980).

[36] I. L. Aleiner and K. B. Efetov, Phys. Rev. Lett. **97**, 236801 (2006).

[37] A. Altland, Phys. Rev. Lett. **97**, 236802 (2006).

[38] M. Titov, Europhys. Lett. **79**, 17004 (2007).

[39] P. M. Ostrovsky, I. V. Gornyi, and A. D. Mirlin, Phys. Rev. Lett. **98**, 256801 (2007).

[40] S. Ryu, C. Mudry, H. Obuse, and A. Furusaki, Phys. Rev. Lett. **99**, 116601 (2007).

[41] I. L. Aleiner and V. I. Fal'ko, Phys. Rev. Lett. **87**, 256801 (2001).

[42] P. W. Brouwer, J. N. H. J. Cremers, and B. I. Halperin, Phys. Rev. B **65**, 081302 (2002).

[43] J.-H. Cremers, P. W. Brouwer, and V. I. Fal'ko, Phys. Rev. B **68**, 125329 (2003).

[44] D. M. Zumbühl, J. B. Miller, C. M. Marcus, K. Campman, and A. C. Gossard, Phys. Rev. Lett. **89**, 276803 (2002).

[45] D. M. Zumbühl, J. B. Miller, C. M. Marcus, D. Goldhaber-Gordon, J. J. S. Harris, K. Campman, and A. C. Gossard, Phys. Rev. B **72**, 081305 (2005).

[46] J. Cserti, A. Csordas, and U. Zülicke, Phys. Rev. B **70**, 233307 (2004).

[47] Y. V. Fyodorov and H.-J. Sommers, JETP Lett. **72**, 422 (2000).

[48] A. Ossipov, T. Kottos, and T. Geisel, Europhys. Lett. **62**, 719 (2003).

[49] P. Jacquod, H. Schomerus, and C. W. J. Beenakker, Phys. Rev. Lett. **90**, 207004 (2003).

[50] J. Tworzydło, A. Tajic, H. Schomerus, and C. W. J. Beenakker, Phys. Rev. B **68**, 115313 (2003).

[51] J. Tworzydło, A. Tajic, and C. W. J. Beenakker, Phys. Rev. B **70**, 205324 (2004).

[52] S. Rahav and P. W. Brouwer, Phys. Rev. Lett. **95**, 056806 (2005).

[53] S. Rahav and P. W. Brouwer, Phys. Rev. Lett. **95**, 056806 (2005).

[54] R. Scharf, J. Phys. A **22**, 4223 (1989).

[55] M. Thaha, R. Blümel, and U. Smilansky, Phys. Rev. E **48**, 1764 (1993).

[56] M. Thaha and R. Blümel, Phys. Rev. Lett. **72**, 72 (1994).

[57] A. Ossipov, D. M. Basko, and V. E. Kravtsov, Eur. Phys. J. B **42**, 457 (2004).

[58] P. Jacquod and R. S. Whitney, in *Proceedings of the Fourth international conference on "Unsolved Problems of Noise and Fluctuations in Physics, Biology and High Technology", UPON4* (2005).

[59] F. M. Izrailev, Phys. Rep. **196**, 299 (1990).

[60] C. W. J. Beenakker, Rev. Mod. Phys. **69**, 731 (1997).

[61] Z. Pluhař, H. A. Weidenmüller, J. A. Zuk, and C. H. Lewenkopf, Phys. Rev. Lett. **73**, 2115 (1994).

[62] O. Agam, I. Aleiner, and A. Larkin, Phys. Rev. Lett. **85**, 3153 (2000).

[63] P. G. Silvestrov, M. C. Goorden, and C. W. J. Beenakker, Phys. Rev. B **67**, 241301(R) (2003).

[64] R. S. Whitney and P. Jacquod, Phys. Rev. Lett. **94**, 116801 (2005).

[65] R. S. Whitney and P. Jacquod, Phys. Rev. Lett. **96**, 206804 (2006).

[66] S. Oberholzer, E. V. Sukhorukov, and C. Schönenberger, Nature **415**, 765 (2002).

[67] C. W. J. Beenakker and H. van Houten, Phys. Rev. B **43**, 12066(R) (1991).

[68] P. G. Silvestrov and E. G. Mishchenko, Phys. Rev. B **74**, 165301 (2006).

[69] Y. M. Blanter and E. V. Sukhorukov, Phys. Rev. Lett. **84**, 1280 (2000).

[70] S. Pilgram, A. N. Jordan, E. V. Sukhorukov, and M. Büttiker, Phys. Rev. Lett. **90**, 206801 (2003).

[71] E. V. Sukhorukov and O. M. Bulashenko, Phys. Rev. Lett. **94**, 116803 (2008).

[72] L. W. Molenkamp, G. Schmidt, and G. E. W. Bauer, Phys. Rev. B **64**, 121202(R) (2001).

[73] C. Dellago and H. A. Posch, Phys. Rev. E **52**, 2401 (1995).

[74] J. Nitta, T. Akazaki, H. Takayanagi, and T. Enoki, Phys. Rev. Lett. **78**, 1335 (1997).

[75] H.-A. Engel, L. P. Kouwenhoven, D. Loss, and C. M. Marcus, Quantum Inf. Proc. **3**, 115 (2004).

[76] J. L. van Velsen and C. W. J. Beenakker, Phys. Rev. A **70**, 032325 (2004).

[77] A. Aiello and J. P. Woerdman, Phys. Rev. A **70**, 023808 (2004).

[78] G. Puentes, A. Aiello, D. Voigt, and J. P. Woerdman, Phys. Rev. A **75**, 032319 (2007).

[79] C. W. J. Beenakker, C. Emary, M. Kindermann, and J. L. van Velsen, Phys. Rev. Lett. **91**, 147901 (2003).

[80] W. K. Wootters, Phys. Rev. Lett. **80**, 2245 (1998).

[81] R. F. Werner, Phys. Rev. A **40**, 4277 (1989).

[82] C. W. J. Beenakker and M. Kindermann, Phys. Rev. Lett. **92**, 056801 (2004).

[83] D. Frustaglia, S. Montangero, and R. Fazio, Phys. Rev. B **74**, 165326 (2006).

[84] S. Kawabata, J. Phys. Soc. Jpn. **70**, 1210 (2001).

[85] N. M. Chtchelkatchev, G. Blatter, G. B. Lesovik, and T. Martin, Phys. Rev. B **66**, 161320(R) (2002).

[86] P. Samuelsson, E. V. Sukhorukov, and M. Büttiker, Phys. Rev. Lett. **91**, 157002 (2003).

[87] B. Michaelis and C. W. J. Beenakker, Phys. Rev. B **73**, 115329 (2006).

[88] F. J. Jedema, H. B. Heersche, A. T. Filip, J. J. A. Baselmans, and B. J. van Wees, Nature **416**, 713 (2002).

[89] W. Bauer and G. F. Bertsch, Phys. Rev. Lett. **65**, 2213 (1990).

[90] I. Žutić, J. Fabian, and S. D. Sarma, Rev. Mod. Phys. **76**, 323 (2004).

[91] M. Dyakonov and V. Perel, Phys. Lett. A **35**, 459 (1971).

[92] S. Murakami, Phys. Rev. B **69**, 241202 (2004).

[93] E. G. Mishchenko, A. V. Shytov, and B. I. Halperin, Phys. Rev. Lett. **93**, 226602 (2004).

[94] A. A. Burkov, A. S. Núñez, and A. H. MacDonald, Phys. Rev. B **70**, 155308 (2004).

[95] I. Adagideli and G. E. W. Bauer, Phys. Rev. Lett. **95**, 256602 (2005).

[96] Y. K. Kato, R. C. Myers, A. C. Gossard, and D. D. Awschalom, Science **306**, 1910 (2004).

[97] V. Sih, R. C. Myers, Y. K. Kato, W. H. Lau, A. C. Gossard, and D. D. Awschalom, Nature Phys. **1**, 31 (2005).

[98] J. Wunderlich, B. Kaestner, J. Sinova, and T. Jungwirth, Phys. Rev. Lett. **94**, 047204 (2005).

[99] E. Saitoh, M. Ueda, H. Miyajima, and G. Tatara, Appl. Phys. Lett. **88**, 182509 (2006).

[100] S. O. Valenzuela and M. Tinkham, Nature **442**, 176 (2006).

[101] T. Kimura, Y. Otani, T. Sato, S. Takahashi, and S. Maekawa, Phys. Rev. Lett. **98**, 156601 (2007).

[102] J. Schliemann and D. Loss, Phys. Rev. B **71**, 085308 (2005).

[103] R. Raimondi and P. Schwab, Phys. Rev. B **71**, 033311 (2005).

[104] M. Büttiker, Phys. Rev. Lett. **57**, 1761 (1986).

[105] B. K. Nikolić, L. P. Zârbo, and S. Souma, Phys. Rev. B **72**, 075361 (2005).

[106] E. M. Hankiewicz, L. W. Molenkamp, T. Jungwirth, and J. Sinova, Phys. Rev. B **70**, 241301(R) (2004).

[107] L. Sheng, D. N. Sheng, and C. S. Ting, Phys. Rev. Lett. **94**, 016602 (2005).

[108] W. Ren, Z. Qiao, J. Wang, Q. Sun, and H. Guo, Phys. Rev. Lett. **97**, 066603 (2006).

[109] A. Rycerz, J. Tworzydło, and C. Beenakker, Europhys. Lett. **79**, 57003 (2007).

[110] E. McCann, K. Kechedzhi, V. I. Fal'ko, H. Suzuura, T. Ando, and B. Altshuler, Phys. Rev. Lett. **97**, 146805 (2006).

[111] K. Efetov, *Supersymmetry in Disorder and Chaos* (Cambridge University, Cambridge, 1997).

[112] P. Markos and L. Schweitzer, J. Phys. A **39**, 3221 (2006).

[113] K. Nomura and A. H. MacDonald, Phys. Rev. Lett. **98**, 076602 (2007).

[114] A. W. W. Ludwig, M. P. A. Fisher, R. Shankar, and G. Grinstein, Phys. Rev. B **50**, 7526 (1994).

[115] M. I. Katsnelson, Eur. Phys. J. B **51**, 157 (2006).

[116] J. Tworzydlo, B. Trauzettel, M. Titov, A. Rycerz, and C. W. J. Beenakker, Phys. Rev. Lett. **96**, 246802 (2006).

[117] V. V. Cheianov and V. I. Fal'ko, Phys. Rev. B **74**, 041403(R) (2006).

[118] H. Tamura and T. Ando, Phys. Rev. B **44**, 1792 (1991).

[119] D. V. Khveshchenko, Phys. Rev. Lett. **97**, 036802 (2006).

[120] P. M. Ostrovsky, I. V. Gornyi, and A. D. Mirlin, Phys. Rev. B **74**, 235443 (2006).

[121] A. A. Nersesyan, A. M. Tsvelik, and F. Wenger, Nucl. Phys. B **438**, 561 (1995).

[122] K. Nomura, M. Koshino, and S. Ryu, Phys. Rev. Lett. **99**, 146806 (2007).

Samenvatting

Iedereen heeft wel enige notie van het begrip *spin*, al zal het niet altijd onder die naam zijn. Magneten zijn niets anders dan een grote verzameling spins. Door te spelen met magneten krijgt men gevoel voor de mogelijke sterkte van de magnetische wisselwerking; een spin reageert op een magnetisch veld (bijvoorbeeld een dat wordt veroorzaakt door een andere magneet). Wanneer er geen magnetische velden zijn doet een spin niets, onberoerd als hij is door de omgeving en afwijzend ten opzichte van wisselwerking met elektrische velden. Dat is zo tot de spin begint te bewegen. Zodra de spin beweegt, gaat de relativiteitstheorie een rol spelen. Deze vertelt ons dat het elektrische veld dat we produceren als een magnetisch veld wordt gezien in het ruststelsel van het elektron; daardoor gaan de spin en het elektrische veld een gesprek aan. Vanwege het relativistische karakter van dit effect is deze wisselwerking in het algemeen nogal zwak. De wisselwerking gaat onder de naam *spin-baan-koppeling*.

Dit proefschrift behandelt de effecten van deze spin-baan-koppeling op quantum transport. Het woord *quantum* betekent hier dat we het elektron als fase-coherent beschouwen over de hele grootte van het sample, ofwel: gedurende de tijd die nodig is om van een kant van het sample naar de andere kant te geraken. Deze quantum coherentie is belangrijk, omdat in veel gevallen de aanwezigheid van de spin-baan-koppeling wordt gedetecteerd via de kleine (quantum) correcties op klassieke grootheden. In het bijzonder is dit het geval voor *zwakke (anti) localisatie*, een quantumcorrectie op de geleidbaarheid, veroorzaakt door verhoogde (verminderde) terugverstrooiing ten gevolge van quantum interferentie.

In het derde hoofdstuk, dat volgt op een inleiding in het eerste hoofdstuk en de definitie van het numerieke model dat in de daaropvolgende

analyse wordt gebruikt in het tweede hoofdstuk, beschouwen we het geval dat het quantum-effect dat door de spin-baan-koppeling wordt veroorzaakt een term van eerste orde is. De grootheid die bestudeerd wordt is zogenaamde *hagelruis*; de "klassieke" bijdrage wordt uitgeschakeld door de klassieke limiet van een zeer groot systeem te nemen. Dit is een voorbeeld waarin de spin-baan-koppeling nieuwe verschijnselen veroorzaakt. Het doel van de *spintronica*, electronica met spins, is om dit soort verschijnselen onder controle te krijgen en ze tot ons nut te gebruiken. Soms heeft de spin-baan-koppeling echter onwelkome effecten. Een voorbeeld hiervan wordt gegeven in hoofdstuk vier, waar we bediscussiëren hoe spin-baan-koppeling de elektron-gat-verstrengeling veroorzaakt door een tunnel-barrière afbreekt. Dit gebeurt wanneer de tunnel-barrière zogenaamde *multi-mode* draden verbindt en de spin-baan-koppeling de verschillende modes mengt, leidend tot verminderde spin-verstrengeling.

Een van de doelen van spintronica is om *stromen van spin* te creëren en die te meten. Door het *spin Hall effect* kan een longitudinale ladingsstroom een puur transversale spin-stroom veroorzaken. Op dezelfde manier als waarop wanorde deze spin-stroom uiteindelijk vernietigt zal chaotische dynamica ook de spin-stroom doen verdwijnen, zoals we in hoofdstuk vijf laten zien. Deze bewering slaat op de (ensemble-)gemiddelde stroom. De spin-stroom in een gegeven sample hoeft niet nul te zijn en het blijkt in feite zo te zijn dat de variantie van de spin-stroom ongelijk nul en universeel is.

Het laatste hoofdstuk steekt enigszins af ten opzichte van de eerderen, aangezien het niet handelt over spin. Het onderwerp is het materiaal *grafeen*. De effectieve beschrijving bij lage energie van grafeen gebeurt echter via een Dirac Hamiltoniaan, die gezien kan worden als bevattende een spin-baan-koppeling term. In tegenstelling tot de voorgaande gevallen is de spin-baan-koppeling nu de dominante term en géén kleine correctie. We beschouwen de effecten van wanorde op de geleidbaarheid. We vinden dat gelijkmatige wanorde, enigszins tegen de intuïtie in, de geleidbaarheid, die logaritmisch groeit met de systeemgrootte, verhoogt.

List of Publications

- *Coherent electronic transport in a multimode quantum channel with Gaussian-type scatterers*, J. H. Bardarson, I. Magnusdottir, G. Gudmundsdottir, C.-S. Tang, A. Manolescu, and V. Gudmundsson, Phys. Rev. B **70**, 245308 (2004).

- *Multi-mode transport through a quantum nanowire with two embedded dots*, V. Gudmundsson, G. Gudmundsdottir, J. H. Bardarson, I. Magnusdottir, C.-S. Tang, and A. Manolescu, Eur. Phys. J. B **45**, 339 (2005).

- *Transport through a quantum ring, a dot and a barrier embedded in a nanowire in magnetic field*, V. Gudmundsson, Y.-Y. Lin, C.-S. Tang, V. Moldoveanu, J. H. Bardarson, and A. Manolescu, Phys. Rev. B **71**, 235302 (2005).

- *Stroboscopic model of transport through a quantum dot with spin-orbit scattering*, J. H. Bardarson, J. Tworzydlo, and C. W. J. Beenakker, Phys. Rev. B **72**, 235305 (2005) [Chapter 2].

- *How spin-orbit interaction can cause electronic shot noise*, A. Ossipov, J. H. Bardarson, C. W. J. Beenakker, J. Tworzydlo, and M. Titov, Europhys. Lett. **76**, 115 (2006) [Chapter 3].

- *Degradation of electron-hole entanglement by spin-orbit coupling*, J. H. Bardarson and C. W. J. Beenakker, Phys. Rev. B **74**, 235307 (2006) [Chapter 4].

- *Effect of spin-orbit coupling on the excitation spectrum of Andreev billiards*, B. Béri, J. H. Bardarson, and C. W. J. Beenakker, Phys. Rev. B **75**, 165307 (2007).

- *Mesoscopic Spin Hall Effect*, J. H. Bardarson, I. Adagideli, and Ph. Jacquod, Phys. Rev. Lett. **98**, 196601 (2007) [Chapter 5].

- *Demonstration of one-parameter scaling at the Dirac point in graphene*, J. H. Bardarson, J. Tworzydlo, P. W. Brouwer, and C. W. J. Beenakker, Phys. Rev. Lett. **99**, 106801 (2007) [Chapter 6].

- *Splitting of Andreev levels in a Josephson junction by spin-orbit coupling*, B. Béri, J. H. Bardarson, and C. W. J. Beenakker, Phys. Rev. B **77**, 045311 (2008).

- *Non-local detection of resistance fluctuations of an open quantum dot*, A. I. Lerescu, E. J. Koop, C. H. van der Wal, B. J. van Wees, and J. H. Bardarson, submitted to Phys. Rev. B.

- *Theory of the valley-valve effect in graphene nanoribbons*, A. R. Akhmerov, J. H. Bardarson, A. Rycerz, and C. W. J. Beenakker, submitted to Phys. Rev. B.

- *A Proof of the Kramers Degeneracy of Transmission Eigenvalues From Antisymmetry of the Scattering Matrix*, J. H. Bardarson, to be submitted [Section 1.2.5].

Curriculum Vitæ

I was born in Reykjavík on the 20th of August 1979. I grew mostly up in Selfoss were I attended both grade school and high school at Fjölbrautaskóli Suðurlands, from where I graduated in 1999. The same year I started my undergraduate studies in physics at the University of Iceland. I spent one summer in Lille, France doing experimental work at the University of Science and Technology as a part of my bachelor degree, which I obtained in the summer of 2002. Shortly thereafter I started working under the supervision of Prof. Vidar Gudmundsson on my M.Sc. thesis titled *Grid-free ground state of molecules and transport in nanosystems.* My masters education included a one semester stay in Copenhagen, where I attended courses at both the University of Copenhagen and at the Technical University of Denmark. In September 2004 I began to work at the Institute Lorentz for theoretical physics at the University of Leiden, under the supervision of Prof. Carlo Beenakker. The fruits of that work are partially found in this thesis.

During both my undergraduate and graduate studies I have taught exercise classes in math and physics. I taught math to biology students, and linear algebra, calculus, and classical physics to engineering students. In Leiden I have taught the exercise class in Electromagnetism II three times. In addition to this teaching I have been involved in cluster management, both at the University of Iceland and in Leiden. I have attended a number of summer schools and represented my work in several conferences, both in Europe and in the United States.

Acknowledgments

Blindur er bóklaus maður[1]

As far as I can remember I have been surrounded by books and I cannot imagine life without them. But to really enjoy them discussing, dissecting, even sometimes debating their contents with other people is invaluable. Some people make this role their profession; we often call them teachers. All from reading my first few words as a young boy to writing this thesis I've had the good luck of being mentored through every stage of my edification by enthusiastic, honest and committed people. I can mention a few (Edda Björg Jónsdóttir, Halldór Páll Halldórsson, Reynir Hugason, Ari Ólafsson, Viðar Guðmundsson and Carlo Beenakker) but there are many more and I am equally grateful to all of them. Reflecting on about two decades of education I can not but feel privileged. The opportunity to obtain a balanced and unbiased education from young age is too easily taken for granted.

Ber er hver að baki, nema sér bróður eigi[2]

In this world, there is nothing more valuable than your family and friends. I couldn't have asked for a better family and I don't know how to put in words how much I love them. I hope they know. My friends are scattered around the world so most of them I see only very infrequently. It only takes a few moments to appreciate a real friendship though, and I value all the time I get immensely.

[1] Icelandic proverb, literally: Blind is a man without books.

[2] Icelandic proverb (from Njáls saga), literally: One's back is vulnerable, unless one has a brother.

Finally, the Institute Lorentz has treated me very kindly the time I've spent there. Even before day one, Marianne and Fran helped me with all kinds of things they didn't have to help me with, and always with a smile. For that I'm thankful. An institute is no more and no less then the people that inhabit it. At the Institute Lorentz everyone joins in to create a constructive and friendly atmosphere. An atmosphere that welcomes and stimulates, the ideal conditions for doing science. Knowing that it is not always like that, I thank each and everyone involved for their contribution. I guess I owe you all a hug.

Stellingen

behorende bij het proefschrift

Effects of Spin-Orbit Coupling on Quantum Transport

- Spin-orbit coupling splits the trajectory of an electron reflected by a hard wall, thereby producing shot noise.

  Chapter 3

- The degree of entanglement of a conductor with an isotropic spin density matrix can be obtained from the power spectrum of spin currents.

  Chapter 4

- The sample-to-sample fluctuations of spin currents in mesoscopic systems are universal.

  Chapter 5

- Smooth disorder increases the conductivity of graphene.

  Chapter 6

- A zigzag graphene ribbon in an electric field is metallic or insulating for an even or odd number of atomic rows, respectively.

  A. R. Akhmerov, J. H. Bardarson, A. Rycerz, and C. W. J. Beenakker, arXiv:0712.3233

- Kramers degeneracy does not forbid the splitting of Andreev doublets in a Josephson junction.

  B. Béri, J. H. Bardarson, and C. W. J. Beenakker, Phys. Rev. B **77**, 045311 (2008).

- The mapping of the single-valley Dirac equation to the Chalker-Coddington network model breaks symplectic symmetry.

  I. Snyman, J. Tworzydlo, C. W. J. Beenakker,
  arXiv:0803.2197

- The antisymmetry of the scattering matrix of a disordered photonic crystal with a Dirac spectrum implies that a plane wave incident near the Dirac point has a dark spot in its angular reflection profile.

- Humanity currently faces two serious problems: Climate change and a growth based economy that is over-exploiting the worlds resources. The sets of solutions to the two problems intersect and therefore it is most natural for the international community to focus only on their intersection.

Jens Hjörleifur Bárðarson
29 April 2008